공학박사 학위논문

Preparation of Patterned Isopore Poly(urethane acrylate) and Microporous Poly(vinylidene fluoride) Membranes by Soft Lithography and Their Application to Water Treatment

소프트 리소그래피 방법을 이용한 패턴형 등방공경 PUA 분리막과 패턴형 PVDF 정밀여과막의 제작 및 수처리에의 적용

2015 년 8 월

서울대학교 대학원

화학생물공학부

최 동 찬

Abstract

Preparation of Patterned Isopore Poly(urethane acrylate) and Microporous Poly(vinylidene fluoride) Membranes by Soft Lithography and Their Application to Water Treatment

Choi, Dong-Chan

School of Chemical and Biological Engineering

The Graduate School

Seoul National University

Membrane filtration process is widely used for water and wastewater treatments because of numerous advantages it offers. Critical issues in membrane processes are membrane fouling as well as broad pore size distribution. In this study, patterned isopore membrane with high fouling resistance was fabricated combining soft lithographic method with UV-curable polymer and the effect of pattern on particle deposition were elucidated.

First, membrane with uniform pore size was fabricated using a soft-lithographic method. Due to the precisely controlled pore size by micro size patterns, the

membrane presented narrow pore size distribution comparing with conventional membrane. Furthermore, because the UV-curable polyurethane acrylate with releasing agent which decreases surface energy of PUA was used as the membrane material, it gave rise to better anti-biofouling performance than materials of commercial isopore membrane such as polycarbonate.

Second, a patterned isopore membrane with reverse-pyramid patterns was prepared from UV-curable polyurethane acrylate by the soft lithographic method and extent of particle deposition was investigated during microfiltration. The extent of particle deposition was dependent on not only the ratio of crossflow velocity to permeation velocity, but also the size of particles in the feed. Three dimensional modeling based on computational fluid dynamics was also conducted to predict the vortex formation and elucidate the anti-fouling mechanisms of reverse-pyramid patterned membranes. The vortex was in accordance with the trends of particle depositions during the microfiltration.

Third, correlations between pattern shape and extent of particle deposition were investigated experimentally and were elucidated through three dimensional modeling. The extent of particle deposition on patterned membranes was dependent on both pattern shape and orientation. Three dimensional modeling predicted velocity profile and shear stress distribution on patterned membrane surface. The changes in hydraulic trait at each pattern affected particle deposition. In particular, maximum shear stress mostly governed the extent of particle depositions on the membrane surface.

Keywords : Isopore membrane, Patterned membrane, Anti-fouling, Particle deposition, Three dimensional modeling, Soft lithography, Shear stress, Vortex

Student Number : 2008-21119

Table of Contents

Abstract……..…….... i

Table of contents……..…… iii

List of Figures…….…..…..…x

List of Tables…….……...xx

I. Introduction…….…….…. 1

I.1. Backgrounds……..……. 2

I.2. Objectives……..…….……. 4

II. Literature Review……...…….. 7

II.1. Soft-lithography…….…… 8

II.1.1. Introduction……. 8

II.1.2. Materials for soft-lithography…… 9

II.1.2.1. Hard molds…….…….. 9

II.1.2.2. Soft molds…….…….…….…..……. 11

II.1.2.3. Rigiflex molds…….…….…..……. 14

II.1.3. Diverse patterning techniques of soft-lithography…… 15

II.1.3.1. Soft molding…….…… 15

II.1.3.2. Capillary force lithography application…… 18

II.2. Isopore membranes……. 20

II.2.1. Introduction……... 20

II.2.2. History of isopore membranes……...…… 21

II.2.2.1. Track etched membrane……...…….. 21

II.2.2.2. Focused ion beam method…….…… 24

II.2.2.3. Micro molding…….…….…….. 26

II.2.2.4. Self-assembly…….…….…….... 31

II.2.3. Application of isopore membranes…… 33

II.3. Patterned membranes…….……...… 37

II.3.1. History of patterned membranes…….……..…. 37

II.3.2. Micro patterned hollow fiber membrane…..……. 39

II.3.3. Micro patterned flat sheet membrane…….……. 43

II.3.4. Sub-micro patterned flat sheet membrane…..…..……. 46

II.3.5. Confirmation of antifouling property of patterned membrane …….…...…..…….…….……. 48

II.4. Computational fluid dynamics at membrane……..49

II.4.1. Introduction……..…… 49

II.4.2. CFD for crossflow membrane filtration system……..... 50

II.4.2.1. Crossflow membrane filtration system without spacer……..…….. 50

II.4.2.2. Crossflow membrane filtration system with spacer..53

II.4.3. CFD in Membrane bioreactor……..... 56

III. Tunable Pore Size Micro/Submicron-sieve Membranes by Soft Lithography ……..59

III.1. Introduction ……... 60

III.2. Experimental section …….……..... 63

III.2.1. Preparation of PUA membranes ……..……. 63

III.2.2. Water flux test ……..... 65

III.2.3. Particle separation test ……...……..……. 67

III.2.4. CDC biofouling test ……..…..…… 68

III.2.5. Membrane characterization ……..…. 70

III.3. Results and discussion …….…….……... 71

III.3.1. Preparation of Tunable Pore Size Micro-sieve membrane…… 71

III.3.2. Surface pore characteristics of micro-sieve Membrane …….…..… 74

III.3.3. Submicron-sieve Membrane Preparation and Surface Pore Characterization ……...……..77

III.3.4. Effect of straight pore structure and uniform pore size …….…... 79

III.3.5. Anti-biofouling property of PUA material …….……. 81

III.4. Conclusion ……..…..…… 84

IV. Three-dimensional hydraulic modeling of particle deposition on the patterned isopore membrane in crossflow microfiltration…….….85

IV.1. Introduction ……..…… 86

IV.2. Materials and Methods …….…….…….. 89

IV.2.1. Fabrication of patterned isopore membrane ……...… 89

IV.2.2. Particle depositions during crossflow microfiltration...92

IV.2.3. Numerical method ……...……..…. 95

IV.3. Results and discussion ……...…….……...… 98

IV.3.1. Conformation of a reverse-pyramid patterned membrane ……...…….…...…...……...….....….……. 98

IV.3.2. Deposition of 2 μm particles on the patterned isopore membrane surface ……...……. 102

IV.3.3. Deposition of 5 μm particles or mixture of 2 and 5 μm particles on the patterned isopore membrane surface.. …….105

IV.3.4. Hydraulic flow characteristics on the patterned membrane surface ..……..…….…… 109

IV.4. Conclusions ...……...……114

V. Effects of pattern shape and orientation on fouling behavior……. 115

V.1. Introduction ……...…… 116

V.2. Materials and Methods ……...…….. 118

V.2.1. Materials ……. 118

V.2.2. Preparation of patterned MF membrane …..…….. 119

V.2.3. Pure water flux measurement of MF membrane ..… 121

V.2.4. Particle deposition experiment …….…….. 123

V.2.5. Numerical method …….…..…. 124

V.3. Results and discussion …….…….……..…. 126

V.3.1. SEM images and pure water flux of flat and patterned membrane ……..…… 126

V.3.2. Particle deposition on flat and patterned membrane surface ……...……..…… 129

V.3.3. Wall shear stress near the flat and patterned membrane surface ……. 131

V.3.4. Stream line near the flat and patterned membrane surface …….…….…….. 134

V.3.5. Relationship between particle deposition and wall shear stress …….…….. 136

V.3.6. Relationship between particle deposition and stream line……..…138

V.4. Conclusions ……..…….…… 139

VI. Conclusion ……..……. 141

List of Figures

Figure II-1. Demensial stability (Rogers and Lee 2009) ……..…..… 13

Figure II-2 Schematic diagram of soft molding ……..……. 17

Figure II-3 Schematic diagram of capillary force lithography application (a) thick polymer, (b) thin polymer ……..…… 19

Figure II-4 SEM images of track etched membrane with (a) 200 X magnification and (b) 500X magnification …….. 22

Figure II-5 SEM image of silicon nitride isopore membrane with 25 nm pore size (H. D. Tong 2004) ……...….. 25

Figure II-6 SEM images of (a) line and space micro structure and (b) several micrometer isopore membrane fabricated by micromolding method. (L. Vogelaar 2003) ……..…….. 28

Figure II-7 SEM images of (a) accumulated silica particles and (b) isopore membrane after removing silica particles and photo polymerization (F. Yan 2004) ……..……. 29

Figure II-8 SEM image of isopore membrane prepared by combining micromolding and float casting method after particle

separation experiment. Several micrometer pore was shown behind of sub-micro meter pores (F. Yan 2012) …… 30

Figure II-9 SEM images of (a) top view and (b) cross section of AAO membrane (W. Lee 2006) ……..……..……. 32

Figure II-10 SEM images mixed cell before filtration (left) and cells after filtration (right) (Y. Ou 2014) …… 35

Figure II-11 SEM images of arrayed nanodots. (H. Masuda 2000) …. 36

Figure II-12 SEM images of patterned hollow fiber membrane at (a) 5 mm, (b) 12 mm, (c) 32 mm and (d) 58 mm air gap (Çulfaz et al. 2010) ……..…….. 41

Figure II-13 Schematic diagram of patterned hollow fiber membrane fabrication (Kim et al. 2015) ..…… 42

Figure II-14 SEM images of (a) pyramid, and (b) prism patterned membrane (Won et al. 2012) ……..……... 44

Figure II-15 SEM images of patterned membrane prepared from (a) 180 kDa, (b) 275 kDa, and (c) 430 kDa molecular weight polymer (Won et al. 2014) …… 45

Figure II-16 (a) Schematic diagram of sub-micro patterned UF membrane preparation step and AFM images of (b) flat and (c) patterned membrane (S.H. Maruf et al. 2013)…….. 47

Figure II-17 Pressure distribution on the membrane surface (Rahimi et al. 2005) ……..……..……. 52

Figure II-18 Experimental and modeling results of particle deposition experiment (Radu et al. 2014) ……..…….. 55

Figure II-19 Relationship between bubble size and average wall shear stress (Wei et al. 2013) ……...…… 58

Figure III-1. SEM images of master mold with a pyramid pattern. The base length and height of the pyramids are 28 μm and 10 μm, respectively …….…….. 64

Figure III-2. Schematic diagram of the stirred cell for water flux measurements. To measure the flux of each membrane, membranes were installed in the stirred cell and the reservoir was filled with distilled water. Then, pressurized N2 gas was used to deliver water to the stirred cell. The

weight of the effluent was measured using a balance ……..…… 66

Figure III-3. Schematic diagram and operating conditions of the biofouling test with the CDC reactor …….…….. 69

Figure III-4. Schematic representation of the process steps for the fabrication of soft-lithographically patterned micro/submicron-sieve membranes. A PDMS stamp that is replicated from a master mold is used to generate a working PSMAH stamp. Then UV-curable PUA oligomer solution is dispensed onto the working stamp and scraped with a casting knife. Finally, the fully cured PUA isopore membrane layer with the working stamp is dissolved on a fabric support, where the dissolving PSMAH material acts as a glue to attach the membrane onto the support. The same procedures can also be applied for master mold with submicron-sized features. Note here that the pore size of the isopore membrane can be easily be varied by adjusting the height of the casting knife in the fourth step for this pyramid-shaped master mold …… 73

Figure III-5. Scanning electron microscopy (SEM) images of membranes. a) Commercial PVDF(polyvinylidene fluoride), and b) Commercial track-etched membranes, respectively. The red circles in b) show defective pores with doublets or triplets. c) and d) PUA isopore membranes with different pore sizes fabricated by simply adjusting the vertical height of the casting knife; pore size ~2.6 μm for c) and ~6.3 μm for d). e) Plot of pore size and porosity as a function of the vertical height of the casting knife. Values for the track-etched membrane shown in (b) are indicated in the plot for comparison purposes ……. 75

Figure III-6. SEM images of soft-lithographically fabricated micro-sieve membranes. The height of the casting knife was varied (manually) to obtain isopore micro-sieve membranes with different pore sizes, (a) ~2.7 μm, (b) ~3.5 μm, (c) ~5.9 μm and (d) ~6.4 μm, respectively. The pyramid-patterned Si master mold was used for these membranes. The final thicknesses of the micro-sieve membrane layer on the porous polyester support varied as well, from ~1 μm for (a) up to ~2.3 μm for (d) ……. 76

Figure III-7. SEM images of soft-lithographically fabricated submicron-sieve membranes. (a) Si master mold having vertical array of ~700nm Si pillars, (b) PUA membrane, and (c) Track-etched membrane, respectively. (d) Comparison of pore or pattern size in track-etched and PUA membranes. (e) Plot of the measured porosities for both membranes. Scale bars are 1μm for (a), (b), and (c) ……..…… 78

Figure III-8. a) Comparison of water flux through various membranes with different porosity by the stirred cell test. b) Semi-log plot of the normalized water flux based on the porosity of each membrane used in the flux measurements. c) SEM images of colloidal particles (mixture of 1.1 μm and 300 nm polystyrene colloids) before separation by the isopore membrane, on the membrane surface, and in the permeate after filtration, from left to right, respectively ……. 80

Figure III-9. CLSM images of biofilm on the a) PUA and b) track-etched microsieve membrane surfaces after 48 h of operation in CDC reactor. Green color indicates the P. aeruginosa in biofilm. Imaging area is ~1.2 mm*1.2 mm for both cases. c) ζ-potential of membranes and anti-biofouling

characteristics. Variation of zeta-potential of PUA and TE membranes as a function of solution pH. d) Surface energy of PUA and track-etched membranes …… 83

Figure IV-1. Schematic diagram of fabrication steps for the patterned isopore membrane. UV-curable PUA precursor solution was (a) dispensed on a pyramid-patterned PDMS replica mold and (b) spin-coated at 1850 rpm. (c) The PUA oligomer solution was polymerized by UV-curing at 365 nm for 2 h. (d) Finally, reverse-pyramid patterned PUA membrane was detached from the PDMS mold …… 91

Figure IV-2. Schematic diagram of the crossflow filtration experimental set-up. A peristaltic pump was connected to the permeation line of membrane module to control the pore water flux……..…….. 94

Figure IV-3. Overall domain of computational fluid dynamics modeling . The overall domain size was 75 μm × 150 μm × 2000 μm (width × length × height) and the size of each pattern was 25 μm × 25 μm × 16 μm. The number of elements was 57,864 and fine meshes were generated near the membrane surface to solve complicate flow behavior with accuracy ……..…. 97

Figure IV-4. SEM images of (a, b) surface (c) cross-section, and (d) rear of the patterned isopore membrane …….. 99

Figure IV-5. SEM images of PUA membrane prepared at different rotation rates. (a) 2400 and (b) 2500 rpm. Higher rotation rate gave rise to larger membrane pore size …… 100

Figure IV-6. Average pore size and pore size distribution of PUA membrane. The average pore size of PUA membrane was around 0.8 μm and its deviation was 0.08 μm ……..…101

Figure IV-7. SEM images of particle depositions on the membrane surfaces after crossflow microfiltration of 2 μm particles (a) at Vc = 0.25 m/s with low Jp (=Vc/1000 = 2.5 X 10-4 m/s), (b) Vc =0.42 m/s with low Jp (=Vc/1000 = 4.2 X 10-4 m/s), (c) Vc = 0.25 m/s with high Jp (=Vc /100 = 2.5 X 10-3 m/s), and (d) Vc =0.42 m/s with high Jp (=Vc /100 = 4.2 X 10-3 m/s) ……..…….. 104

Figure IV-8. SEM images of particle depositions on the membrane surfaces after crossflow microfiltration of 5 μm particles (a) at Vc = 0.25 m/s with low Jp (Jp = Vc 1000 = 2.5 X 10-4 m/s), and (b) Vc = 0.42 m/s with low Jp (= Vc /1000 = 4.2 X 10-4 m/s) …….……..…….. 107

Figure IV-9. SEM images of particle depositions on the membrane surfaces after crossflow microfiltration of mixture of 2 and 5 μm particles (a') at Vc = 0.25 m/s with low Jp (Jp = Vc /1000 = 2.5 X 10-4 m/s), and (b') Vc = 0.42 m/s with low Jp (= Vc /1000 = 4.2 X 10-4 m/s). Magnified SEM images are presented at right side of each SEM image ……..… 108

Figure IV-10. Stream lines estimated by 3-D modeling near the patterned isopore membrane surface: (a) Vc = 0.25 m/s with low Jp (=Vc /1000 = 2.5 X 10-4 m/s), (b) Vc = 0.42 m/s with low Jp (=Vc /1000 = 4.2 X 10-4 m/s), (c) Vc = 0.25 m/s with high Jp (=Vc /100 = 2.5 X 10-3 m/s), and (d) Vc = 0.42 m/s with high Jp (=Vc /100 = 4.2 X 10-3 m/s), (a') Vc = 0.25 m/s with low Jp (=Vc /1000 = 2.5 X 10-4 m/s) and (b') Vc = 0.42 m/s with low Jp (=Vc /1000 = 4.2 X 10-4 m/s). For (a') and (b'), the stream lines were estimated, assuming that a 5 μm particle was trapped around the pore in each reverse-pyramid pattern. The blue and red colors of the horizontal spectrum indicate the lower and higher water stream velocity, respectively ……..….. 113

Figure V-1. Schematic diagram of patterned membrane fabrication (Won et al. 2012) …… 120

Figure V-2. Schematic diagram of crossflow microfiltration system ... 122

Figure V-3. SEM images of (a) flat membrane (X1000), (b) flat membrane (X2500), (c) reverse-pyramid membrane (X1000), (d) reverse-pyramid membrane (X2500), (e) pyramid membrane (X1000), and (f) pyramid membrane (X2500) ……127

Figure V-4. Water fluxes of flat and patterned membranes …….. 128

Figure V-5. Amounts of particle deposition at each membrane surface.....130

Figure V-6. Wall shear stresses at each membrane surface. The red and blue colors of the vertical bar indicate higher and lower wall shear stress, respectively …… 133

Figure V-7. Stream lines at each membrane surface …….. 135

Figure V-8. Maximum wall shear stresses of each pattern shape ……. 137

List of Tables

Table II-1 Pore density and mean porosity of various commercial track etched membrane(J. I. Calvo et al. 1995) …… 23

Chapter I

Introduction

I.1. Backgrounds

Recently, water scarcity due to climate change and inequality of water resource threatens to be serious and becomes worse. As a result, a demand for clean water increases rapidly and the related market size is expanding. In this situation, membrane have been one of major solution of water scarcity. The key characteristics of membrane are selectivity and fouling resistance. Membrane with narrow pore size distribution assures more expectable water quality and high fouling resistance enables long term operation without chemical or physical washing.

Track-etching method was applied to membrane fabrication process and the method enabled pore size distribution become narrower than other membranes prepared by phase separation process (Price et al 1962). However, pore collapse appears during track etching process and it reduces pore uniformity. After that, focused ion beam (FIB) etching was utilized to fabricate uniform nanoscale pores (Tong et al. 2004) and micromolding was combined with conventional membrane fabrication process to prepare opened microstructure to be formed (Vogelaar et al. 2003). Float casting, as another recent study, was performed to prepare isoporous membrane (F. Yan 2004) and self-assembly of block-co-polymer and anodic aluminum oxide (Lee et al. 2006 and Karunakaran et al. 2014).

On the other hand, anti-fouling property of membrane has been achieved by adapting micro- or nano sized patterns on membrane surface. The pattern modifies

shear stress and flow near membrane surface (Lee et al. 2013). Patterned hollow fiber membrane have been fabricated and increased membrane performance has been achieved (Çulfaz et al. 2010, Çulfaz et al. 2011a, Çulfaz et al. 2011b, Çulfaz et al. 2011c, Çulfaz et al. 2010d, Kim et al. 2015). Various shape and sized patterns have been applied and also confirmed mitigated membrane fouling and increased water flux (Won et al. 2012 , Maruf et al 2014).

Nevertheless, established isopore membrane fabrication process and modeling for patterned membrane still have shortcomings. For instance, isopore membrane fabricated by FIB requires high-priced equipment and the continuous process is not available. Meanwhile, previous modeling was just accomplished with two dimensional modeling and water permeation was not considered.

Therefore, development of cost effective and possible approach for continuous isopore membrane fabrication process is essential to achieve economic feasibility and high selectivity. Furthermore, three dimensional modeling with water permeation are required to effectively design pattern shapes and to determine appropriate operating conditions for maximizing antifouling effect of patterned membrane.

I.2. Objectives

The objectives of the study were to prepare isopore membranes with soft lithographic method and to investigate effects of pattern on particle deposition. The detail contents are as follows:

(1) Preparation of isopore membrane using soft lithography method

Soft-lithography was applied in the preparation of isopore membrane using a master mold with pyramid or cylindrical pattern and UV-curable polymer. The anti-fouling effect was explained by lower surface energy which was determined experimentally and theoretically.

(2) Preparation of patterned isopore membrane and investigation of its vortex effect on particle deposition

Patterned isopore membrane was prepared by the same way described in (1) except the inverted pyramid pattern. Particle depositions on that membrane were investigated experimentally and were elucidated by vortex development predicted by three dimensional CFD modeling.

(3) The effect of pattern shape and orientation on anti-fouling property

The anti-fouling effect of pyramid, reverse-pyramid, and 45° rotated patterned membrane were elucidated by maximum shear stress which is

developed on the patterned surface. The maximum shear stress of each patterned membrane was predicted by three dimensional CFD modeling.

Chapter II

Literature review

II.1. Soft-lithography

II.1.1. Introduction

Soft lithography is a non-photolithographic technique for preparing micro- and nano-structures using elastomeric material. The soft lithographic method has advantages such as lower cost, higher resolution, and broader application field as biotechnology than photolithographic method. An nano or micro patterned elastomeric stamp (i.e PDMS) is used to replicate patterns on the target surface with feature sizes ranging from 30 nm to 100 μm (Choi et al. 2004). Many kind of materials are used as patterning mold ant the patterning techniques vary as properties of material of mold such as surface energy, Young's modulus, transparency of light and flexibility or compliance. Each property effects on the patterning process and resolution of the product. Among them, common property of mold material is low surface energy. The low surface energy enables detachment between mold and material being patterned after patterning step. Other properties of materials will be discussed at next section.

II.1.2. Materials for soft-lithography

Mold materials are categorized into three different types by its hardness, soft, hard or rigiflex. (Brittain et al. 1998a, Brittain et al. 1998b, Ho et al. 1998, Jeon et al.1998, Xia and Whitesides 1998). Hard mold materials are used for imprint lithography and soft mold materials are applied for soft lithography. The rigiflex mold materials can be applied for both lithographic methods.

II.1.2.1 Hard molds.

Hard molds are prepared by photo lithography or electron beam lithography on silicon wafers. The prepared hard mold is applied for nano imprint lithography (NIL) or room temperature imprint lithography (TRIL) (Kumar et al. 1994, Hong and Lee 2003, Khang and Lee 2000, Khang et al. 2001, Ye et al. 2010). Unlike soft mold, Young's modulus of hard mold is high enough to endure high pressure during pattern replication (Ruchhoeft et al. 1999). Thus hard molds are suitable for NIL and TRIL methods which need high pressure during patterning process. On the other hand, at step-and-flash imprint lithography (SFIL), low pressure is applied. In this case, UV curable pre-polymer solution is widely applied and thus, high transparency in the UV range is needed. Therefore, quartz is typically used for SFIL because of its high transparency in the UV range, high modulus and dimensional stability (Choi et al. 2004).

High Young's modulus of hard mold prevents damaging of pattern from repetitive use of the mold. Therefore master template can be used as hard mold. For example, at NIL or RTIL, nickel electroplating can be carried out to replicate the patterned silicon mold.

II.1.2.2 Soft molds.

Sylgard 184 (Polydimethylsiloxane, PDMS) (Dow Corning, USA) is one of the wildly used soft mold. The normal PDMS mold is prepared by mixing pre-polymer and curing agent with weigh ration of 10:1. Lower curing agent ratio makes PDMS mold softer and sticker. Young's modulus of PDMS is about 2 MPa, depending on the mixing ratio, curing time, and temperature. Mixed PDMS solution should be cured at least 2 h at 60 °C.

The PDMS mold has advantages to be used for soft lithography. It has low surface energy about 21 dyn/cm and the low surface energy enables easy detachment after lithography process. High UV transparency of PDMS mold also permit soft lithography process with UV curable polymer. In addition flexibility and tackiness are advantages of PDMS mold during lithography process because the properties allow conformal contact with the underlying surface. On the other hand, organic solvent resistance and Young's modulus are relatively low comparing with hard molds. PDMS can be swelled easily by toluene, benzene, cyclohexane, and etc. This restricts application of PDMS at soft lithography. Furthermore, low Young's modulus also limits pattern replication. Patterns with high aspect ratio on the PDMS mold can be collapsed, and merged (Hui et al. 2002, Lee et al. 2003, Odom et al. 2002). The deformations of PDMS mold during and after the lithography process is given in the figure II-1.

To avoid such deformations mold with high Young's modulus is needed (Sharp et al. 2004). Hard PDMS which has high Young's modulus around 9 MPa,

was developed. However, hard PDMS is brittle and it needed high pressure during lithography process. To solve the disadvantages of the hard PDMS, soft and hard PDMS were combined. Soft PDMS supports patterned hard PDMS to facilitate handling and conformal contact. As a result, advantages of hard and soft PDMS mold was combined.

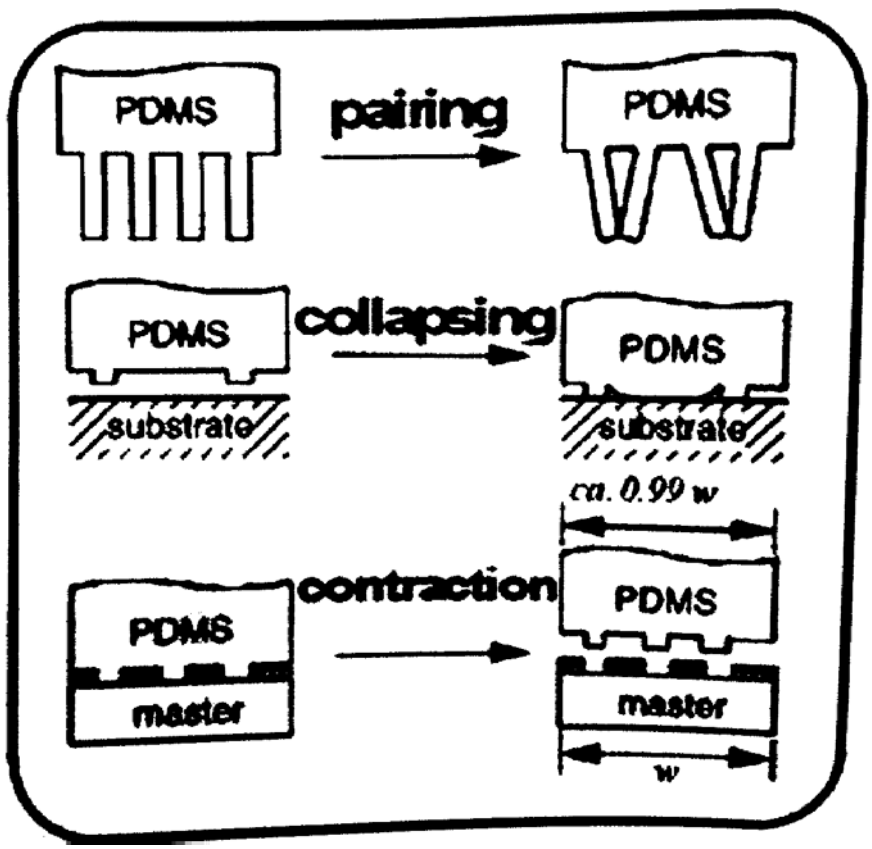

Figure II-1. Demensial stability (Rogers and Lee 2009)

II.1.2.3 Rigiflex molds.

Young's modulus range of rigiflex mold is from tens of MPa to few GPa. The rigiflex mold has both advantages of hard and soft mold, hard enough for high resolution patterning and soft enough for conformal contact with target surface (Kim et al. 1996). Rigiflex molds based on Teflon and UV curable polyurethaneacrylate (PUA) were developed (Khang et al. 2004, Khang and Lee 2004a). In spite of higher modulus, 1 mm thick Teflon mold is more flexible than 1 cm thick soft PDMS.

The PUA mold is made up of three kinds of monomers. One of the monomer is photo initiator which enables UV curing and the other one is releasing agent that facilitate detachment from master template. After casting PUA oligomer solution on the patterned master mold, UV curing is performed at 365 nm for 2 h. Young's modulus of after UV curing of commercial PUA oligomer solution from Minuta tech. are 100 MPa for MINS ERM and 400 MPa for MINS 311RM. The surface energy of PUA mold is about 23 dyn/cm and it allows self-replication (Choi et al. 2004). PUA mold is inert to many kinds of chemical solvents and transparent at UV and visible wave length region. Also, PUA can be applied for imprinting process because of sufficient Young's modulus.

II.1.3. Diverse patterning techniques of soft-lithography

II.1.3.1. Soft molding

Soft molding process is one of the soft lithography techniques. Fundamental of soft molding process is solvent induced capillarity using soft elastomeric mold (Choi and Rogers 2003). The soft molding process do not require high pressure. Therefore, soft molds, such as PDMS, can be applied to the soft molding process (Kim et al. 2001). On the other hand, when the patterns are nano scale, aspect ratio of the patterns are high to cause collapses between patterns. As a result, at the nano patterning process using soft molding method, rigiflex mold is applied to prevent pattern collapsing phenomena.

Figure II-2 indicates schematic diagram of patterning step using soft molding method. First, a polyelectrolyte multilayer was formed onto a substrate via an alternating adsorption process. After spin coating step, 50-60 °C rigiflex mold is placed on the polyelectrolyte multilayer. At this temperature, rigiflex mold softens whereas it is harder than the usual PDMS mold (Yoo et al. 2004). The rigiflex mold is pressed lightly less than 1 N/cm^2 on the 50-60 °C hot plate for 20 min to solidify the polyelectrolyte multilayer. After the solidification the rigiflex mold is peeled off from the polyelectrolyte multilayer.

At the soft molding process solvent absorption of the mold is significant factor. Each rigiflex mold has different absorption weight ratio and the ration varies

with molding temperature. Therefore, optimized solution concentration changes as rigiflex mold type and its chemical property.

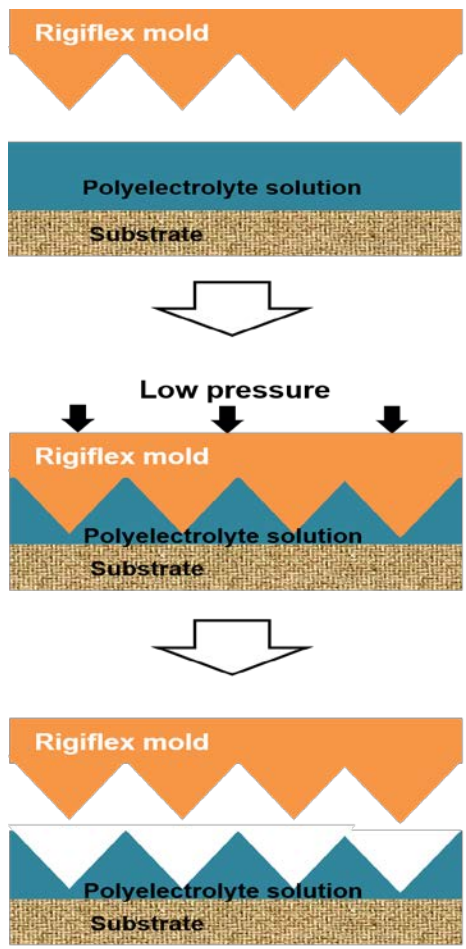

Figure II-2 Schematic diagram of soft molding

II.1.3.2. Capillary force lithography application

For sub-100 nm pattering, capillary force lithography (CFL) is the one of the most economical method for large area pattering. The schematic diagram of CFL is shown at figure II-3. First, thermoplastic resin is spin coated on substrate at proper rotation rate. When the spin coated thickness of thermoplastic is thin, fidelity of the pattern decreases as figure II-3 (b). Temperature of the polymer is increased to Tg after spin coating and solvent evaporation. At Tg polymer chains get mobility and moves toward mold by capillary force. After cooling step, mold is detached from polymer.

At CFL method, polymer and mold affect the normalized height of pattern, Z_m. The driving force, Laplace pressure (P_L) is related with surface tension (γ) and contact angle (θ) where the r is radius of capillary.

$$P_L = \frac{2\gamma \cos\theta}{r}$$

The normalized height follows below equation

$$Z_m = 1 - \frac{1}{P_L}$$

For example, polystyrene at 150 °C with 40 mN/m surface tension and 56.6° contact angle represent the 440 nm normalized height. Therefore, the capillary rise should follow at atmospheric pressure of the feature size smaller than 440 nm (Suh et al. 2001, Khang and Lee 2004b, Lai et al. 2009).

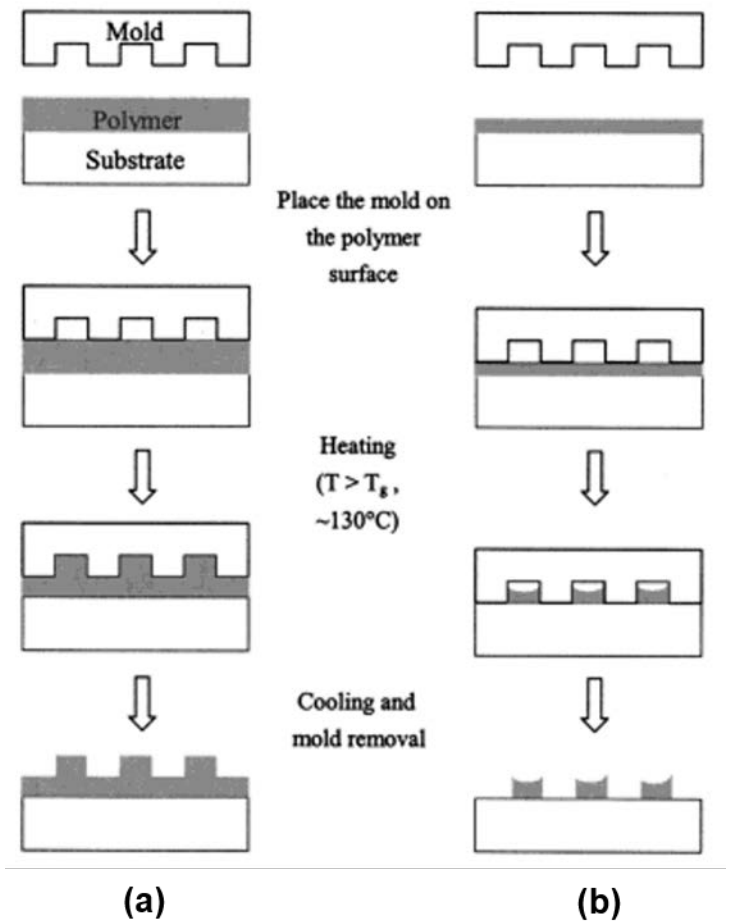

Figure II-3 Schematic diagram of capillary force lithography application (a) thick polymer, (b) thin polymer.

II.2. Isopore membranes

II.2.1. Introduction

Membrane filtration is a simple sieving principle that is a membrane prevents the passage of larger particles than membrane pore size. Thus, the pore size and its distribution of the membrane is one of the key parameters for a filtration process. Conventional membranes have been fabricated by phase separation phenomena, induced temperature-induced phase separation (TIPS) or by non-solvent-induced phase separation (NIPS). However, membranes, which are prepared by phase separation process, have tortuous, long-path pores and broad pore size distribution. The absence of precise pore size control and its spatial distribution are the drawbacks of these methods. In addition, phase separation methods involve organic solvents, which are harmful to operators and the working environment.

To solve the problems of conventional membranes, isopore membranes, which have narrow pore size distribution and straight pore structure, have been prepared by various methods. The isopore membranes are applied not only for water treatment but also protein separation, drug delivery, and electronics. The various preparation methods will be discussed in the next section.

II.2.2. History of isopore membranes

II.2.2.1. Track etched membrane

Among various approaches for the fabrication of isoporous membranes, the track-etch method has been widely used for isopore membrane fabrication. Track etched membrane was first demonstrated using irradiation-etching technique (Price et al 1962) and since 1970s the track etched membrane was commercialized. When a heavy charged particle or ion beams from accelerators traverses polymeric film, it leaves a track of radiation damage. The selective and local damage by high-energy ions on a polymeric film has been shown to generate non-tortuous pores and a relatively uniform pore size after the selective etching of damaged spots. The chemical etching step is pore size and shaped determining step. Due to the random nature of ion bombardment on the polymer surface, however, track etched membranes typically have defects such as doublet and triplet pores as shown in figure II-4 and low pore density as show in table II-1 (Martinez-Villa et al. 1988, Calvo et al. 1995). Moreover the membrane film should be thin enough to be penetrable by ions, which leads to low mechanical strength. Therefore, polymers which have high physical strength such as polyester, polyamide and polycarbonate are widely used as track etched membrane material. However the mechanical strength is poor owing to the absence of a support layer. In addition, track etched membranes have biofouling problems like other membranes (E. M. Tracey 1994, C. Ho 1999).

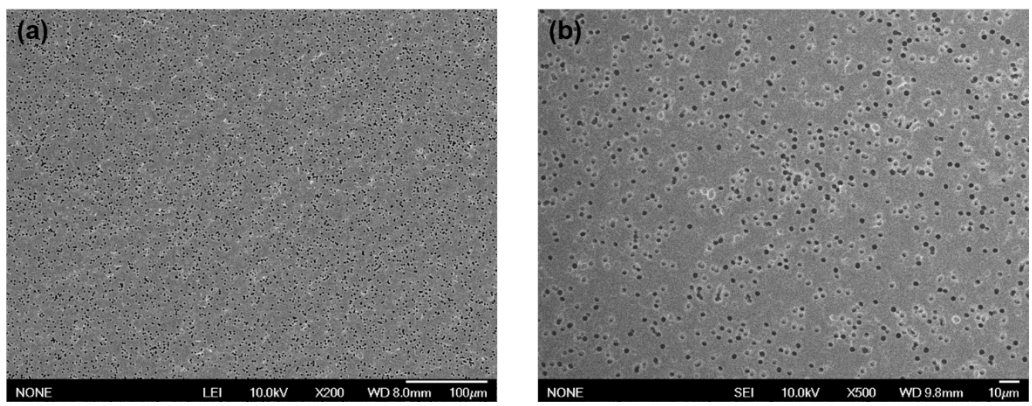

Figure II-4 SEM images of track etched membrane with (a) 200 X magnification and (b) 500X magnification.

Table II-1 Pore density and mean porosity of various commercial track etched membrane(J. I. Calvo et al. 1995).

Membrane	Diameter (μm)	Thickness (μm)	Pore density (10^{12} Pores/m^2)	Mean porosity (%)
C01	0.1	10	6.0	4
C02	0.2	10	4.5	14
C04	0.4	10	1.0	13
C06	0.6	9	0.3	8
C08	0.8	9	0.3	15
C10	1.0	9	0.2	16

II.2.2.2. Focused ion beam method

Another interesting approach is application of focused ion beam (FIB) etching to the membrane fabrication process. Fundamental of FIB is similar with SEM which uses focused electrons to imaging surface of samples while FIB uses focused ions for milling specific surface. High energy ions collide with sample surface and it sputter the surface atoms. Depending on total beam size and chemical property of material 10 – 15 nm size milling is possible. The FIB technique usually applied to material science, biological field, and semiconductor industry.

Isoporous silicon nitride membrane was prepared by using FIB. The thickness of silicon nitride must be adequate to endure during handing, fabrication process, and application process. In consequently, at early application of FIB process, each pore size was larger than 50 nm. To reduce pore size, micro pore sized silicon nitride sieve and ultrathin silicon nitride skin layer were combined. As a result, pore size was reduced to 25 nm while mechanical strength was increased to endure high pressure, several bars, during operation. Figure II-5 indicates the isopore membrane prepared by FIB method. The prepared silicon nitride membrane has high mechanical strength comparing with track etched membrane and chemical and thermal stability. Also, pore collapse were not found and pores were arranged regularly (Tong et al. 2004). However, FIB equipment is high cost and it is difficult to be applied to continuous fabrication process. Furthermore, sort of materials are limited.

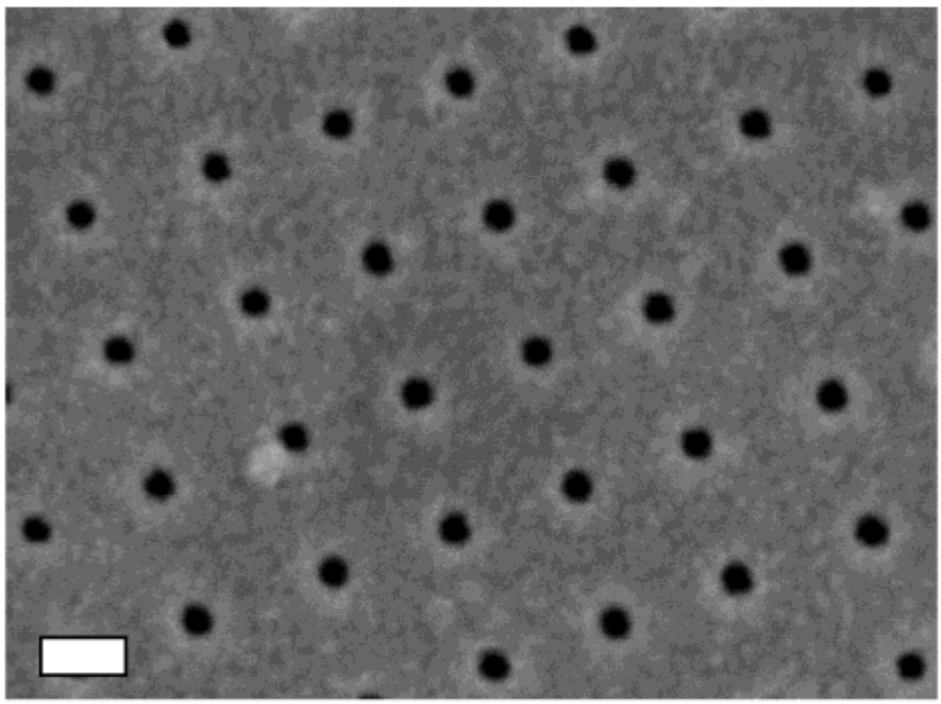

Figure II-5 SEM image of silicon nitride isopore membrane with 25 nm pore size (H. D. Tong 2004).

II.2.2.3. Micromolding

Micromolding is replication of micro scale structured mold using nanoimpint and softlithography. Some researchers have been combined micromolding method with conventional membrane fabrication process, NIPS and TIPS. Polymeric solution was casted on the micro mold with proper thickness and during the solidification polymer film shrinks toward micro mold. Consequently, opened microstructure was formed. Figure II-6 shows the prepared polymeric films by micromoling method. By using line and space pattern, opened line pattern was formed (figure II-6 (a)) and using rod shaped pattern, membrane with micro meter pore size was fabricated (Vogelaar et al. 2003). Comparing with FIB method, micro molding can be applied as continuous fabrication process by adapting roll to roll process. Also high temperature and pressure is not needed during fabrication step. However, pore size was limited to several micro meters yet.

Another approach, float casting, was performed to prepare isoporous membrane. After spreading organic monomer on water surface, sub-micro sized particles were floated with several or tens of particle thickness. The spread organic monomer was photo-polymerized and then sub-micro particles were removed. The final thickness of the membrane is determined by accumulated number of particles. Finally, sub-micro pore sized membrane was prepared as figure II-7 (F. Yan 2004). With the float casting method, pore size can be controlled by floating particle size. However, pore collapse was found on the membrane surface and surface pore size is

larger than size of inner structure pores. Furthermore, the membrane thickness is still thin to make proper mechanical strength and difficult to integrate support layer.

Recently, micromolding and float casting processes were combined to pick advantages of each process. Micromolding method is single step process and that makes several micrometer pores with regular arrangement. The advantage of float casting process is appropriate to fabricate sub-micro pores that is microfiltration membrane. With micromolding method, support layer was fabricated and with float casting method sub-micro pore skin layer was prepared as figure II-8. Support layer which was prepared by micromolding method provide sufficient mechanical strength to handle manually and thus thickness of skin layer prepared by float casting method can be thinner than membrane which was fabricated by float casting method only.

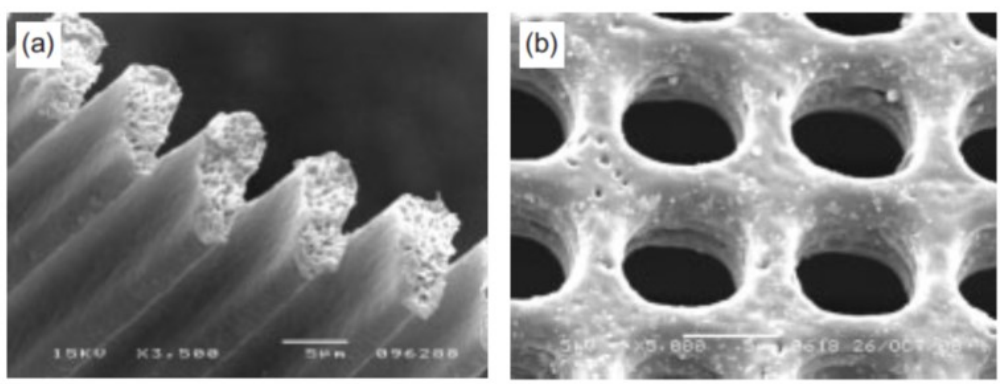

Figure II-6 SEM images of (a) line and space micro structure and (b) several micrometer isopore membrane fabricated by micromolding method. (L. Vogelaar 2003).

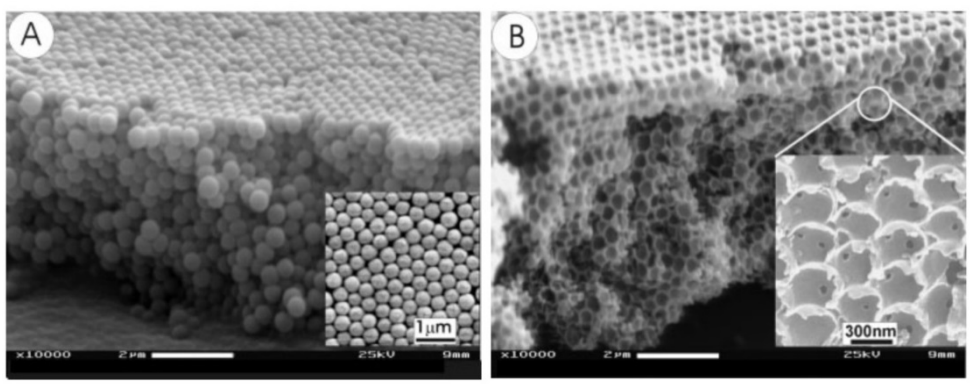

Figure II-7 SEM images of (a) accumulated silica particles and (b) isopore membrane after removing silica particles and photo polymerization (F. Yan 2004).

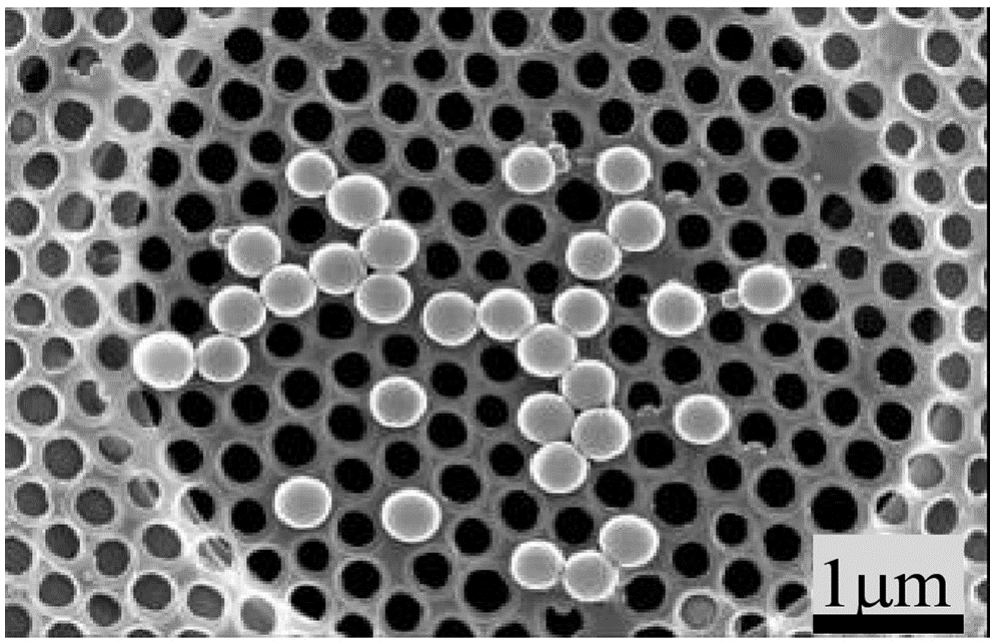

Figure II-8 SEM image of isopore membrane prepared by combining micromolding and float casting method after particle separation experiment. Several micrometer pore was shown behind of sub-micro meter pores (F. Yan 2012).

II.2.2.4. Self-assembly

Self-assembly is organization of molecules by themselves interactions and making specific patterns. Self-assembly was applied to prepare isoporous skin layer and NIPS was combined to form support layer. Many factors affect skin layer property at self-assembly method, such as solvent composition, block copolymer composition and molecular length. Therefore, specific condition have to be found for isopore membrane fabrication. Karunakaran et al. reported 22.2 wt% of PS-b-PEO block copolymer with DMAc, THF, and sulfolane mixture is one of the isopore membrane fabrication condition. Comparing with track etched isopore membrane, porosity was high and pure water flux was high because of straight pore structure.

Another self-ordered membrane is anodic aluminium oxide (AAO) membrane. AAO has been widely used as a master mold to prepare nano wire. Another application area of AAO is membrane for water treatment. Because of its ordered pore structure and simplicity of pore size control. The monodisperse nanopores are prepared under mild anodization condition (25 – 40V) (Masuda et al. 1995). However, mild anodization method is time consuming process and aspect ratio (thickness/poresize) cannot exceed 20. To overcome the disadvantages hard anodization process was applied to AAO isopore membrane fabrication. As a result, aspect ratio more than 1000 was achieved with highly ordered pore structure and uniform pore size (Lee et al. 2006).

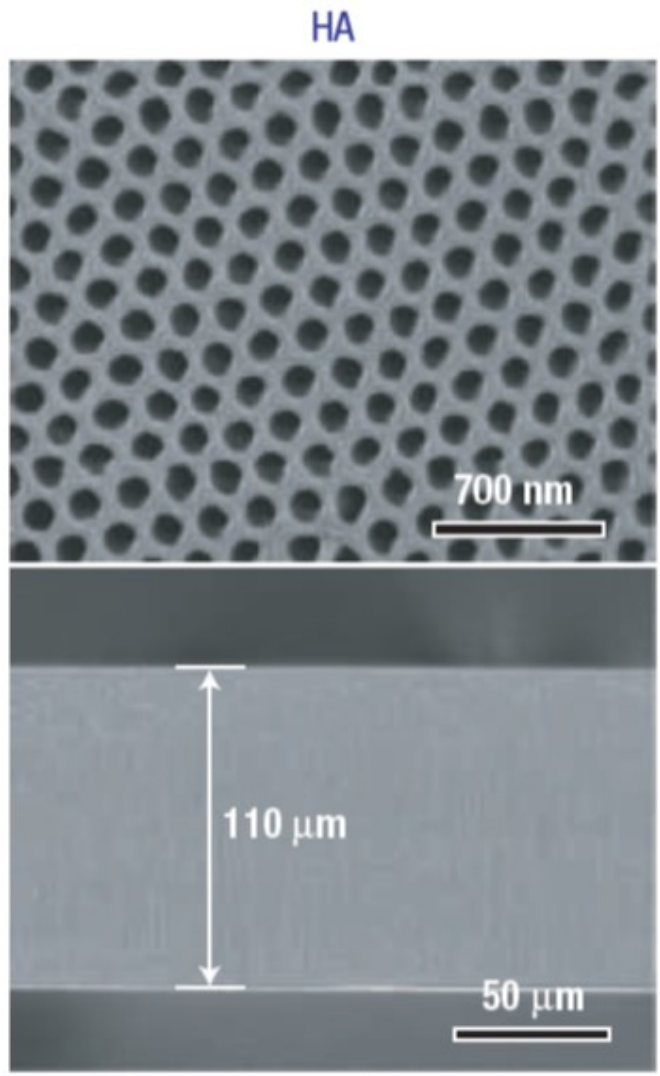

Figure II-9 SEM images of (a) top view and (b) cross section of AAO membrane (W. Lee 2006).

II.2.3. Application of isopore membranes

Advantage of isopore membrane is narrow pore size distribution and it enables separation of specific bacteria, biosensor, controlled release for drug delivery and synthesis of nanostructures.

Ou et al. fabricated 2.5 μm pore sized isopore membrane and applied to separation of mixed cells (yeast and lactobacilli). It is known that lactobacilli has 0.7 μm size and yeast has 3.1 μm. The mixed cell solution was filtered by isopore membrane. After the filtration step mixed cell solution and filtrate were observed by SEM (figure II-10). Yeast cells were rejected almost 100% by isopore membrane and lactobacilli cells were recovered 70%. This result indicates that isopore membrane is effective for mixed cell separation using size exclusion.

Molecule and pore interaction is key factor for biomolecular selectivity at biomolecule detection and drug delivery. Therefore, isopore membrane is advantageous because of high selectivity and high flux. In addition, tunable nanochannels facilitated DNA manipulation. One of application area of isopore membrane is sensor for biotechnology. For application to sensor, the isopore membrane must has biocompatibility and cell barrier while allowing nutrient and waste product exchange. Leoni et al. prepared silicon based nanoporous membrane and tested biocompatibility of the membrane.

Isopore membrane can be applied to synthesis of nanostructures because of its uniform pore size and regular pore arrangement. H. Masuda used AAO as a mask

for nanodot arrangement and they achieved ordered multiple dots with nanometer dimensions.

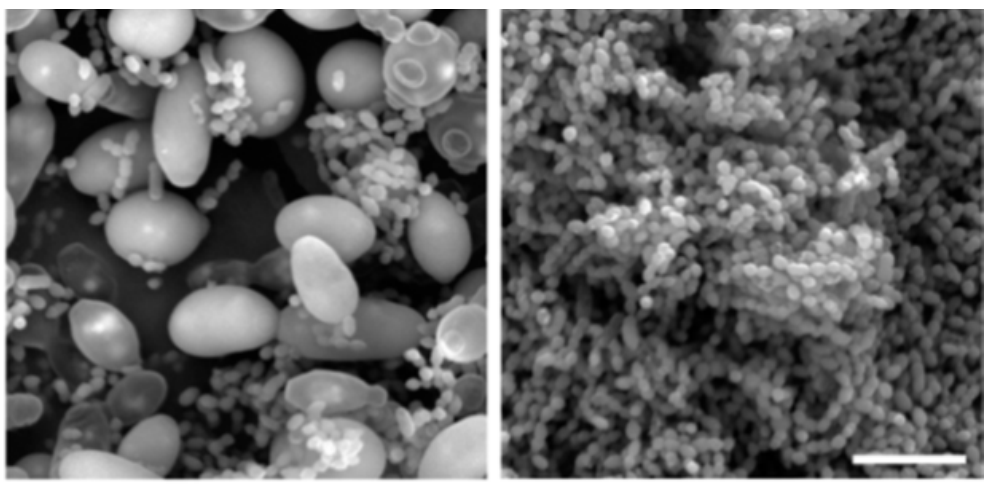

Figure II-10 SEM images mixed cell before filtration (left) and cells after filtration (right) (Y. Ou 2014).

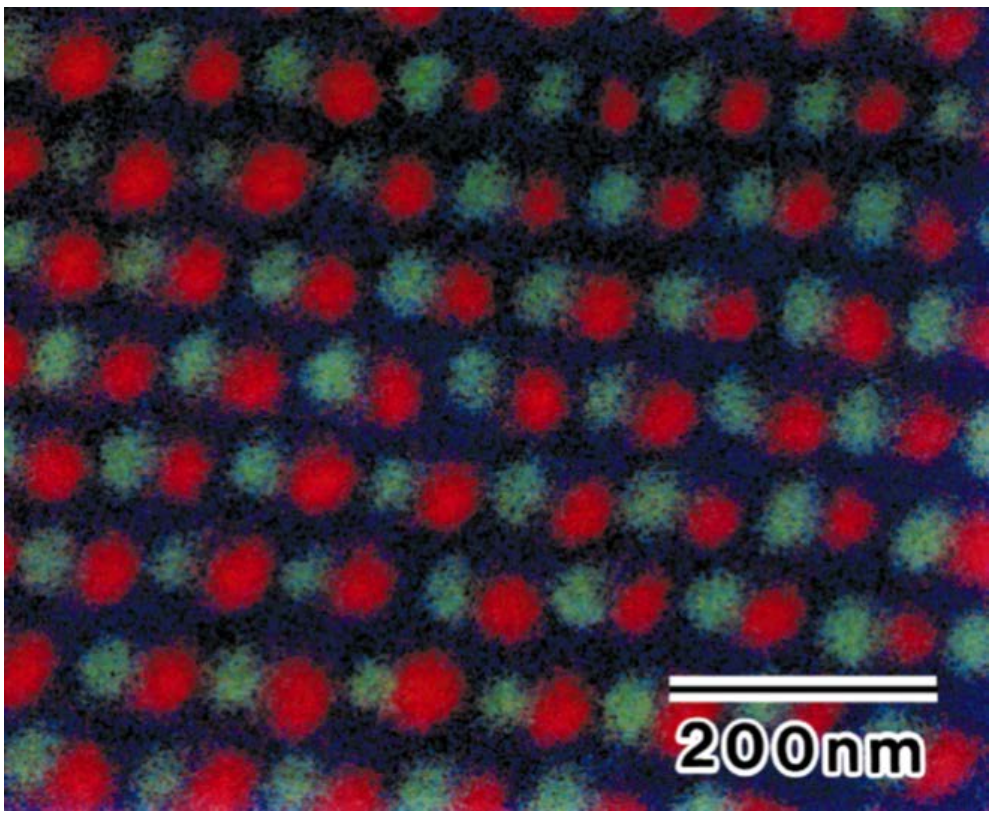

Figure II-11 SEM images of arrayed nanodots. (H. Masuda 2000).

II.3. Patterned membranes

II.3.1. History of patterned membranes

The first patterned membrane was fabricated by Gronda et al. at 2000. The membrane was prepared for gas separation and it had corrugated patterns on membrane surface with mm size. They confirmed flux can be increased by patterns.

Further patterned membrane researches were carried out by M. Wessling group (Çulfaz et al. 2010, Çulfaz et al. 2011a, Çulfaz et al. 2011b, Çulfaz et al. 2011c, Çulfaz et al. 2010d). They prepared microstructured hollow fiber membrane for water treatment and investigated antifouling effect of the pattern.

Won et al. applied various pattern shaped to the patterned membrane. Pyramid, prism, and embossed patterned microfiltration membrane was fabricated and confirmed antifouling effect on cross flow system and membrane bioreactor.

Smaller sized pattern (sub-micro scale) was studied by Ding group. They imprinted sub-micro pattern on the commercial ultrafiltration membrane and effect of the pattern was confirmed by particle deposition experiment.

To confirm effect of pattern, computational fluid dynamic (CFD) was applied by Lee et al. Relating CFD result and fouled patterned membrane surface, they investigated that increased shear stress decreases fouling behavior of patterned

membrane. Detail considerations about various patterned membrane researches will be mentioned at following sections.

In addition, durability of patterned membrane was approved at lab scale RO system and MBR operation. Shape of patterns and anti-fouling effect were conserved after high pressure and long-term operation.

II.3.2. Micro patterned hollow fiber membrane

Çulfaz et al. fabricated micro patterned hollow fiber membrane. Except nozzle shape at the end of ejection part, other process was identical with conventional hollow fiber membrane fabrication. Varying air gap distance (between nozzle and coagulation bath) and polymer dope velocity, pattern fidelity was compared. The SEM images of the patterned hollow fiber showed when the air gap distance increases, pattern fidelity was decreased as shown at figure II-12. On the other hand polymer dope velocity did not affected final pattern fidelity. In this research maximum surface area enhancement was 89%. The water flux of patterned hollow fiber membrane was higher than flat membrane at identical membrane length while molecular weight cut off (MWCO) was similar (Çulfaz et al. 2010). Study about micro patterns at inner surface of hollow fiber membrane fabrication was carried out by same researchers (Çulfaz et al. 2011a). They applied micro structured needle and controlled membrane fabrication condition such as bore liquid flow rate, air gap and residence time in air gap. In this case high bore flow rate reduced pattern fidelity. Pure water flux was similar that is higher water permeability will be shown at identical fiber length condition. On the other hand, mean pore size was increased comparing with flat hollow fiber membrane.

Previous patterned hollow fiber membranes were limited to line and space pattern because patterning method was applying patterned nozzle to the outlet of polymeric solution. To overcome this limitation a new patterned hollow fiber membrane fabrication process was developed recently. Patterned PDMS mold was

rolled into appropriate size straw and then braid was fixed at center position of the straw. After filling polymeric solution between PDMS mold and braid, the straw was dipped into water bath to induce NIPS. As shown in figure II-13 this process enabled fabrication of pyramid patterned hollow fiber membrane and its increased water permeability and antifouling property were confirmed.

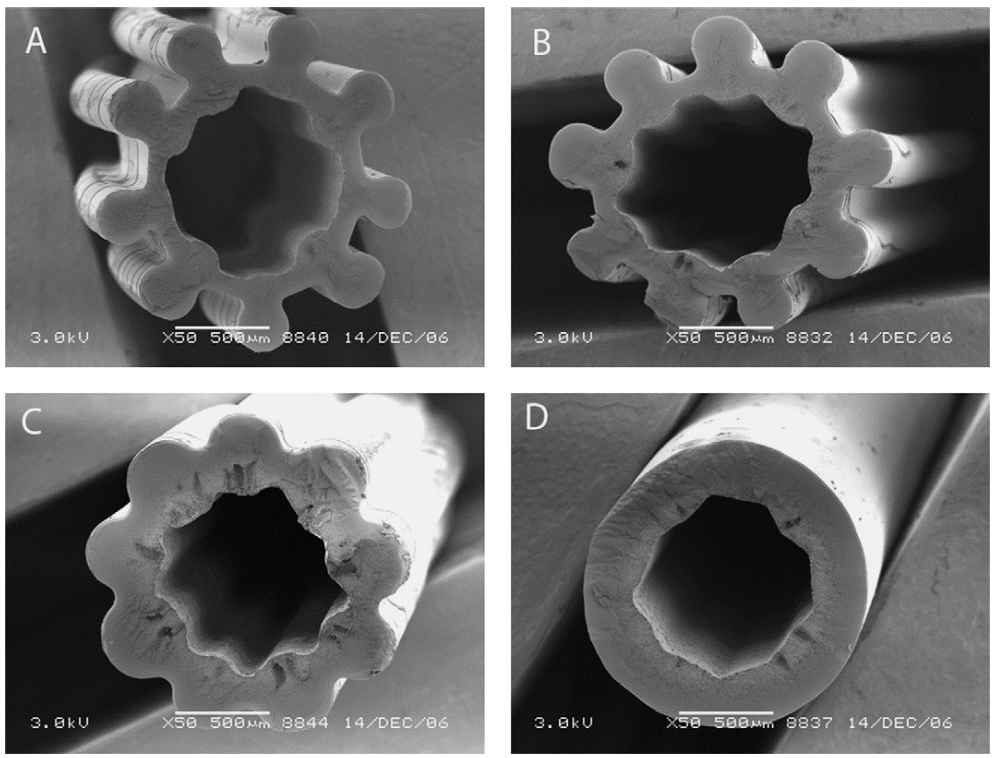

Figure II-12 SEM images of patterned hollow fiber membrane at (a) 5 mm, (b) 12 mm, (c) 32 mm and (d) 58 mm air gap (Çulfaz et al. 2010).

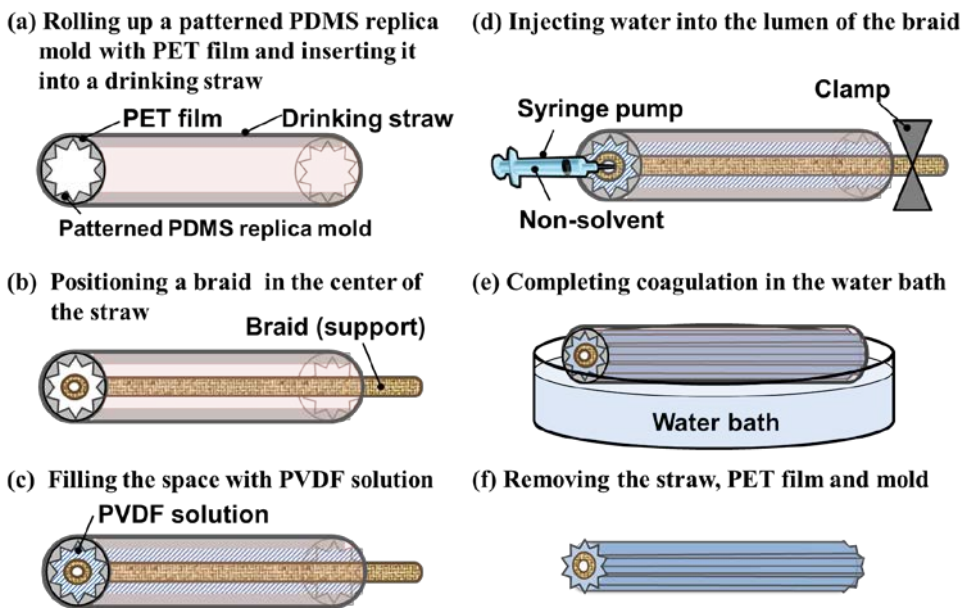

Figure II-13 Schematic diagram of patterned hollow fiber membrane fabrication (Kim et al. 2015).

II.3.3. Micro patterned flat sheet membrane

Microporous patterned membranes have been fabricated by combining soft lithographic method and NIPS. PVDF solution with proper concentration was casted on the patterned PDMS mold, after replicating PDMS mold from master mold. Nonwoven fabric (support layer) was put on the casted PVDF solution, and then dipped into coagulation bath. Micrometer scale pyramid pattern and prism pattern were prepared and pure water flux was measured. The water flux values were increased about 20% comparing with flat sheet membrane. In addition, prepared patterned membrane and flat membrane were applied to lab scale MBR to confirm anti-fouling effect of micro patterns (Figure II-14). Further study about pattern fidelity was carried out by Won et al. They confirmed the effect of molecular weight of polymer, concentration and work of adhesion of replica mold on pattern fidelity. The pattern fidelity was increased as molecular weight of polymer was decreased (180 kDa) at each polymer concentration, 10 wt% and 15 wt% because phase inversion rate is faster at low molecular weight condition than high molecular weight condition. The work of adhesion of replica mold was affected pattern fidelity (Figure II-15). The best pattern fidelity was appeared when the work of adhesion of replica mold was similar with polymeric solution. They also confirmed the effect of pattern height on water flux and anti-fouling property of patterned membrane. Higher pattern height shown greater water flux and anti-fouling property than lower pattern height because of increased surface area and local shear stress at apex of pattern.

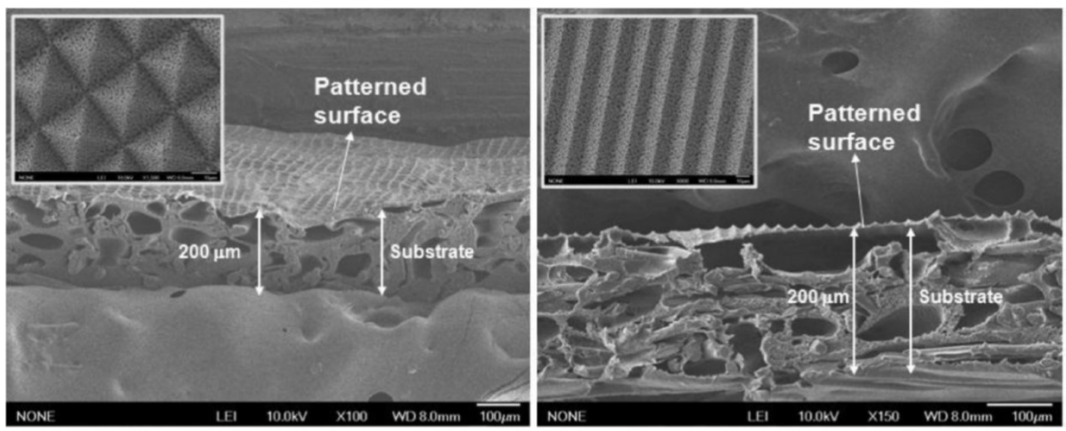

(a) (b)

Figure II-14 SEM images of (a) pyramid, and (b) prism patterned membrane (Won et al. 2012).

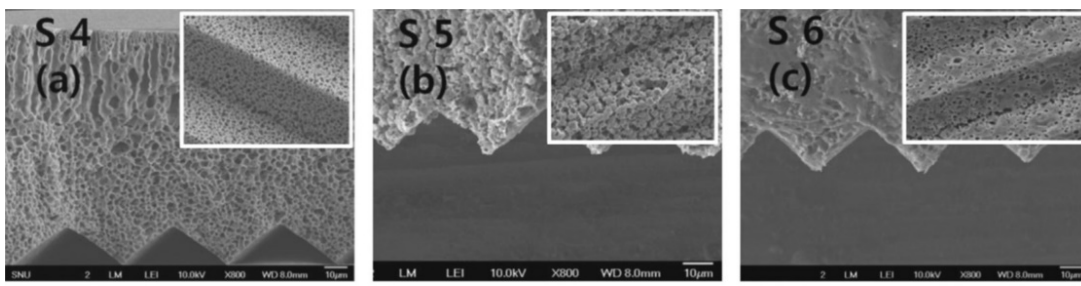

Figure II-15 SEM images of patterned membrane prepared from (a) 180 kDa, (b) 275 kDa, and (c) 430 kDa molecular weight polymer (Won et al. 2014).

II.3.4. Sub-micro patterned flat sheet membrane

Sub-micro scale patterned membrane was fabricated by Maruf et al. In this study, line and space pattern with 830 nm width and 200 nm depth was prepared by nanoimprint lithography and it was applied to form sub-micro pattern on commercial polyethersulfone ultrafiltration membrane (figure II-16). The UF membrane was pressed with patterned mold at 4MPa for 180 s after surface temperature was increased to 120 °C that is below T_g value of PES. After preparation of sub-micro patterned membrane, they measured water flux with suspended sub-micro size silica particles. They confirmed the increases of critical flux of patterned membrane.

Jang et al. fabricated patterned membrane with smaller pattern than Ding group. They applied NIL method as Ding group but applied smaller patterned mold, AAO. The AAO had 100 nm pores and the mold with NIL method made embossed pattern on membrane surface. Fouling behavior was identified by water filtration with various sized latex particles. With this study, relationship between pattern size and foulant size was confirmed.

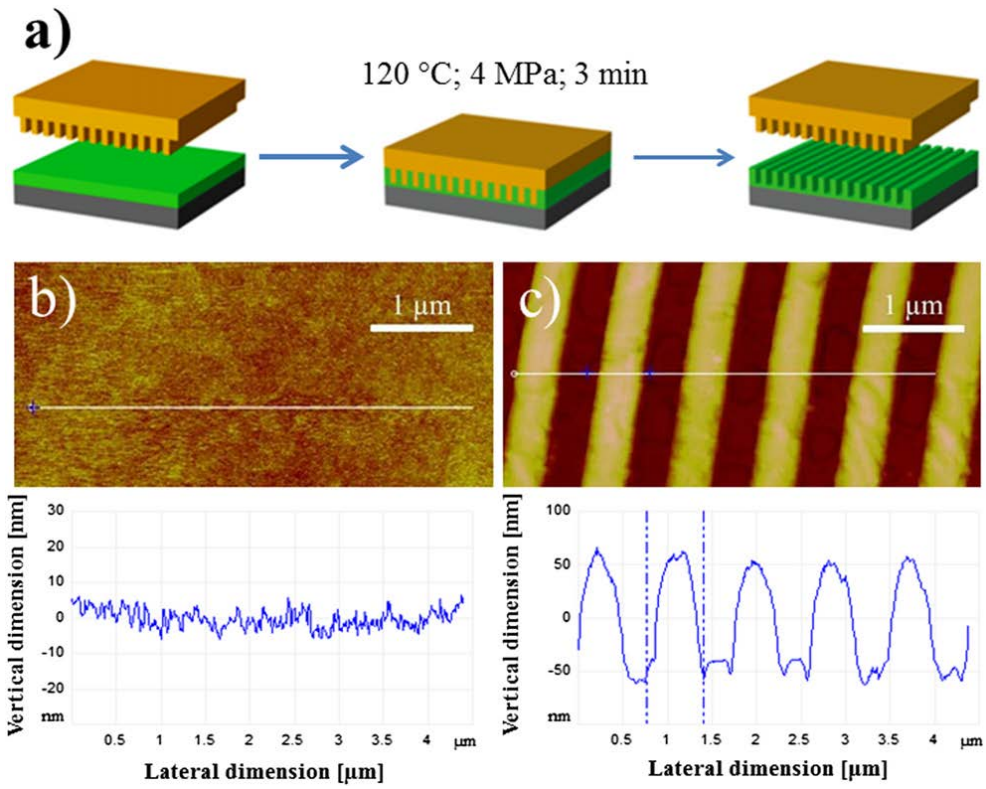

Figure II-16 (a) Schematic diagram of sub-micro patterned UF membrane preparation step and AFM images of (b) flat and (c) patterned membrane (S.H. Maruf et al. 2013).

II.3.5. Confirmation of antifouling property of patterned membrane

Many researchers have been confirmed about anti-fouling property of patterned membrane. However, they assumed the effects of pattern on fouling behavior. To clarify the pattern effect some studies have been carried out by combining computational fluid dynamics and patterned membrane experiment. Lee et al. prepared patterned microfiltration membrane and performed crossflow filtration experiment with activated sludge. After filtration experiment, attached sludge on patterned membrane surface was observed by CLSM. To account different fouling behavior between flat and patterned membrane CFD analysis was performed. The CFD results indicated that overall wall shear stress was higher at flat surface membrane. On the other hand, wall shear stress of upper region of patterned membrane was much higher than flat surface membrane and the wall shear stress distribution affected fouling behavior.

II.4. Computational fluid dynamics at membrane

II.4.1. Introduction

In the membrane filtration systems, hydrodynamics of fluid plays an important role and computational fluid dynamics (CFD) has been applied to investigate flows in membrane module and fouling trend. Since the membrane filtration is pressure driven process, analysis of pressure distribution on the membrane surface using CFD is helpful for prediction of water flux in crossflow microfiltration (Rahimi et al. 2005). The influence of filter geometry and shear rate on membrane fouling in RO and NF filtration process were also identified (Hoek et al. 2002). In the MBR process, aeration has been accomplished for not only sludge maintenance but also delay of membrane fouling caused by physical effect of air bubbles. Therefore, appropriate aeration intensity or cycle have been significant factor for cost effective MBR operation. To find out optimum aeration process, CFD is one of the powerful tool. Effect of intermittent slug bubbling in MBR was investigated using CFD (Wei et al. 2013). CFD modeling for full scale MBR on hollow fiber membrane considering liquid velocities with different flow direction and fluid viscosity (Wang et al. 2010). Detail usages of CFD method to membrane filtration process will be discussed in the next section.

II.4.2. CFD for crossflow membrane filtration system

II.4.2.1. Crossflow membrane filtration system without spacer

Since the membrane filtration process is driven by pressure typically, the distribution of pressure is important for predict water flux and membrane fouling behavior. Therefore, pressure distribution on microfiltration membrane surface at crossflow system was identified by using CFD method.

Rahimi et al. carried out CFD modeling to identify pressure distribution of membrane surface in membrane module with different sized trapezoidal barrier, skew barrier and without barrier. They confirmed that each CFD result demonstrated different pressure distribution as shown following figure and water flux prediction was more accurate than simple calculation.

Yuanfa et al. inserted helical screw in the membrane module as a turbulence promoter. The screw was simulated three dimensionally for CFD and it showed entirely changed hydrodynamics in result. The changed fluid flow reduced particle deposition and flow resistance. As a result, energy consumption was lowered comparing with conventional crossflow system.

Hoek et al. identified relationship between pressure drop, module geometry (height of channel), colloid deposition, and shear stress during NF or RO crossflow filtration system. They found that higher shear stress reduces pressure drop and colloidal particle deposition by combining CFD and experimental results. However, since the most NF, and RO membrane are applied as spiral wound module with

spacer, CFD modeling and filtration experiment without spacer would far from real system. In the next section, NF and RO crossflow with spacer will be discussed.

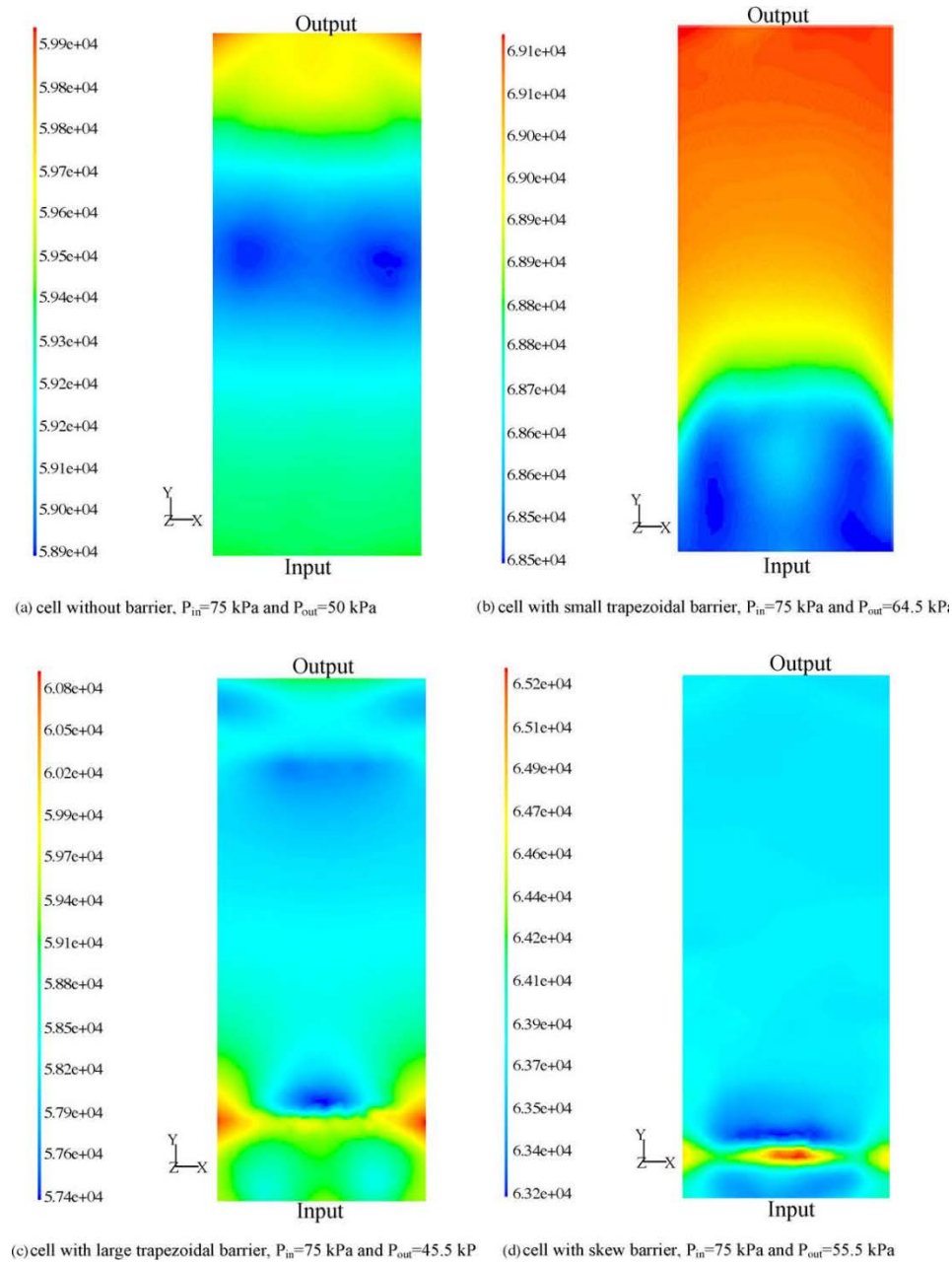

Figure II-17 Pressure distribution on the membrane surface (Rahimi et al. 2005).

II.4.2.2. Crossflow membrane filtration system with spacer

Feed spacers in NF or RO spiral wound module are applied between two flat sheet membranes for induce vortex-wave flow, increased mass transfer and anti-fouling properties. To find out effective shape of spacer, CFD was employed to predict or analyze flow behavior, mass transfer, and power dissipation.

Schwinge et al. established flow patterns with spacer at various Reynolds number condition and thickness of feed spacer. The CFD results showed flow patterns were depend on flow velocity and thickness of feed spacer. However, the CFD was performed at two dimensional system. Therefore, the result would not reflect real crossflow system with spacer.

To resolve limitation of two dimensional simulation, three dimensional simulation was performed by other researchers. Li et al. performed a study to estimate optimized spacer. They altered length angle of square of non-woven spacer. According to this research, ratio of length and thickness of fiber affected mass transfer and optimum ratio value exists.

Another research for geometry of feed spacer was carried out by Radu et al. They changed configuration of feed spacer (diamond or ladder) and performed particle deposition experiment and three dimensional modeling at different crossflow velocity. Faster crossflow velocity caused more particle deposition and altered deposition area because of collision chance between particle and membrane surface and changed wall shear stress. In addition the number of deposited particle

and area were not different on membrane and glass surfaces. The result indicated that water flux at NF and RO system is negligible because velocity difference between bulk stream and water permeation is high. (figure II-18)

Vrouwenvelder et al. developed three dimensional model for describing biofouling and fluid flow at membrane surface with spacer. The simulation result was corresponded with magnetic resonance image after biofouling test and pressure drop was predicted accurately. Therefore, using CFD modeling membrane fouling trend and optimization of feed spacer shape and operating condition can be decided without cost and time consuming experiment.

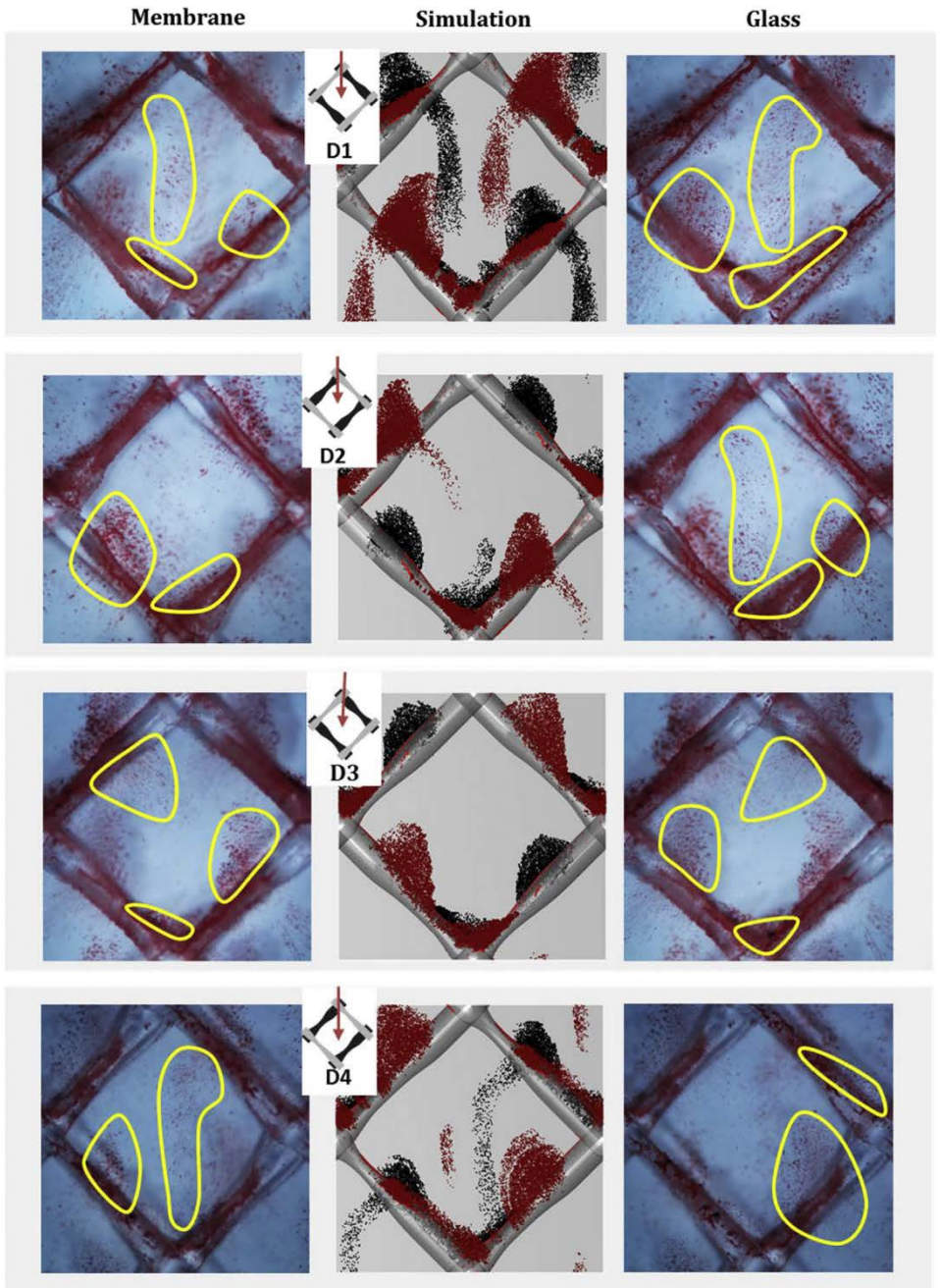

Figure II-18 Experimental and modeling results of particle deposition experiment (Radu et al. 2014).

II.4.3. CFD in Membrane bioreactor

Aeration is an essential process for membrane bioreactor (MBR) operation for supply oxygen to bacteria and membrane fouling mitigation. In particular, since the aeration intensity is related with membrane fouling directly, many kinds of effective aeration processes have been developed. One of the effective aeration processes is periodic introduction of large air bubbles. Electrochemical experiments have been carried out to confirm the effect of periodic slug bubbling. However, shear stress and mass transfer of oxygen information were limited due to experimental condition. Wei et al. applied CFD modeling to estimate the effect of slug bubble flow. They observed real shape of air bubble and traced to modeling system. The modeling result established relationship between air bubble size and wall shear stress. The average wall shear stress increased rapidly to 60 mL of bubble volume and increased gently over the 60 mL bubble volume region as figure II-15.

Membrane configuration is one of the important factors for membrane filtration. High packing density of membrane module has advantage for water flux at identical membrane module volume. Gunther et al. estimated the effect of membrane packing density. Their CFD result indicated that high packing density induces non-uniform water flux and it caused higher local flux than critical flux. AS a result, filtration flux decreased dramatically.

Since precise CFD result requires small mesh size, CFD for large MBR is difficult because computation effort is required. Especially, large number of hollow fiber membranes are installed as a bundle of fibers. Therefore, in spite of usefulness

of CFD modeling to MBR system, CFD study for real system MBR was limited. To exceed the limitation, Wang traced the hollow fiber bundles as a porous media. The assumption enabled investigation of effect of sludge viscosity on the flow regimes.

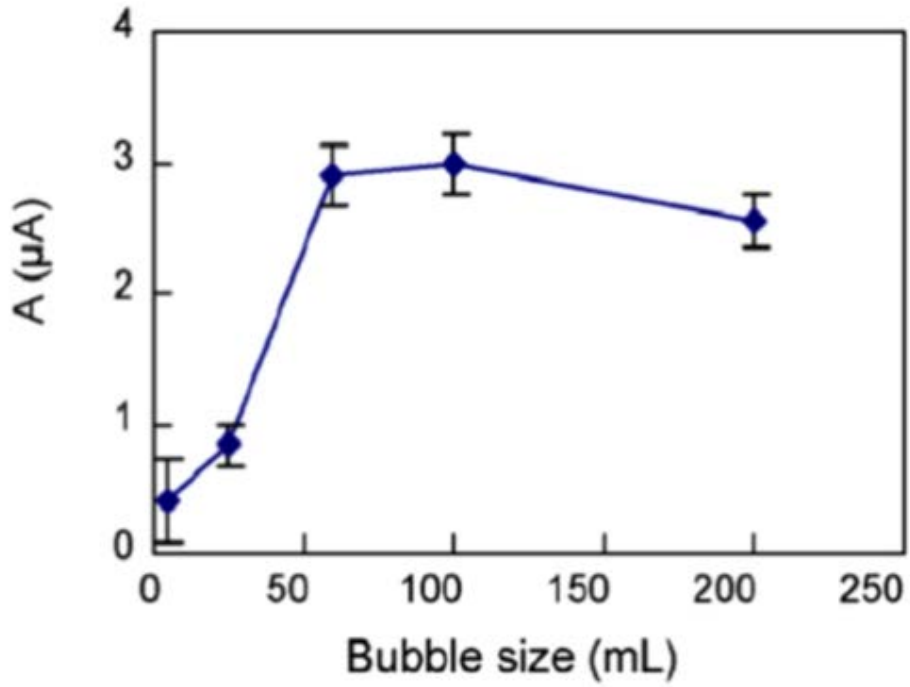

Figure II-19 Relationship between bubble size and average wall shear stress (Wei et al. 2013).

Chapter III

Tunable Pore Size Micro/Submicron-sieve Membranes by Soft Lithography

III.1. Introduction

Membrane filtration or separation is often based on a simple “sieving” principle: a membrane prevents the passage of contaminants that are larger than its pore size. Thus, for a given membrane, the pore size and its distribution, as well as the overall fraction of pores (i.e., porosity), are some of the key parameters determining its usefulness for a specific application. To generate porous polymeric membranes, phase separation phenomena, induced either thermally (temperature-induced phase separation, TIPS) or by adding a non-solvent (non-solvent-induced phase separation, NIPS), have been the most common fabrication methods(Strathmann 2011, Mohanty et al. 2011). Although these phase separation-based methods have been successfully applied, membranes that have tortuous and thus long-path pores generated by these methods pose adverse impacts such as reduced water flux, pore clogging, pressure buildup and increased operation power requirements for periodic back-flushing(Judd et al. 2006, Le-Clech et al. 2006, Drews et al. 2010) . More fundamentally, the absence of precise pore size control and its spatial distribution are the drawbacks of these methods. Furthermore, these methods involve various organic solvents, both in the liquid and vapor phases, which are harmful to operators and the working environment unless tight emission controls are implemented.

Among various approaches for the fabrication of isoporous, micro/submicron-sieve membranes, the track-etch method has been widely used for polymeric membranes

with non-tortuous and narrow size-distributed pores (Warkiani 2013 et al). The selective and local damage by high-energy ions on a polymeric film has been shown to generate non-tortuous pores and a relatively uniform pore size after the selective etching of damaged spots. Due to the random nature of ion bombardment on the polymer surface, however, track-etched membranes typically have defects such as doublet and triplet pores (Calvo et al. 1995, Fmartinez-Villa et al. 1988). Moreover the membrane film should be thin enough to be penetrable by ions, which leads to low mechanical strength. In addition, track-etched membranes have biofouling problems like other membranes, and the mechanical strength is poor owing to the absence of a support layer (Ho et al. 1999, Tracey et al. 1994). Although a few studies have been done to solve the problems of biofouling and low mechanical strength, the practical applications of track-etched membranes in water and wastewater treatment are still limited (Apel 2001, Worrel et al 2007, Vakuliuk 2009 et al.). Another interesting approach is to combine phase separation micromolding and/or float-casting, which has led to the fabrication of hierarchically structured micro-sieve membranes (Vogelaar et al. 2003, Yan et al. 2004, Yan et al. 2012, Wachner et al. 2013). In addition, focused ion beam etching has also been applied to the membrane fabrication process (Tong et al. 2004).

In this work, we have demonstrated a simple yet environmentally benign method for the preparation of micro/submicron-sieve membranes using soft lithographic technique. The soft-lithographically patterned membranes were designed to have non-tortuous pores running through the entire thickness of the membrane to increase water permeability. The size (and uniformity) of pores and their spatial distribution

were also designed to be precisely controlled by the patterns on the mold or stamp used. Particularly, in contrast to the necessity of solvents/non-solvents in conventional phase inversion methods, the use of a patterned mold in our soft lithographic process enabled the adoption of solvent-less, UV-curable polyurethane acrylate (PUA) as the membrane material. The surface energy and surface zeta potential of the PUA membrane were measured/calculated to elucidate its anti-biofouling performance. Surface porosity, mean pore size, and pore size distribution of prepared PUA membranes were characterized by SEM and image analysis program. Water permeability, fractionation of particles, and anti-biofouling characteristics were also tested for PUA membranes.

III.2. Experimental section

III.2.1. Preparation of PUA membranes

A polydimethylsiloxane (PDMS; Sylgard 184, Dow) stamp was replicated from the master mold with a regular array of pyramids (Figure III-1). Then, a disposable working stamp of poly(styrene-co-maleic anhydride) (PSMAH; Sigma-Aldrich) was made by casting a PSMAH/toluene solution (15 wt.%) onto the PDMS replica stamp. The released PSMAH stamp was fixed on a flat glass slide, and the PUA oligomer solution (Minuta, Korea, 311RM) was applied to it. Excess PUA, along with the top part of the pyramidal pattern of PSMAH, were removed by a casting knife. The height of the casting knife was controlled manually, and this had a direct correlation with the pore size of the final PUA membrane. After UV curing of PUA for 2 h at 365 nm, the working PSMAH stamp with the cured PUA membrane on it was placed on a polyester fabric support layer. Finally, dipping the entire sample into toluene led to the dissolution of the underlying PSMAH, leaving the isoporous PUA membrane layer on the fabric support. The same procedure was applied for the preparation of an isoporous PUA membrane with sub micron-scale pores, starting with a master mold of a vertical array of Si submicron pillars.

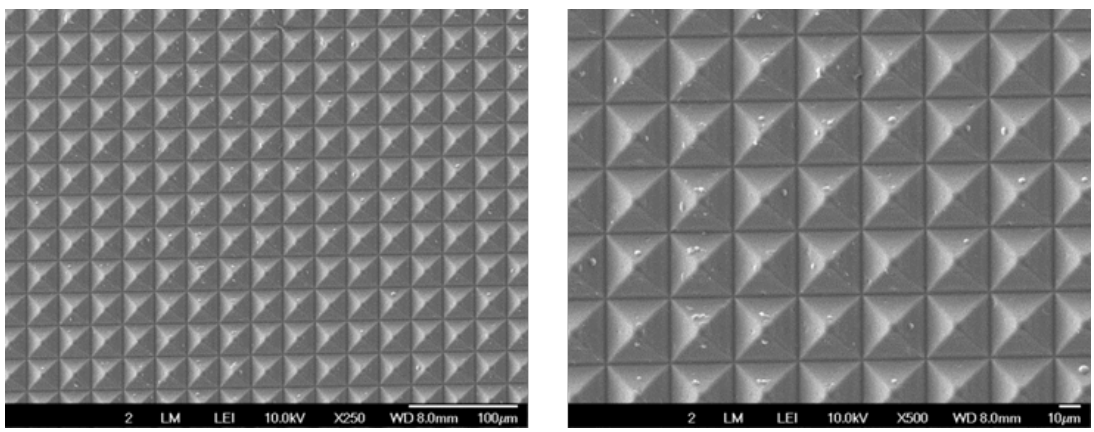

Figure III-1. SEM images of master mold with a pyramid pattern. The base length and height of the pyramids are 28 µm and 10 µm, respectively

III.2.2. Water flux test

The water flux of the PUA, track-etched and PVDF membranes was measured at three different pressures (2.5, 5 and 6 kPa), where the pressure was controlled by adjusting a two-stage regulator from a N_2 gas cylinder. The membrane (diameter of ~ 2.5 cm) was installed in a stirred cell (Millipore, USA), then pressurized N_2 gas was applied to the water reservoir to deliver deionized water to the stirred cell. The mass of filtrate was measured by balance at regular time intervals over a period of 20 min.

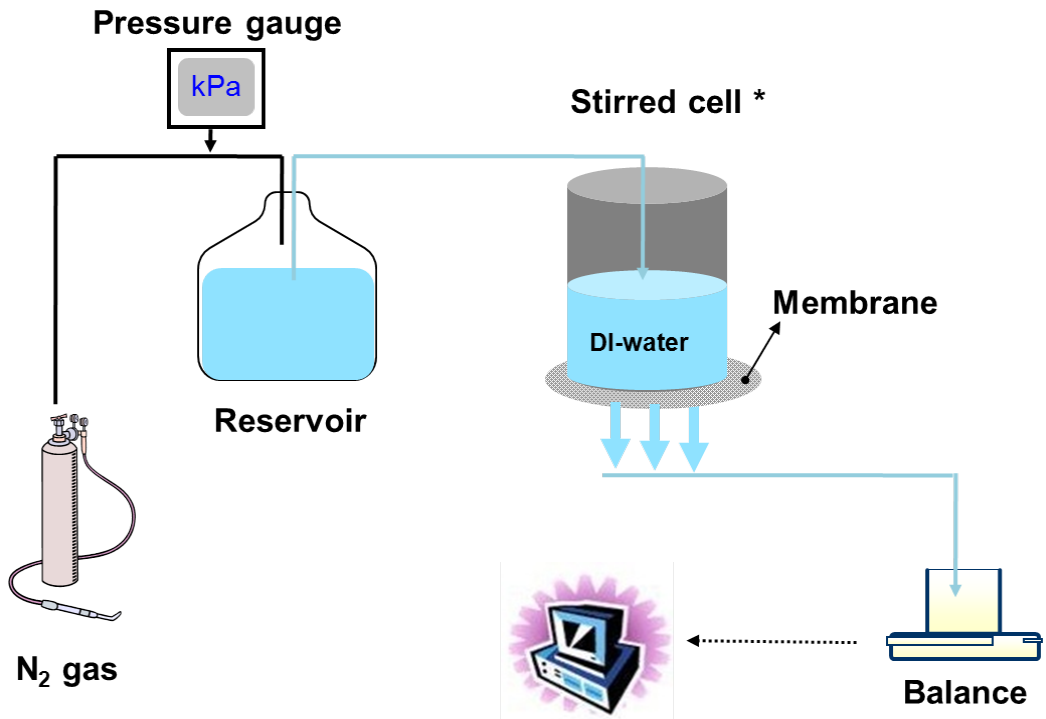

Figure III-2. Schematic diagram of the stirred cell for water flux measurements. To measure the flux of each membrane, membranes were installed in the stirred cell and the reservoir was filled with distilled water. Then, pressurized N_2 gas was used to deliver water to the stirred cell. The weight of the effluent was measured using a balance.

III.2.3. Particle separation test

Monodisperse colloidal polystyrene particles (1.1 μm and 300 nm in diameter) were purchased from Sigma-Aldrich. Each particle solution (10 μl) was mixed into DI water (2 mL), then the mixture solution was sonicated for 15 min to break up particle aggregates. A vacuum flask with a filter holder was connected to a vacuum pump. Then, an isoporous PUA membrane (pore diameter of ~1 μm) was installed in the filter holder and the solution (1 mL) was poured onto the membrane. The vacuum pump was turned on and the filtered solution was collected in a conical tube. Finally, the filtrate solution (1 mL) with 300 nm particles was drop-cast on a slide glass and dried at room temperature.

III.2.4. CDC biofouling test

Pseudomonas aeruginosa PAO1 tagged with green fluorescent protein (GFP) and carbenicillin resistance was applied to form a biofilm on the membrane surface. Tryptic soy agar (Difco, U.S.A) was dissolved in DI water and sterilized at 121°C for 15min. Then, carbenicillin (Gold Biotechnology, U.S.A) was added at a concentration of 200 μg/ml and the agar was solidified in a Petri dish. GFP-tagged *P. aeruginosa* was precultured on a tryptic soy agar plate for 1 day in an incubator at 37°C. Precultured GFP-tagged *P. aeruginosa* was inoculated in tryptic soy broth (Difco, U.S.A) and cultured for 1 day at 37°C in a shaking incubator (100 rpm). Cultured GFP-tagged *P. aeruginosa* was diluted in sterilized distilled water, then the concentration was adjusted to an optical density at 600 nm of 0.14. The biofilm formation test was performed in a CDC biofilm reactor (Biosurface Technologies Co., U.S.A). A schematic diagram of the CDC biofilm reactor experiment is shown in Fig S4. The CDC reactor and 1:100 diluted tryptic soy broth were sterilized before use. Tryptic soy broth was put in the CDC reactor and GFP-tagged *P. aeruginosa* was inoculated at 10^6 CFU/ml. The CDC reactor was operated in batch mode for 24 h, then 1:300 diluted sterilized tryptic soy broth was injected at 1.4 ml/min for 24 h. Finally, membranes were taken out of the CDC reactor after 48 h of operation and imaged by confocal laser scanning microscopy (CLSM).

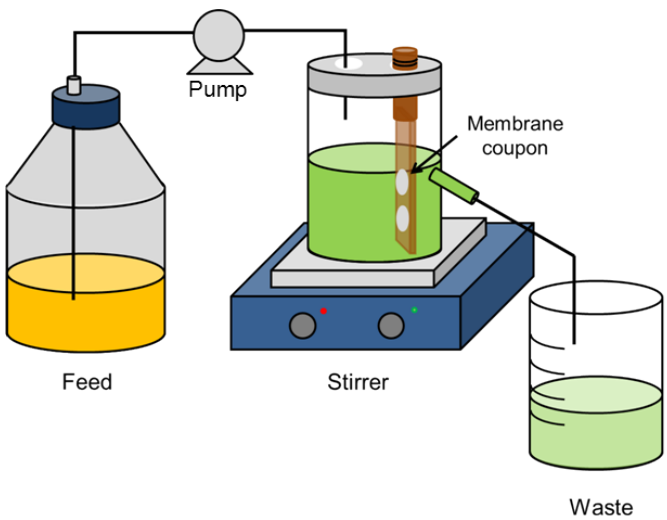

Operating condition

Feed	**Diluted tryptic soy broth (1/300)**
Temperature	**37 ℃**
Stirring rate	**100 rmp**
Operating time	**48 hrs**
Microorganism	***P. Aeruginosa* GFP tagged**

Figure III-3. Schematic diagram and operating conditions of the biofouling test with the CDC reactor.

III.2.5. Membrane characterization

SEM images were obtained on a JSM-6701F (Jeol, USA) and were analyzed by Image J (National Institutes of Health, USA) to calculate porosity. Using automatic color threshold adjustment in Image J, the colored pores and their areal fraction (i.e., surface porosity) were calculated automatically. Also, the pore size and distribution were measured on an NIS-Elements BR 3.2 (Nikon, Japan Surface zeta potentials were measured using an ELS-Z2 apparatus (Otsuka Electronics, Japan) with a quartz cell for flat samples. CLSM (C1 plus, Nikon, Japan) images were measured with a Planfluor 10X lens (N.A. 0.30, W.D 16 mm) and then visualized by IMARIS (Bitplane AG, Switzerland).

III.3. Results and discussion

III.3.1. Preparation of Tunable Pore Size Micro-sieve Membrane

Figure III-4 shows schematically the steps involved in the fabrication of micro-sieve membranes by the soft lithographic method. The master mold has an array of pyramids with a base and height of 28 μm*28 μm and 10 μm, respectively. An elastomeric PDMS stamp was poured and cured onto the master mold, yielding a negative replica of the master. Then, a working, disposable PSMAH replica was prepared from the PDMS stamp, which had the pattern features of the master. Applying a proper amount of PUA oligomer solution on the working PSMAH stamp, removal the vertical height of the casting knife. The working stamp with the cured PUA membrane on top was placed on a fabric support layer. Finally, the working stamp made of PSMAH was dissolved away by dipping the entire sample in toluene, leaving the PUA membrane on the surface of the fabric support. The adhesion between the cured PUA membrane and the fabric support was found to be good enough to easily pass the scotch-tape test, though the exact adhesion mechanism is still under investigation. The dissolved PSMAH material might play the role of an interpenetrating bridge to strongly anchor the PUA membrane onto the fabric surface. The presence of the fabric support is beneficial for the fabricated PUA sieve membrane in terms of mechanical strength, when compared to the free-standing, thin track-etched membrane. The final PUA membrane showed uniformity in terms of pore size (determined by the vertical height of the casting knife) and inter-pore distance (determined by the dimension of the pyramidal pattern on the master mold),

and can be designated an “isopore” sieve membrane. Note also that the pore size, distance between pores, and thus the porosity of the PUA membrane can easily be varied by using a master mold with a different pattern.

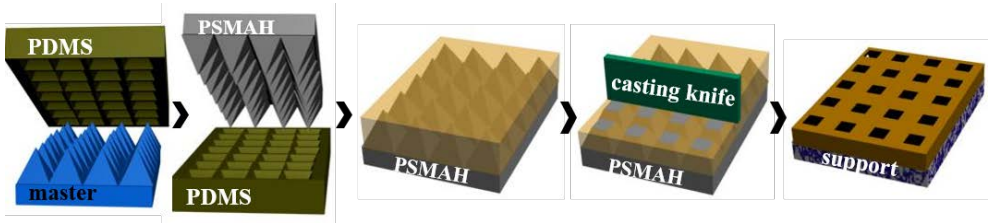

Figure III-4. Schematic representation of the process steps for the fabrication of soft-lithographically patterned micro/submicron-sieve membranes. A PDMS stamp that is replicated from a master mold is used to generate a working PSMAH stamp. Then UV-curable PUA oligomer solution is dispensed onto the working stamp and scraped with a casting knife. Finally, the fully cured PUA isopore membrane layer with the working stamp is dissolved on a fabric support, where the dissolving PSMAH material acts as a glue to attach the membrane onto the support. The same procedures can also be applied for master mold with submicron-sized features. Note here that the pore size of the isopore membrane can be easily be varied by adjusting the height of the casting knife in the fourth step for this pyramid-shaped master mold.

III.3.2. Surface pore characteristics of micro-sieve membrane

The fabricated membrane indeed had uniform pores, as shown in figure III-4. For comparison purposes, typical membranes prepared by phase inversion (figure III-5a) and by track-etching (figure III-5b) are also shown; the membrane fabricated using the phase inversion method had tortuous pores, with large scatter in pore size, while the track-etched membrane showed rather uniform pores with a few defects such as doublets/triplets indicated by red circles in the image. The membrane from the present soft-lithographic approach was very uniform and had a regular array of pores, as shown in figure III-5c and 5d, where the difference in pore size was controlled simply by changing the vertical height of the casting knife (figure III-6). By changing the height of the casting knife manually, the pore size can easily be varied from ~2 µm to >6 µm, corresponding to a porosity range from ~1% to ~5%, as shown in figure III-5e. With better control of the position of the casting knife (compared to manual control), a range of membranes, differing in pore size and thus in porosity, can be prepared from a given master pattern.

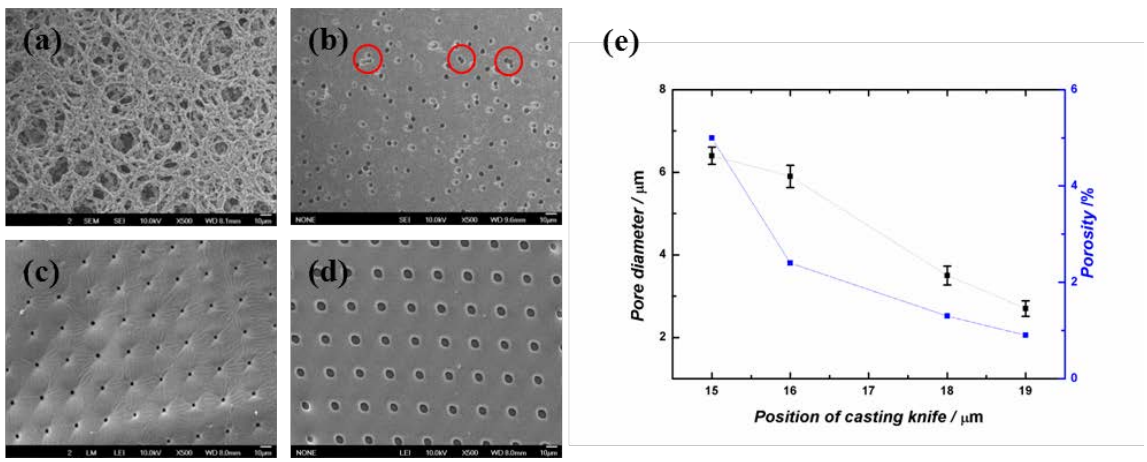

Figure III-5. Scanning electron microscopy (SEM) images of membranes. a) Commercial PVDF(polyvinylidene fluoride), and b) Commercial track-etched membranes, respectively. The red circles in b) show defective pores with doublets or triplets. c) and d) PUA isopore membranes with different pore sizes fabricated by simply adjusting the vertical height of the casting knife; pore size ~2.6 µm for c) and ~6.3 µm for d). e) Plot of pore size and porosity as a function of the vertical height of the casting knife. Values for the track-etched membrane shown in (b) are indicated in the plot for comparison purposes.

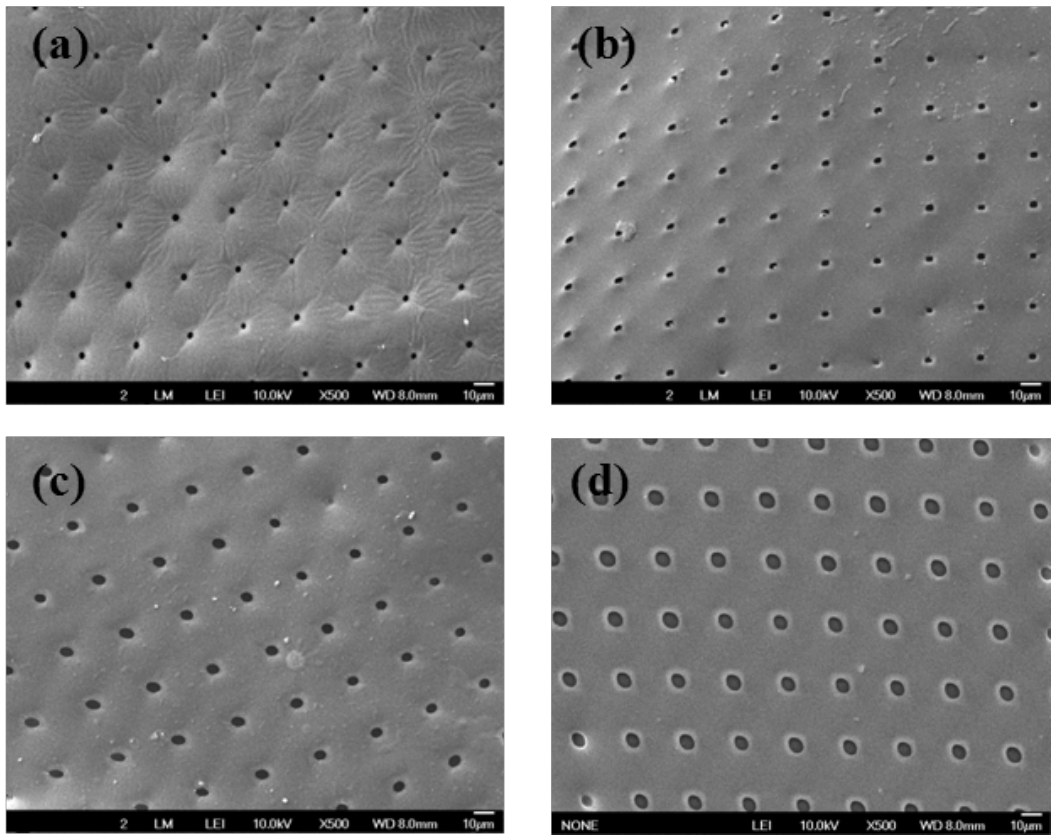

Figure III-6. SEM images of soft-lithographically fabricated micro-sieve membranes. The height of the casting knife was varied (manually) to obtain isopore micro-sieve membranes with different pore sizes, (a) ~2.7 µm, (b) ~3.5 µm, (c) ~5.9 µm and (d) ~6.4 µm, respectively. The pyramid-patterned Si master mold was used for these membranes. The final thicknesses of the micro-sieve membrane layer on the porous polyester support varied as well, from ~1 µm for (a) up to ~2.3 µm for (d).

III.3.3. Submicron-sieve Membrane Preparation and Surface Pore Characterization

The same principle was found to be applicable for the preparation of submicron-sieve membranes, using a master pattern of Si submicron pillars, as shown in figure III-7. For the fabrication of the submicron-sieve membrane (figure III-7b), a vertical array of Si submicron pillars (~700 nm in diameter and ~6 μm in length; figure III-7a) that was prepared by metal-assisted chemical etching (MaCE) (Huang et al. 2011) with a colloidal monolayer mask was used as the master mold. Note here that the pore size in the submicron-sieve membrane be the same to the pillar diameter on master mold. This is due to the uniform pillar diameter along its length, compared to slanted sidewalls in pyramid-shaped master for the preparation of micro-sieve membranes (figure III-4). This submicron-sieve membrane showed not only a much narrower distribution of the pore size, but also a more regular inter-pore distance than the track-etched membrane (figure III-7c, d). Further, the porosity was shown to be increased to >15% using such a submicron scale master pattern, more than 3-fold vs. the track-etched membrane having similar pore size, as shown in figure III-7e.

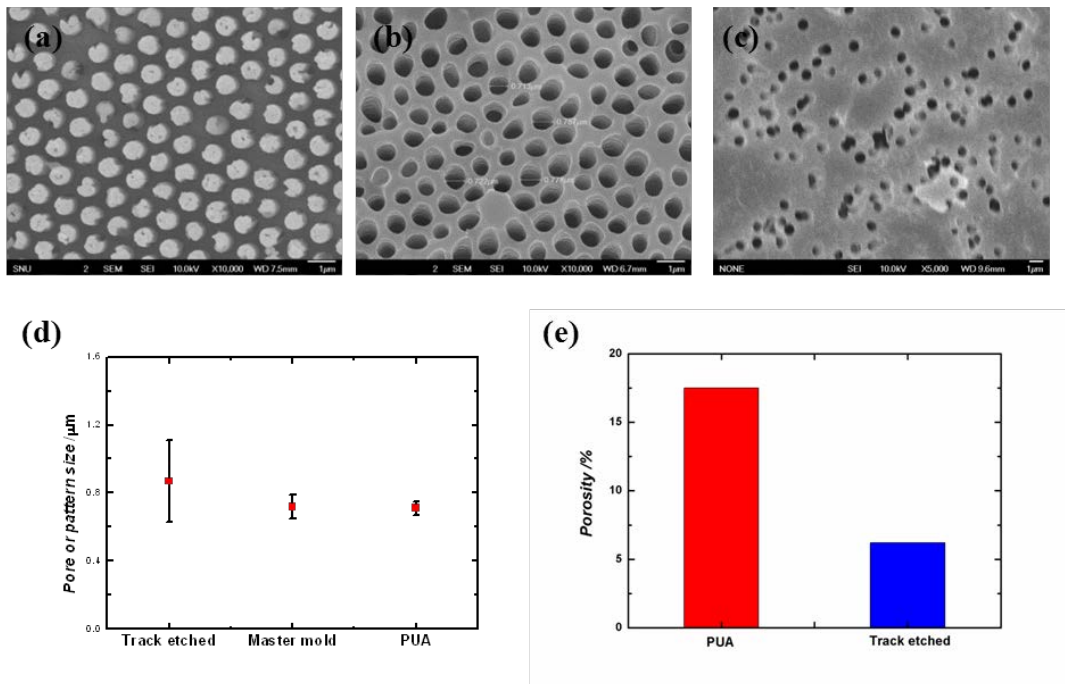

Figure III-7. SEM images of soft-lithographically fabricated submicron-sieve membranes. (a) Si master mold having vertical array of ~700nm Si pillars, (b) PUA membrane, and (c) Track-etched membrane, respectively. (d) Comparison of pore or pattern size in track-etched and PUA membranes. (e) Plot of the measured porosities for both membranes. Scale bars are 1μm for (a), (b), and (c).

III.3.4. Effect of straight pore structure and uniform pore size

The comparison of water flux was made between the three membrane types (PUA, track-etched and PVDF) with a nearly equal pore size of 5 μm in a stirred cell, as shown in figure III-8a and 8b. The absolute water flux through the soft-lithographically fabricated isopore membrane was lower than that through the phase inversion and track-etched membranes (figure III-8a). When the flux was normalized based on membrane surface porosity (figure III-8b), however, the PUA membrane showed much higher water flux than the phase inversion membrane (PVDF), but similar to the track-etched membrane. The surface porosity-normalized water flux was enhanced by more than 10-fold vs. the phase inversion membrane, due to the non-tortuous pore structure.

In addition to the advantages originating from the non-tortuous pore structure, the mono-disperse pore size can lead to the precise separation of mixtures differing in size into individual sizes. As a proof of concept, we tried to separate a mixture of colloidal polystyrene particles (1.1 μm and 300 nm) using the isopore membranes developed in this work. Figure III-8c shows the SEM images of the initial colloidal mixture, captured particles that are larger than the pore size (~1 μm) on membrane surface, and the permeate through the isopore membrane after separation, respectively. Indeed, the separation efficiency was 100%. Although we used particles with a large difference in size here for demonstration purposes, we believe that almost perfect sieving of mixtures based on size could easily be achieved after further optimization of the process.

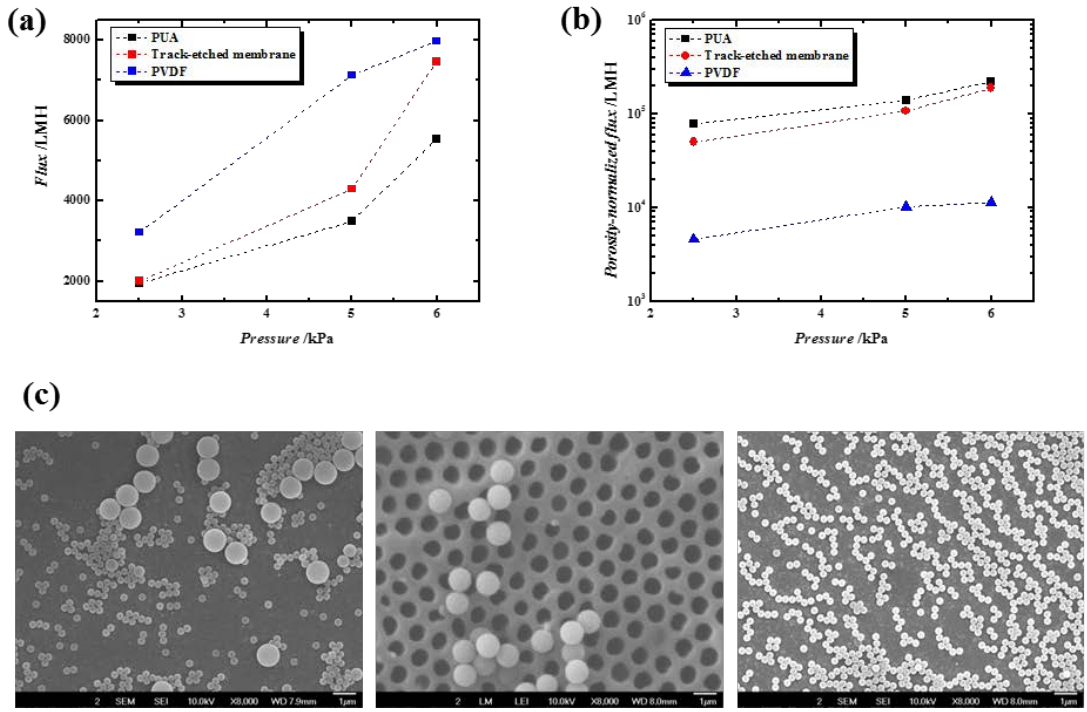

Figure III-8. a) Comparison of water flux through various membranes with different porosity by the stirred cell test. b) Semi-log plot of the normalized water flux based on the porosity of each membrane used in the flux measurements. c) SEM images of colloidal particles (mixture of 1.1 µm and 300 nm polystyrene colloids) before separation by the isopore membrane, on the membrane surface, and in the permeate after filtration, from left to right, respectively.

III.3.5. Anti-biofouling property of PUA material

When a new membrane is applied to water or wastewater treatment, its biofouling tendency is important because this is closely associated with energy consumption in the operation of membrane filtration. Consequently, PUA and track-etched membranes were tested for biofouling using the CDC reactor setup. Figure III-9a and 9b shows confocal laser scanning microscope (CLSM) images of biofilms deposited on PUA and track-etched membranes, respectively. The green color in the CLSM images indicates GFP-tagged *P. aeruginosa* adsorbed on the membrane surface. The PUA membrane unexpectedly showed much lower fouling tendency than the negatively charged track-etched membrane. In order to elucidate this tendency, the zeta-potentials of both membranes were measured as a function of solution acidity (figure III-9c). The zeta-potential of the PUA membrane surface showed a nearly constant value, ~0 mV, over the range of pH levels investigated here, indicating the chemical stability of the well cross-linked PUA membrane. On the other hand, the PVDF membrane showed variation in negative values (-30~-60 mV) depending on solution pH. Many studies have reported that a negatively charged membrane has lower fouling tendency than neutral or positively charged one (Chiang et al. 2012, Chon et al. 2013). This is because most particles, including microorganisms in natural water, are negatively charged near neutral pH and thus a negatively charged membrane causes a repulsive force between the membrane surface and particles. However, in spite of the nearly zero zeta-potential, the PUA membrane showed reduced biofouling. Therefore, in addition to zeta potential, we assessed the surface energy of each membrane to elucidate this unexpected result in

biofouling tendency between the PUA and track-etched membranes. As shown in Fig. S5, the surface energies of both membranes were calculated based on Fowkes theory (Fowkes 1962). The surface energy of the PUA membrane (34.4 mJ/m^2) turned out to be lower than that of the track-etched membrane (44.5 mJ/m^2) (figure III-9d). According to previous study, lower surface energy can lead to less biofouling tendency (Liu et al. 2005). Consequently, we assume that the lower surface energy of the PUA membrane could counterbalance its unfavorable zeta potential effect on biofouling and thus the PUA membrane might have less biofouling tendency than the track-etched membrane. This might be an additional advantage of the PUA membrane.

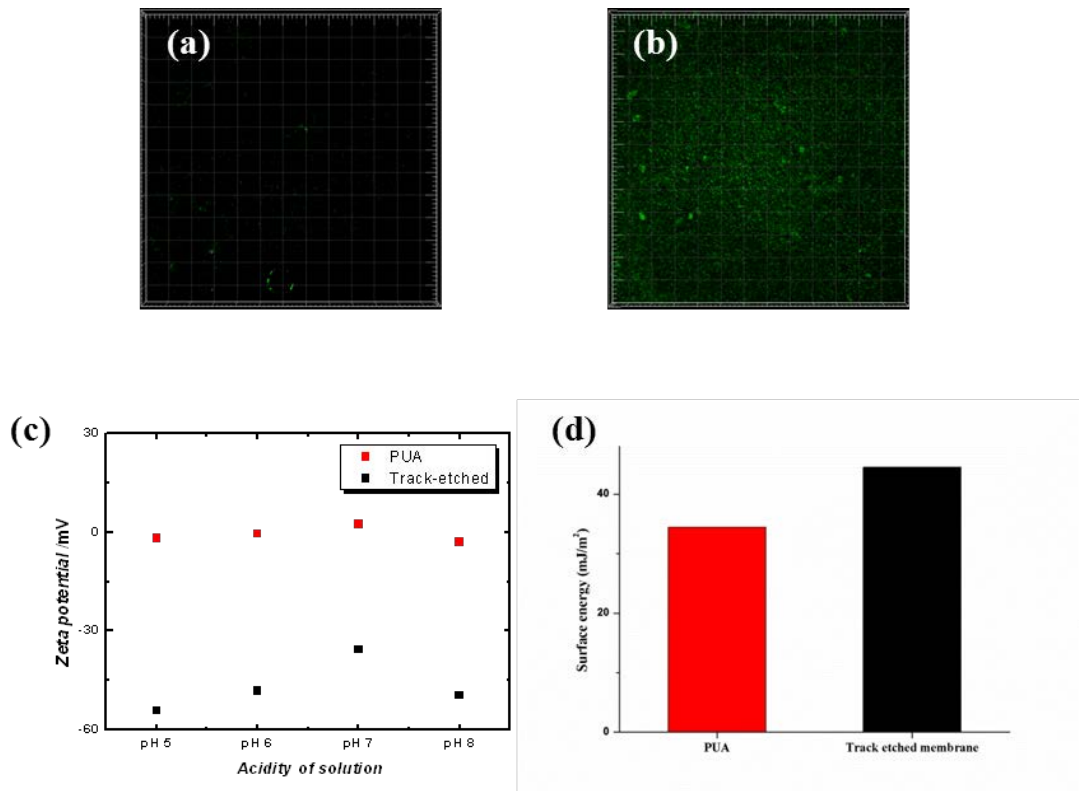

Figure III-9. CLSM images of biofilm on the a) PUA and b) track-etched microsieve membrane surfaces after 48 h of operation in CDC reactor. Green color indicates the P. aeruginosa in biofilm. Imaging area is ~1.2 mm*1.2 mm for both cases. c) ζ-potential of membranes and anti-biofouling characteristics. Variation of zeta-potential of PUA and TE membranes as a function of solution pH. d) Surface energy of PUA and track-etched membranes.

III.4. Conclusions

In summary, new micro- and submicron-sieve membranes were prepared using a soft lithography technique to provide a membrane material with low surface energy. The membranes have many advantages such as uniformity of pore size, deterministic spatial control of the pore distribution (or porosity), a non-tortuous pore structure and a lower biofouling tendency. The size (and uniformity) of pores and their spatial distribution can be not only precisely controlled by the patterns on the mold or stamp used, but also easily varied by simply changing the process conditions. The soft-lithographically patterned membrane had non-tortuous pores running through the entire thickness of the membrane, which was found to be very effective in increasing water permeability more than 1000 times compared to a conventional tortuous sieve membrane. In addition, the precise control and uniformity in pore size has enabled excellent fractionation of particles. Furthermore, the method involves much less volatile organics, making the process environmentally friendly. Releasing agent in PUA oligomer solution showed another advantage that its lower surface energy could lead to less biofouling. The low surface energy of PUA membrane might be a great help in the treatment of wastewater containing various microorganisms. Finally, the method can be carried out with any cross-linkable polymer materials other than PUA, based on specific requirements, thus greatly expanding the choice of membrane material and reducing the material cost compared to rather expensive PVDF.

Chapter IV

Three-dimensional hydraulic modeling of particle deposition on the patterned isopore membrane in crossflow microfiltration

IV.1. Introduction

Membrane processes have been widely applied to water and wastewater treatments because of their relatively simple operation and high selectivity. However, membrane fouling greatly reduces the economic feasibility of membrane processes and thereby restricts their extensive spread. Membrane fouling is induced by attachment or sorption of foulants such as natural organic matter, microorganisms, and numerous particles on the membrane surface, which subsequently leads to water flux decline, reduction of membrane lifespan and so on (Baker et al. 1998, Drew 2010)

A number of scientific and engineering approaches have been employed to mitigate membrane fouling. Among them, patterned membranes are an alternative way to reduce membrane fouling. Patterned membranes with various configurations and shapes have been prepared and tested. Patterned hollow-fiber membranes were fabricated from patterned nozzles and showed increased water flux compared with conventional hollow-fiber membranes (Çulfaz et al. 2010, Çulfaz et al. 2011a, Çulfaz et al. 2011b, Çulfaz et al. 2011c, Çulfaz et al. 2011d). Prism, pyramid, and embossed patterns were made on a flat sheet membrane surface and all of them showed anti-fouling properties induced by local turbulence and increased wall shear stress at upper region of the pattern (Won et al. 2012, Won et al. 2014). Modeling based on computational fluid dynamics (CFD) for hydraulic flow around the patterned membrane surface revealed that local shear stress distribution and vortex formation were the major reasons for anti-fouling effects of patterned membranes (Lee et al.

2013). However, most CFD modeling studies were two-dimensional, despite the fact that patterns have three-dimensional geometry. Moreover, because the models did not often take into account water permeation through membrane pores, the results obtained did not precisely reflect hydraulic flow around the patterned membrane surface during filtration. Furthermore, the patterned membranes used for such tests were usually by a phase inversion method, and thus their pore size distributions were broad due to many factors such as solvent, non-solvent, additives, and so on. Broad pore size distributions would decrease the selectivity of target solutes and thus reduce water quality of the permeate (Urase et al. 1996, Ohya et al. 1998). Although there had been attempts using track-etched isopore membranes with relatively uniform pore sizes, their applications were still limited due to their defects such as doublet and triplet pores and insignificant anti-fouling property (Tracey et al. 1994, Calvo et al. 1995, Martinezvilla et al. 1988, Ho et al 1999). Recently, studies for decrease pore defects have been carried out by applying self-assembly, anodization, and microelectochemicalsystems (MEMS) to isopore membrane fabrication process (Wan et al. 2012, Warkiani et al. 2013). The increased selectivity by ordered pore structure enabled high resolution size based separation of specific microorganism from tap water or cell mixture (Ou et al. 2014, Warkiani et al. 2011).

In this study, a patterned isopore membrane with reverse-pyramid patterns and a narrow pore size distribution as well was prepared by using UV-curable polymer and soft lithographic method. And then, factors affecting particle depositions on that membrane were investigated during the crossflow microfiltration of different micro-sized particles and their mixture. Three dimensional CFD

modeling was also carried out to analyze and elucidate particle depositions on the patterned membrane surface at various operating conditions for crossflow microfiltration.

IV.2. Materials and Methods

IV.2.1. Fabrication of patterned isopore membrane

Patterned isopore membranes were prepared by polymerization of uniformly coated polyurethane acrylate (PUA; 311RM, Minuta, Republic of Korea) oligomer solution on a pyramid-patterned polydimethylsiloxane (PDMS; Sylgard 184, Dow, USA) replica mold after replication of a reverse-pyramid patterned master mold (figure IV-1). The master mold was fabricated by the photolithographic method using nano-patterning organic devices at Seoul National University. The PDMS prepolymer was mixed with curing agent at a weight ratio of 10:1 and cast on a master mold with reverse-pyramid patterns. After trapped air bubbles were removed at room temperature for 1 h, the mixed PDMS solution was cured for 3 h at 60 °C (Campbell et al. 1999). The cured pyramid-patterned PDMS replica mold was detached from the master mold. Then, UV-curable PUA oligomer solution was applied to the PDMS replica mold surface (figure IV-1a). The excess PUA oligomer solution was removed during the spin-coating step. In this step the final surface pore size of patterned isopore membrane was controlled by the spinning rate (figure IV-1b). In this study, the spinning rate was fixed at 1850 rpm, and total spin coating time was 30 s. After the spin-coating, PUA oligomer solution was UV-cured at 365 nm for 2 h (figure IV-1c). Polymerized PUA film was detached from the PDMS replica mold (figure IV-1d) and attached to the fabric support layer to increase mechanical strength. The PUA reverse-pyramid patterned isopore membranes were observed with a scanning electron microscope (SEM; JSM-6701F, Jeol, USA) and

the pore size and distribution were measured on an NIS-Elements BR 3.2 (Nikon, Japan).

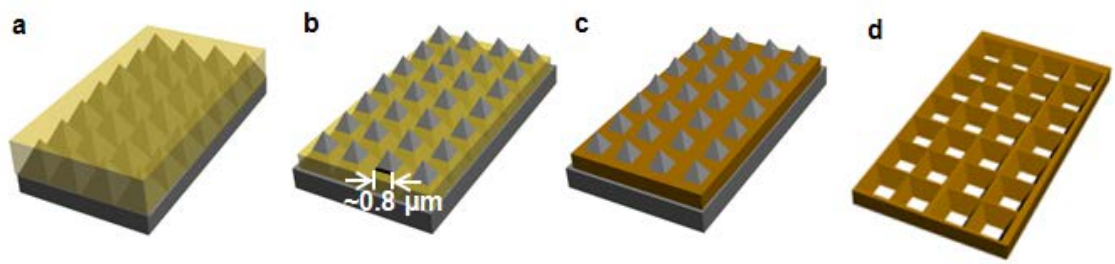

Figure IV-1. Schematic diagram of fabrication steps for the patterned isopore membrane. UV-curable PUA precursor solution was (a) dispensed on a pyramid-patterned PDMS replica mold and (b) spin-coated at 1850 rpm. (c) The PUA oligomer solution was polymerized by UV-curing at 365 nm for 2 h. (d) Finally, reverse-pyramid patterned PUA membrane was detached from the PDMS mold.

IV.2.2. Particle depositions during crossflow microfiltration

The effects of the patterned isopore membranes on polystyrene particle depositions were investigated during the crossflow microfiltration under various conditions such as cross-flow velocity and pore water flux. The polystyrene particle was selected as foulant due to its similar density (1.05 g/cm3) and negative zeta potential with bacteria in water treatment process. In the cross-flow microfiltration system (figure IV-2), the PUA membrane was installed on a lab-scale membrane module measuring 20 mm in channel length, 20 mm in channel width and 2 mm in channel height. A peristaltic pump was connected to the permeate line of the membrane module to control the pore water flux. The cross-flow velocity was controlled by a circulation pump and a valve next to the module and monitored with a flowmeter. 2 μm (2 wt%) and 5 μm (10 wt%) polystyrene latex bead suspensions (Sigma Aldrich, USA) were used to prepare feed suspensions for the crossflow microfiltration and 160 μL of 2 μm or 5 μm suspension were diluted into 800 mL of deionized (DI) water. The mixed suspension of 2 μm and 5 μm latex beads was prepared by adding 35 μL of 2 μm latex bead suspension to 60 μL of 5 μm suspension and then the mixed suspension was diluted with 800 mL of DI water.

Operating conditions for microfiltration runs were as follows. Crossflow velocity (V_c) was selected as either 0.25 or 0.42 m/s and each operation pressure was 8.3 or 21.1 kPa respectively. Pore water flux (J_p), defined by water permeation rate through a membrane pore located at the bottom of each reverse-pyramid pattern, had the same unit as that of V_c (m/s). J_p was adjusted such that the ratio of V_c to J_p was 100

or 1000, i.e., V_c was 100 or 1000 times higher than J_p. When $J_p = V_c/100$ or $J_p = V_c/1000$, they were designated as "high J_p" or "low J_p," respectively. For instance, at $V_c = 0.25$ m/s with low J_p , low J_p is equal to $V_c/1000 = 2.5 \times 10^{-4}$ m/s. Crossflow microfiltration for 2 μm particles was conducted with a combination of $V_c = 0.25$ or 0.42 m/s and at high or low J_p. Those for 5 μm and mixed particles were performed with a combination of 0.25 or 0.42 m/s and only low J_p. After each filtration run, the PUA membrane covered with deposited particles was detached from the membrane module and analyzed by SEM.

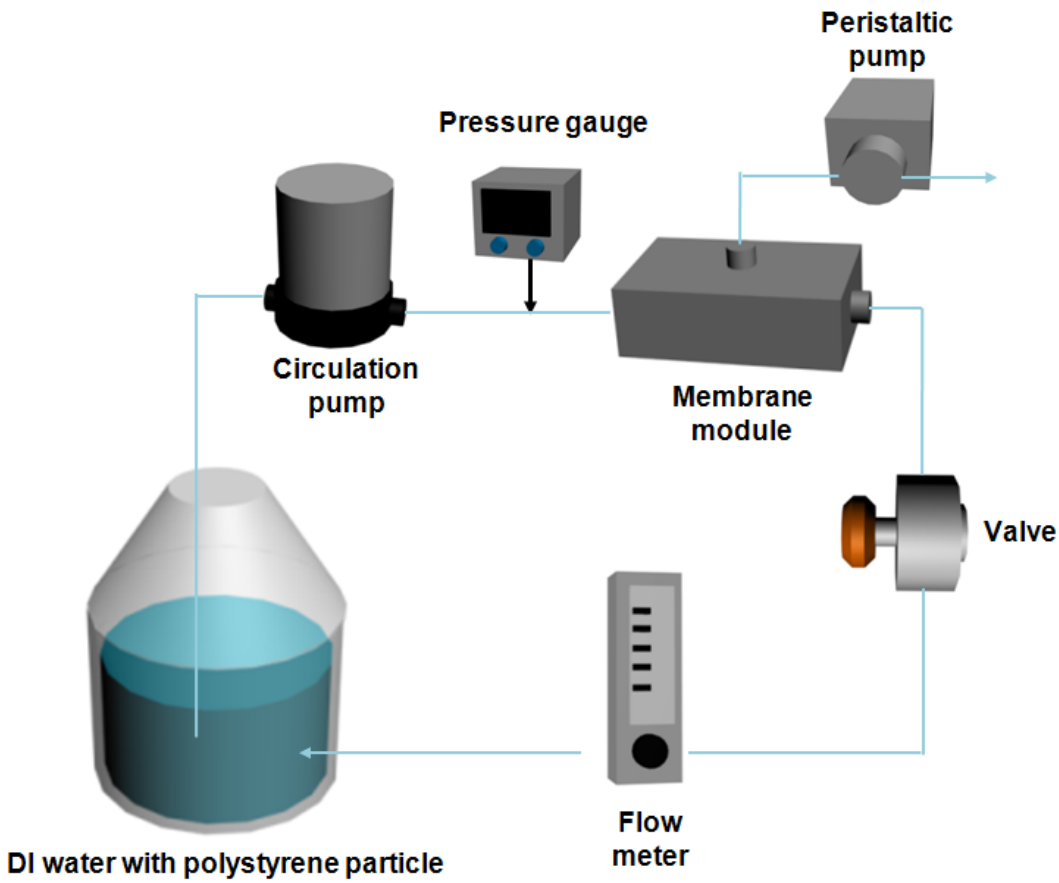

Figure IV-2. Schematic diagram of the crossflow filtration experimental set-up. A peristaltic pump was connected to the permeation line of membrane module to control the pore water flux.

IV.2.3. Numerical method

Three-dimensional hydraulic modeling was conducted to analyze fluid stream lines in the vicinity of the isopores on the patterned membrane surface. The Navier-Stokes and fluid continuity equations for the incompressible Newtonian fluid were discretized and solved by the finite element method (FEM). A 3-D rectangular channel was constructed and used as a simulation domain where reverse-pyramid patterns were engraved on the bottom side. The overall domain size was 75 μm (width) × 150 μm (length) × 2000 μm (height), and the size of each pattern was 25 μm (width) × 25 μm (length) × 16 μm (height), which corresponded to the pattern size of the membrane used for the filtration experiment. The number of elements was 57 864, and fine meshes were generated near the membrane surface to solve complicated flow behavior with accuracy (figure iV-3). The density and viscosity of the fluid (water) were assumed to be 1 g/mL and 1 g/(m·s), respectively.

Boundary conditions were assigned as follows. Under a fully developed flow assumption, the velocity of the fluid was imposed at the inlet as where Umax was the maximum vc, h channel height, and z the coordinate. The crossflow Reynolds number (Rech) was defined as where ρ was the density of the fluid and μ the viscosity of the fluid. The maximum crossflow velocities (U_{max}) were 0.375 and 0.63 m/s, which correspond to the average crossflow velocity, V_c = 0.25 and 0.42 m/s, and to the crossflow Reynolds number, 910 and 1 400, respectively. Water permeate velocities through membrane pores were fixed at 1/100 or 1/1000 of V_c at each filtration modeling. At the upper boundary, velocity was equal to that of the fully

developed flow under the assumption of negligible effects of the surface patterns. The pressure boundary condition ($p = 0$) was assigned at the outlet, and no-slip boundary conditions were applied at the other boundaries. The calculation was performed by using a commercial software (COMSOL Multiphysics ver. 4.2, Comsol Inc., USA). Calculation results were presented as colored stream lines showing the distribution of flow velocity and flow direction. In addition, flow velocities were presented as numeric values at a specific position to compare the effect on the detachment of differently sized particles.

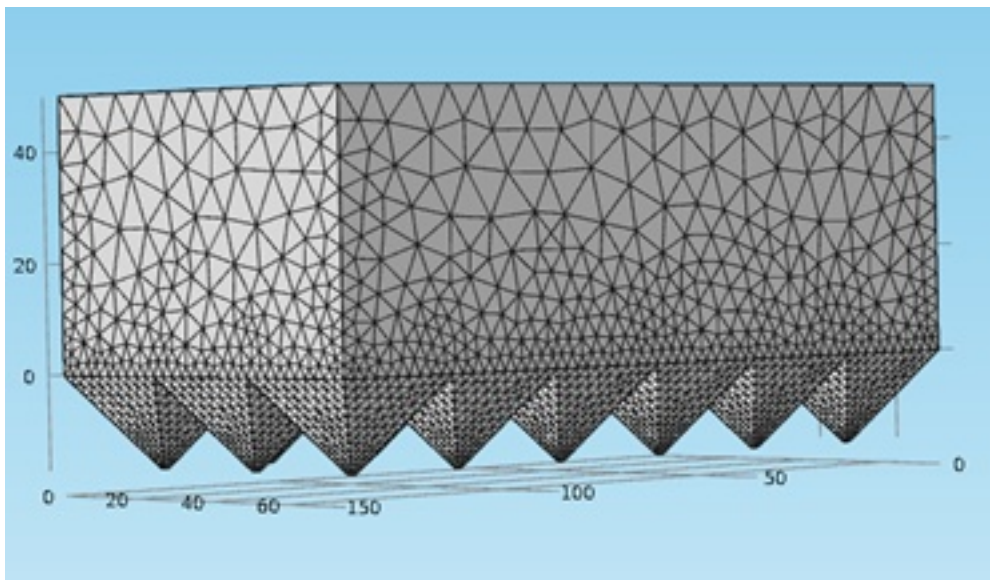

Figure IV-3. Overall domain of computational fluid dynamics modeling . The overall domain size was 75 µm × 150 µm × 2000 µm (width × length × height) and the size of each pattern was 25 µm × 25 µm × 16 µm. The number of elements was 57,864 and fine meshes were generated near the membrane surface to solve complicate flow behavior with accuracy.

IV.3. Results and discussion

IV.3.1. Conformation of a reverse-pyramid patterned membrane

The reverse-pyramid patterned membranes with rectangular isopores were fabricated and their SEM images are shown in figure IV-4. Reverse-pyramid patterns were regularly arrayed on the whole PUA membrane surface (figure IV-4a and 4b), and each pattern was 25 μm wide and 16 μm high. figure IV-4c shows the square pores. figure IV-4d was obtained after inversion of the patterned membrane to confirm regularly located pores. The pore size, defined by the length of the long side of a rectangular pore located at the bottom of the pattern, was largely dependent on the spinning rate. Higher spinning rate yielded a thin PUA coating layer, leading to larger surface pores on the PUA membrane because the cross-sectional area of the pyramid became larger when a cutting plane was positioned at the lower level (figure IV-5). On the other hand, lower spinning rate yielded a thicker PUA coating layer, leading to smaller surface pores on the PUA membrane. The pore size and distribution were shown in figure IV-6. The average pore size was around 0.8 μm with 0.08 standard deviation at the spinning rate of 1850 rpm.

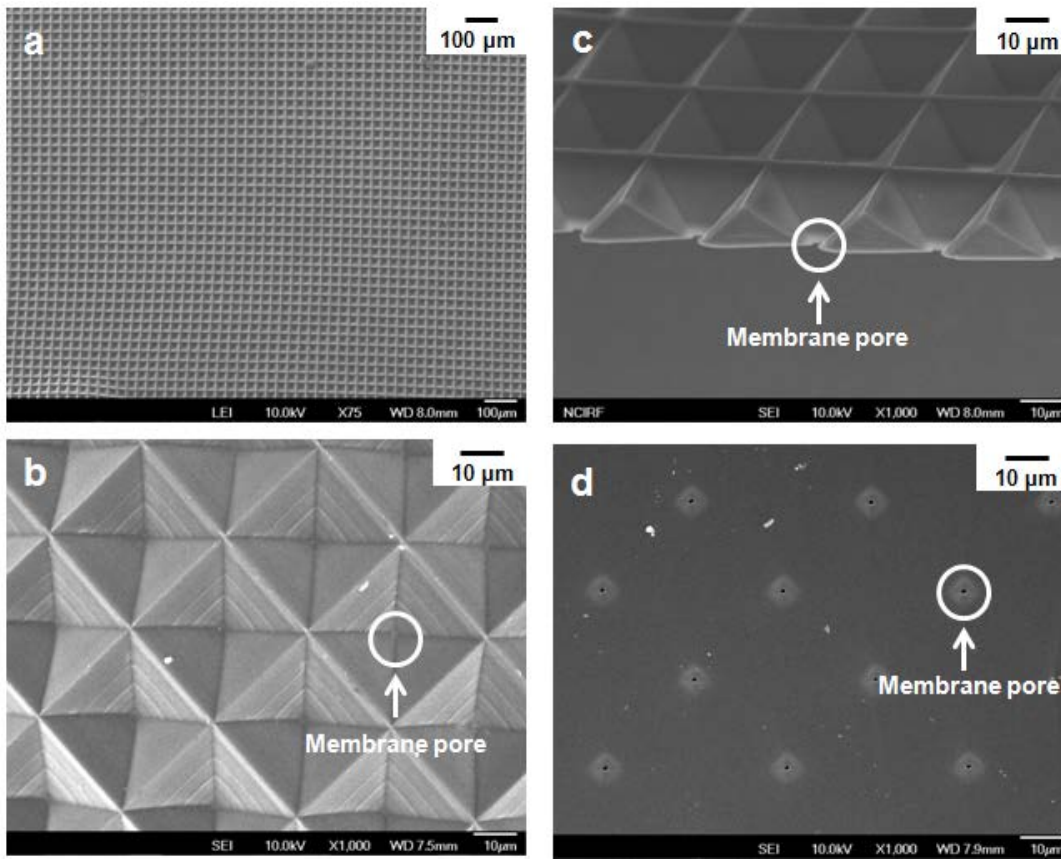

Figure IV-4. SEM images of (a, b) surface (c) cross-section, and (d) rear of the patterned isopore membrane.

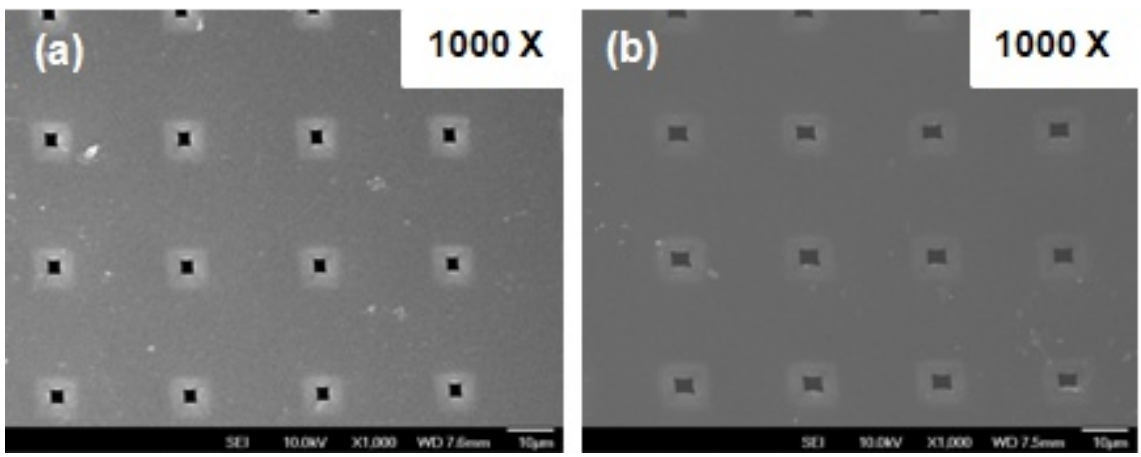

Figure IV-5. SEM images of PUA membrane prepared at different rotation rates. (a) 2400 and (b) 2500 rpm. Higher rotation rate gave rise to larger membrane pore size.

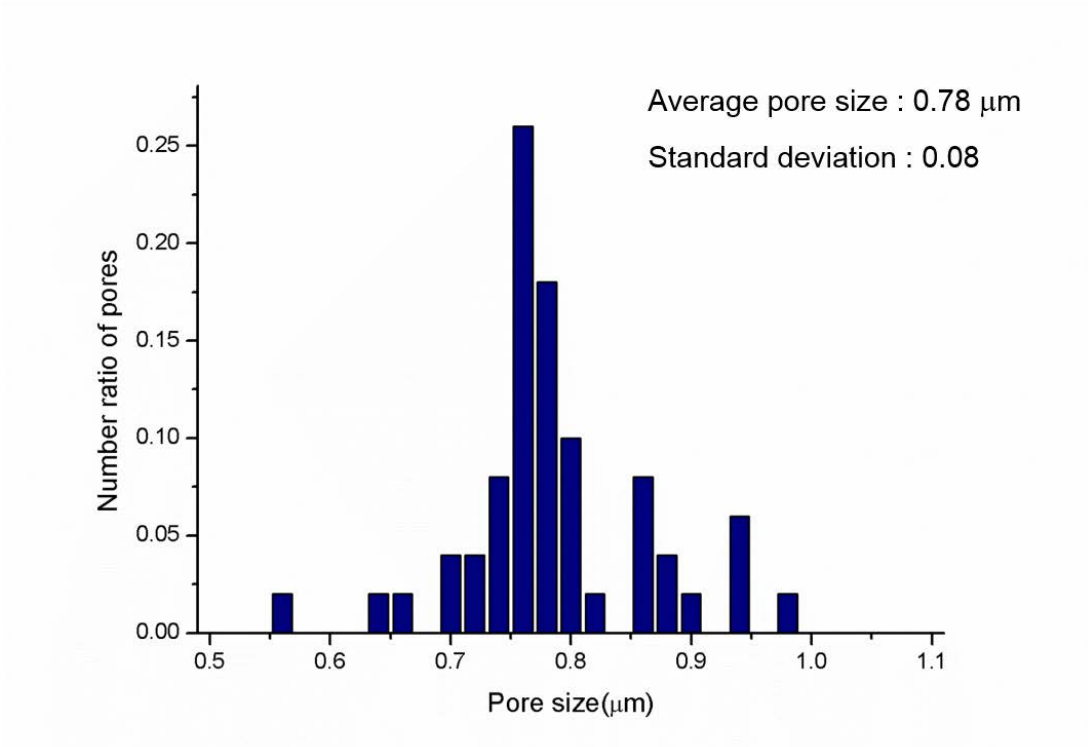

Figure IV-6. Average pore size and pore size distribution of PUA membrane. The average pore size of PUA membrane was around 0.8 μm and its deviation was 0.08

IV.3.2. Deposition of 2 μm particles on the patterned isopore membrane surface

Figure IV-7 shows the SEM images of four patterned isopore (0.8μm) membrane surfaces after the crossflow microfiltration of suspensions with 2 μm particles (beads) under different crossflow velocity (V_c) and pore water flux (J_p). The crossflow direction was from left to right on the membranes in figure IV-7. As shown in figure IV-7, at lower V_c (= 0.25 m/s) with low J_p, most of the 2 μm particles were deposited on the left upper region in each reverse-pyramid pattern, making a straight line. Conversely, particle deposition was negligible on the lower region in each reverse-pyramid pattern. In comparison with the flat surface of the flat membrane, a flow stream such as vortex could be generated on the patterned membrane surface, which possibly prevented particles from colliding with and then depositing on the membrane surface, or moved away particles already deposited. However, detachment of deposited particles may be less probable near the left upper region. These phenomena are discussed in Section IV.3.4.

At high V_c = 0.42 m/s with low J_p, most of the 2 μm particles were deposited on the upper region in each reverse-pyramid pattern, but few particles were seen on the lower region in each pattern (figure IV-7b), just as in figure IV-7a. However, the number of particles deposited in figure IV-7b was much greater than that in figure IV-7a. A numerical calculation study in a reverse osmosis membrane system with a feed spacer reported that at higher V_c more particles accumulated on the membrane surface. Higher V_c causes more chance of collisions between membrane surface and

particles and thus gives rise to more particle depositions. On the other hand, at V_c = 0.25 m/s with ten times higher J_p, the trend of particle deposition was very different. Some particles moved into each reverse-pyramid pattern without any regularity (figure IV-7c). This could be caused by the change of flow stream lines near the membrane pores owed to the increase of J_p. It is also analyzed through CFD modeling below.

Most of the particles on the upper region (figure IV-7b) at high V_c = 0.42 m/s with low J_p disappeared, but many more were seen on the lower region in each pattern when J_p was augmented (figure IV-7d). The change from figure IV-7c to figure IV-6d was similar to that from figure IV-7a to figure IV-7b and could be attributed to the increase of V_c. The deposition of many more particles at the bottom, even jamming the membrane pore in each pattern (figure IV-7d), could be attributed to both higher V_c and J_p. High J_p should create a faster, wider stream toward the membrane pore than low J_p.

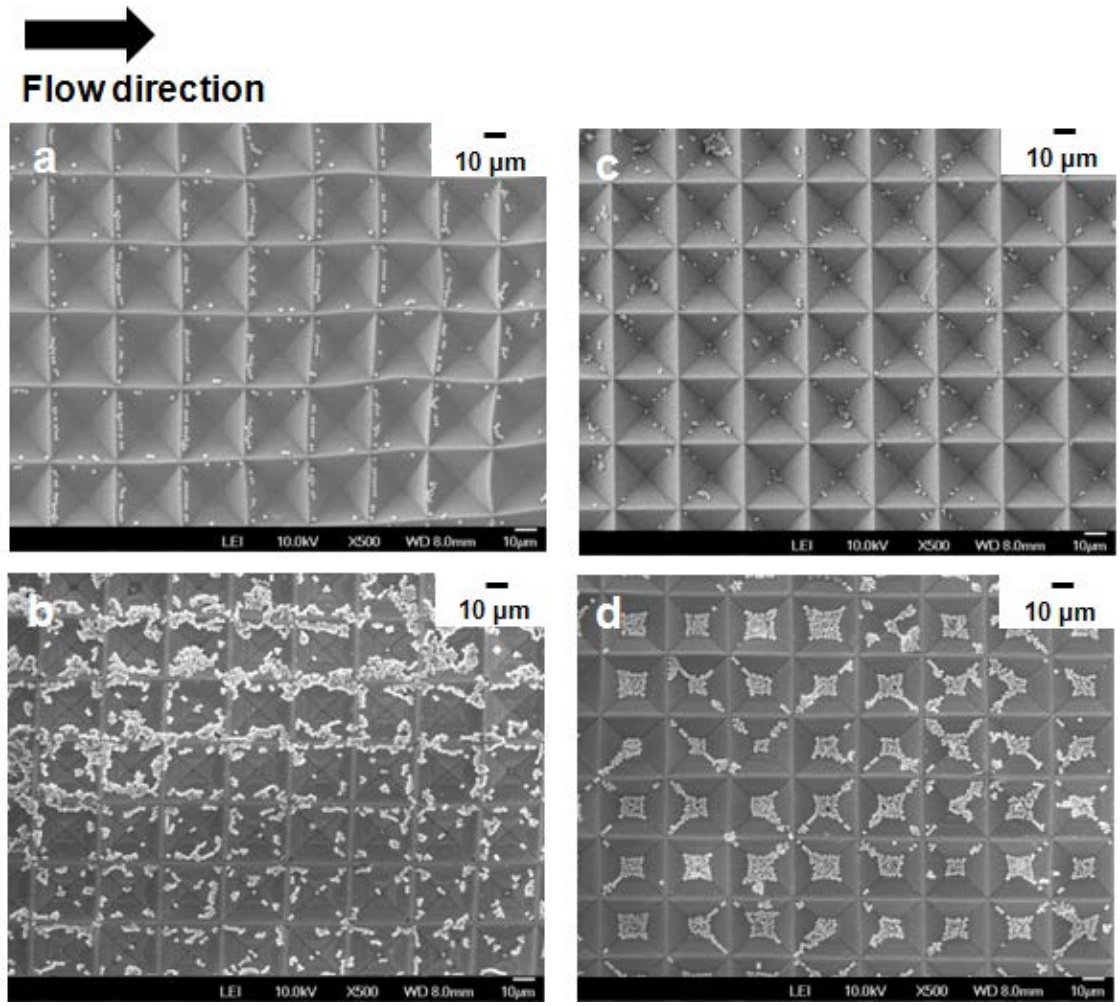

Figure IV-7. SEM images of particle depositions on the membrane surfaces after crossflow microfiltration of 2 µm particles (a) at V_c = 0.25 m/s with low J_p (=V_c/1000 = 2.5 X 10^{-4} m/s), (b) V_c =0.42 m/s with low J_p (=V_c/1000 = 4.2 X 10^{-4} m/s), (c) Vc = 0.25 m/s with high J_p (=V_c /100 = 2.5 X 10^{-3} m/s), and (d) V_c =0.42 m/s with high J_p (=V_c /100 = 4.2 X 10^{-3} m/s).

IV.3.3. Deposition of 5 μm particles or mixture of 2 and 5 μm particles on the patterned isopore membrane surface

When the particle size in the feed suspension increased from 2 μm to 5 μm, the trend of particle depositions on the patterned isopore (0.8 μm) membrane surface was quite different from that of 2 μm particles even at the same V_c and J_p. At low J_p, most of the 2 μm particles were deposited on the upper region in each reverse-pyramid pattern as mentioned above (figure IV-7a and 4b). At the same low J_p, however, most of the 5 μm particles were found around the bottom in each reverse-pyramid pattern rather than on the upper region at both V_c = 0.25 m/s (figure IV-8a) and V_c = 0.42 m/s (figure IV-8b). Because of the different cross-sectional area, larger particles (5 μm) would be influenced by the flow stream differently from smaller particles. This is discussed in Section IV.3.4.

Particles of both sizes (2 and 5 μm) were mixed together and fed into the crossflow microfiltration at the operating conditions of V_c = 0.25 m/s with low J_p. In contrast to figure IV-7a for 2 μm particles at the same operating conditions, 5 μm particles were located at the bottom, even jamming the membrane pore in each pattern (figure IV-9), and were similar to those in figure IV-8. However, 2 μm particles were not deposited any longer on the upper region in the reverse- pyramid pattern but randomly scattered on the pattern surface (figure IV-9). At higher V_c = 0.42 m/s (figure IV-9b'), the trend of deposition was similar to figure IV-9a' except there was a much larger number of deposited particles. During the microfiltration of the

mixture of 2 & 5 μm particles, 5 μm particles which were trapped near the membrane pore located center bottom in each pattern may have modified flow stream lines, leading to the change in the deposition of smaller 2 μm particles. This is discussed in Section IV.3.4.

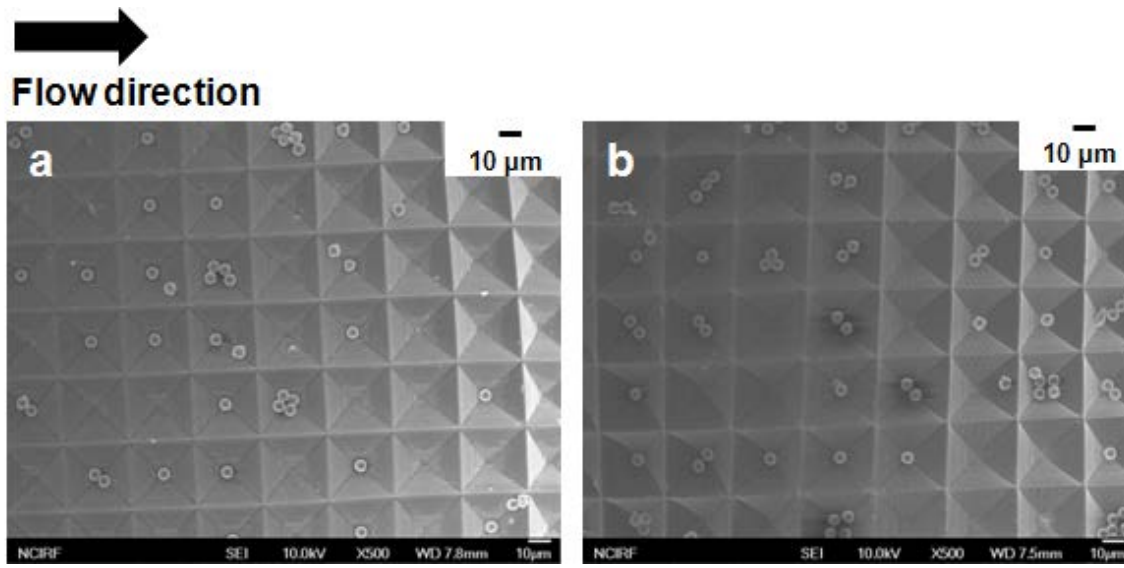

Figure IV-8. SEM images of particle depositions on the membrane surfaces after crossflow microfiltration of 5 µm particles (a) at V_c = 0.25 m/s with low J_p ($J_p = V_c$ 1000 = 2.5 X 10^{-4} m/s), and (b) V_c = 0.42 m/s with low J_p (= V_c /1000 = 4.2 X 10^{-4} m/s).

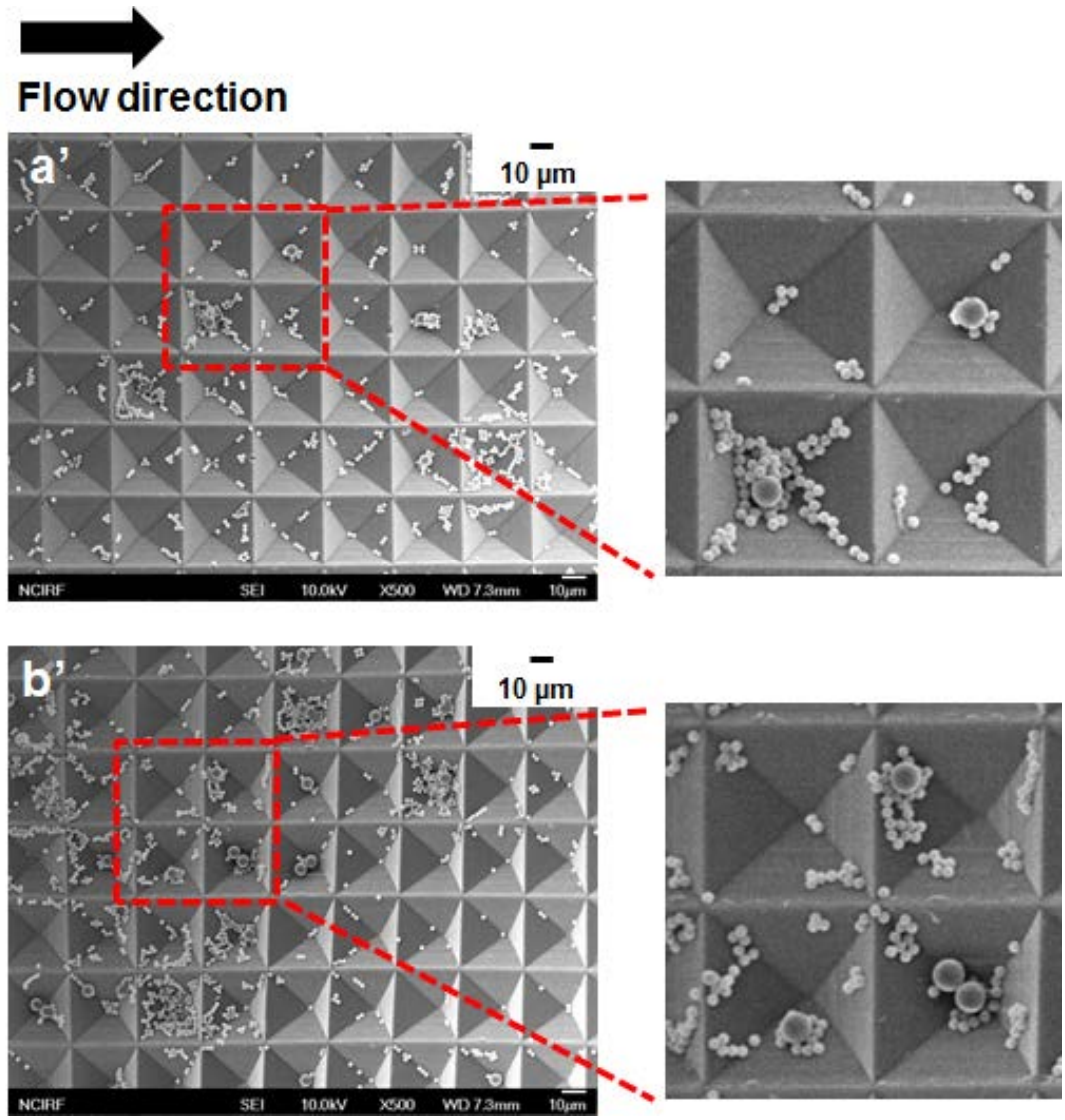

Figure IV-9. SEM images of particle depositions on the membrane surfaces after crossflow microfiltration of mixture of 2 and 5 μm particles (a') at V_c = 0.25 m/s with low J_p ($J_p = V_c /1000$ = 2.5 X 10-4 m/s), and (b') V_c = 0.42 m/s with low J_p (= $V_c /1000$ = 4.2 X 10-4 m/s). Magnified SEM images are presented at right side of each SEM image.

IV.3.4. Hydraulic flow characteristics on the patterned membrane surface

Figure IV-10 shows 3-D CFD modeling of water flow on the reverse-pyramid patterned isopore (0.8 μm) membrane surface. The red and blue colors of the horizontal bar indicate higher and lower water stream velocities, respectively. Even though the modeling was accomplished in three-dimensional space, only the front-viewed images were provided in all cases (figure IV-10a-d and 7a'-b') in order to aid interpretation of the flow streams largely dependent on the crossflow velocity (V_c) and pore water flux (J_p). In general, two distinct hydraulic flow characteristics appeared on the reverse-pyramid patterned membrane surface: one was the bulk stream lines flowing from left to right in the lateral direction and the other was the vortex stream lines in the inner space of each reverse-pyramid pattern. The bulk and vortex streams were well separated from each other, which made it difficult for smaller particles to move from the bulk to the vortex streams and thus reduced the deposition of smaller particles inside the reverse-pyramid pattern.

At V_c = 0.25 m/s with low J_p (=V_c/1000 == 2.5 x 10-3 m/s), the vortex stream lines were almost fully developed and formed inner circles inside the pattern, but very few lines headed down toward the membrane pores, as shown in figure IV-10a. Consequently, it would be difficult for particles to move away from the vortex streams toward the bottom and then deposit inside the reverse-pyramid pattern. Instead, collisions between particles and membrane surface would mainly occurred at the upper region in the reverse-pyramid pattern and thus 2 μm particles were

deposited mostly on the upper region in figure IV-7a. Although the stream lines at V_c = 0.42 m/s with low J_p (=V_c /100= 4.2 x 10-3 m/s) in figure IV-10b are similar to those in figure IV-10a, the number of deposited particles increased greatly, as shown in figure IV-7b. This might be attributed to the increase of collision frequencies at higher V_c. It is worth noting in figure IV-7a that most of the 2 μm particles were located on the left upper region. It might be partly because the wall at the left side of deposited particles might prevents them from being moved away to the right direction together with the water flow.

On the other hand, at V_c = 0.25 m/s with high J_p (=V_c /100= 2.5 x 10-3 m/s), some of the vortex stream lines deviated from the inner circles and went toward the membrane pore located on the center bottom of each pattern, as shown in figure IV-10c and 10d. Consequently, particles were deposited not on the upper region but at the bottom of each pattern, as shown in figure IV-7c. That trend was aggravated at V_c = 0.42 m/s with high J_p (=V_c /100= 4.2 x 10-3 m/s) because of the increase of both collision frequencies and pore water flux, as shown in figure IV-7d.

When the particle size in the feed suspension increased to 5 μm, the particle movement would be influenced more significantly than 2 μm particle by the flow stream because larger surface area should be exposed to the water stream. In this context, flow velocities directed toward both 2 and 5 μm particles located at the upper region in each pattern (Point X) in figure IV-10a and 10b, respectively, were calculated using CFD modeling. At V_c = 0.25 m/s with low J_p (=V_c /1000= 2.5 x 10^{-3} m/s) in figure IV-10a, the flow velocity toward 2 μm particle at point X was

8.58×10^{-5} m/s, whereas that toward 5 μm particle at the same point X was 7.61×10^{-4} m/s. At V_c = 0.42 m/s with low J_p (=V_c /1000= 4.2 x 10-3 m/s) in figure IV-10b, the flow velocity toward 2 μm particle at point X was 1.29×10^{-4} m/s, whereas that toward 5 μm particle at the same point X was 1.25×10^{-3} m/s. In other words, the impact of water flow exerted toward 5 μm particles would be almost ten times greater than that toward 2 μm particles. That greater impact could make 5 μm particles move more easily from the bulk stream to the vortex stream and ultimately move down toward and deposit on the bottom of the each pattern as shown in figure IV-8a and Fig. 8b even at lower pore water flux, J_p (=V_c /1000). However, as the impact on 2 μm particles was much weaker, 2 μm particles would have difficulties in moving from the bulk stream to the vortex stream. That is why figure IV-8a and 8b for 5 μm particles are in striking contrast to figure IV-7a and 7b for 2 μm particles, although the operating conditions for the microfiltration of both suspensions are identical.

When 2 and 5 μm particles were mixed together in the feed suspension, the trend of particle deposition was quite different from that with single particles, especially for 2 μm particles. Despite the same filtration condition as in figure IV-7a and 7b for both V_c and J_p, 2 μm particles were hardly seen on the upper region of each pattern, but they were scattered throughout each pattern (figure IV-9a' and 9b'). In order to elucidate such interesting phenomena, we assumed that a 5 μm particle was trapped near the membrane pore inside each pattern and then 3-D modeling was conducted under the same operating condition as in figure IV-10a and 10b (i.e., V_c = 0.25 and 0.42 m/s with low J_p, respectively). The results of the modeling are

depicted in figure IV-10a' and 10b'. Unexpectedly, the flow stream lines in figure IV-10a' and 10b' did not match those in figure IV-10a and 10b which were obtained at the same V_c and J_p, except for the trapped 5 μm particle. In figure IV-10a' and 10b', the flow stream lines toward the membrane pore located at the center bottom of each pattern were enhanced, which could enhance the migration of 2 μm particles from the upper to the lower region inside each pattern. That is why 2 and 5 μm particles were scattered inside the reverse-pyramid pattern as shown in figure IV-9.

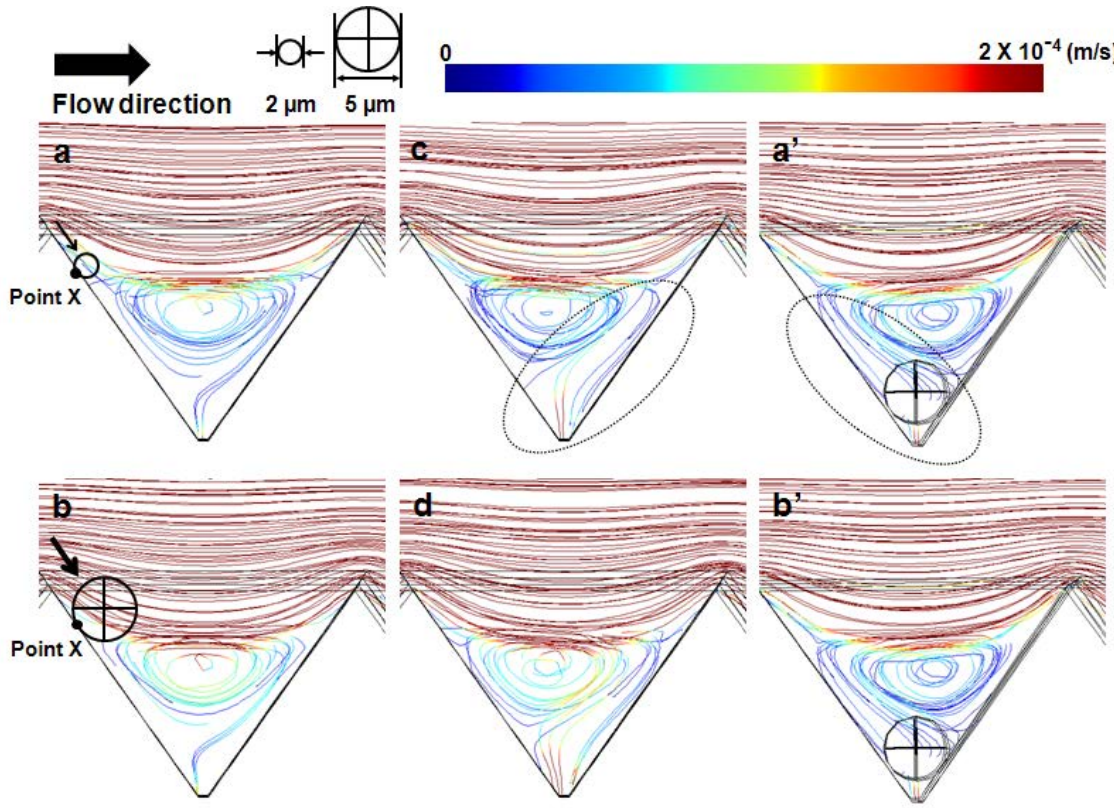

Figure IV-10. Stream lines estimated by 3-D modeling near the patterned isopore membrane surface: (a) V_c = 0.25 m/s with low J_p (=V_c /1000 = 2.5 X 10^{-4} m/s), (b) V_c = 0.42 m/s with low J_p (=V_c /1000 = 4.2 X 10^{-4} m/s), (c) V_c = 0.25 m/s with high J_p (=V_c /100 = 2.5 X 10^{-3} m/s), and (d) V_c = 0.42 m/s with high J_p (=V_c /100 = 4.2 X 10^{-3} m/s), (a') V_c = 0.25 m/s with low J_p (=V_c /1000 = 2.5 X 10^{-4} m/s) and (b') V_c = 0.42 m/s with low J_p (=V_c /1000 = 4.2 X 10^{-4} m/s). For (a') and (b'), the stream lines were estimated, assuming that a 5 μm particle was trapped around the pore in each reverse-pyramid pattern. The blue and red colors of the horizontal spectrum indicate the lower and higher water stream velocity, respectively.

IV.4. Conclusions

A patterned isopore membrane with reverse-pyramid patterns on its surface and a narrow pore size distribution was prepared from UV-curable polymer by the soft lithographic method. Factors affecting particle depositions during the crossflow microfiltration were investigated with experiments as well as with 3D modeling under various operating conditions and feed compositions. In the light of the results, the following conclusions were drawn.

- A rectangular pore was formed in the center of each reverse-pyramid pattern and its size was dependent on the spinning rate of a PDMS replica mold with excess PUA oligomer solution.
- The number and position of particle depositions on the patterned surface were largely dependent on the crossflow rate (Vc), pore water flux (Jp) and size of particles in the feed suspension. Particularly, for the microfiltration of the mixed suspension with different particle sizes, the deposited larger particles affected the flow stream lines, which in turn influenced the deposition of smaller particles.
- Three-dimensional CFD modeling revealed that two stream lines (bulk and vortex) were generated on the surface of the reverse-pyramid patterned membrane and were in accordance with the trends of particle depositions during the microfiltration.

Chapter V

Effects of pattern shape and orientation on fouling behavior

V.1. Introduction

Membrane process is one of the effective technologies which can alleviate the global water shortage phenomenon. However, membrane fouling has been considered as the major obstacle, causing flux decline, membrane life cycle reduction, and increase of operating cost.

Patterned membrane has been one of the suggested solutions for membrane fouling. Hollow fiber patterned membrane for water treatment was fabricated and its antifouling effect was investigated (P. Z. Çulfaz 2010, P. Z. Çulfaz 2011a, P. Z. Çulfaz 2011b, P. Z. Çulfaz 2011c, P. Z. Çulfaz 2010d). Type of hollow fiber membrane was limited to 'line and space' due to continuous fabrication process with patterned nozzle. Membranes with diverse pattern shapes were prepared by combining soft lithographic method and NIPS (Won et al. 2012). Microporous flat sheet membranes with pyramid and prism pattern were fabricated and antifouling effect of each membrane was verified. Patterned hollow fiber membrane was prepared by using soft lithography and straw. The process enabled fabrication of pyramid patterned hollow fiber membrane. However, while the previous researches investigated an increased water flux and fouling resistance, the effect of pattern shape and orientation on the membrane fouling has not been investigated.

Lee et al. introduced computational fluid dynamics (CFD) to reveal the pattern effect by analyzing shear stress and stream near the membrane surface. They found that the shear stress distribution and stream were changed and affect fouling behavior comparing with flat membrane. However, the modeling was conducted two

dimensionally and water permeation which affects stream and particle deposition was not considered.

In this study, flat, pyramid, 45° rotated and reverse-pyramid patterned microfiltration membranes were fabricated by using soft lithography and NIPS. In order to investigate difference of fouling resistance between the membranes, particle deposition experiment was carried out and the fouling behaviors were explained by three dimensional CFD modeling results.

V.2. Materials and Methods

V.2.1. Materials

Polydimethysiloxane (PDMS, sylgard 184) and curing agent were purchased from Dow Corning. Anhydrous *N*,*N*-Dimethylformamide (DMF), polyvinylidene fluoride (PVDF) with 275,000 molecular weight, polystyrene latex bead, and reagent grade acetone were obtained from Sigma Aldrich. All reagents were used without further purification. The polystyrene particle was selected to simulate single bacteria cell because of its comparable properties. The density and zeta potential of particle were 1.05 g/cm^3 and -55.6 mV respectively. Non-woven fabric for membrane supporting layer was provided from Woongjin Chemical.

V.2.2. Preparation of patterned MF membrane

Patterned MF membranes were prepared by using pyramid or reverse-pyramid pattern shaped PDMS mold. Overall membrane fabrication steps were referred from Won et al. 2012. PDMS oligomer solution and curing agent were mixed with 10:1 weight ratio and poured onto patterned master mold. After removing air bubbles for 1 h, the PDMS solution was cured at 60 °C oven for 2 h. The cured PDMS replica mold was peeled off from master mold.

Weight ratio of PVDF, DMF and acetone was 2 : 5.5 : 3 for PVDF solution. 2 g of PVDF pellets was dissolved in 5.5 g of DMF and 3 g of acetone mixture solution at 60 °C for 24 h then the PVDF solution was sonicated for 2 h to remove air bubbles. After cooling down the PVDF solution to room temperature, 0.3 g of PVDF solution was casted onto the 3 X 3 cm sized PDMS mold. Non-woven fabric was put up on the casted PVDF solution and the PVDF solution was percolated to the non-woven fabric for 30 s. The PDMS mold with PVDF solution and non-woven fabric was dipped into tap water at room temperature and coagulated for 24 h to remove residual solvents. After coagulation, patterned or flat membrane was peeled off from PDMS mold and stored at deionized water. Schematic diagram of membrane fabrication procedure is shown in figure V-1.

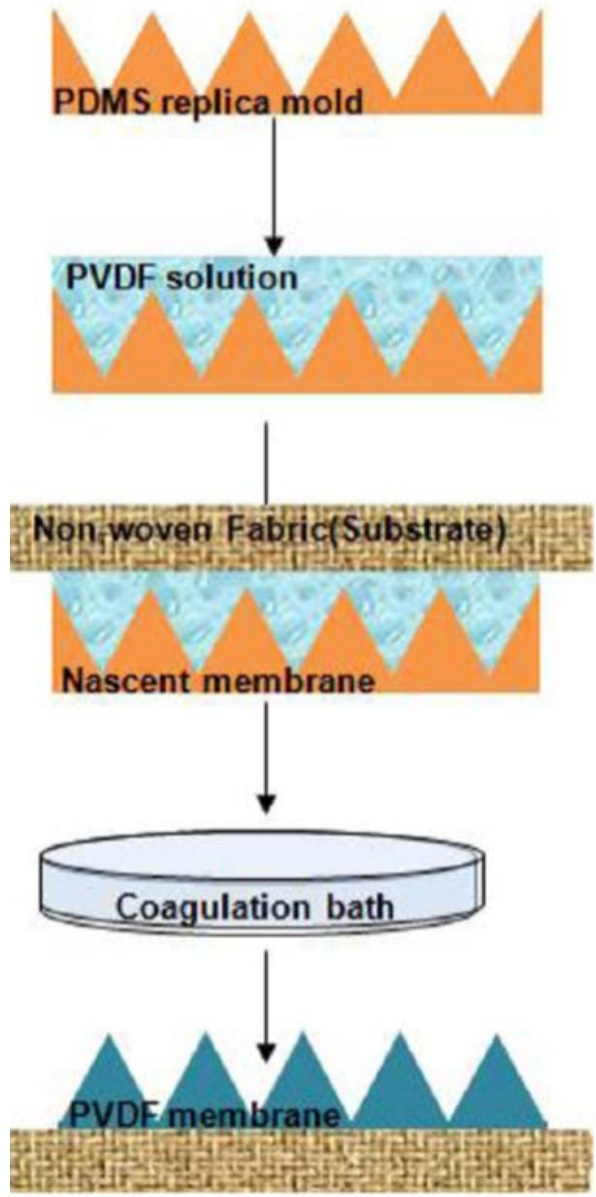

Figure V-1. Schematic diagram of patterned membrane fabrication (Won et al. 2012)

V.2.3. Pure water flux measurement of MF membrane

The pure water fluxes of pyramid, reverse-pyramid, 45° rotated, and flat membrane were measured at crossflow microfiltration system as depicted in figure V-2. Prepared membrane was equipped at membrane module and valid membrane area in the module was 4 cm^2 with 2 cm length and 2 cm width. After membrane compaction at 50 kPa for 2 h, water fluxes were measured at 5, 10, and 15 kPa respectively.

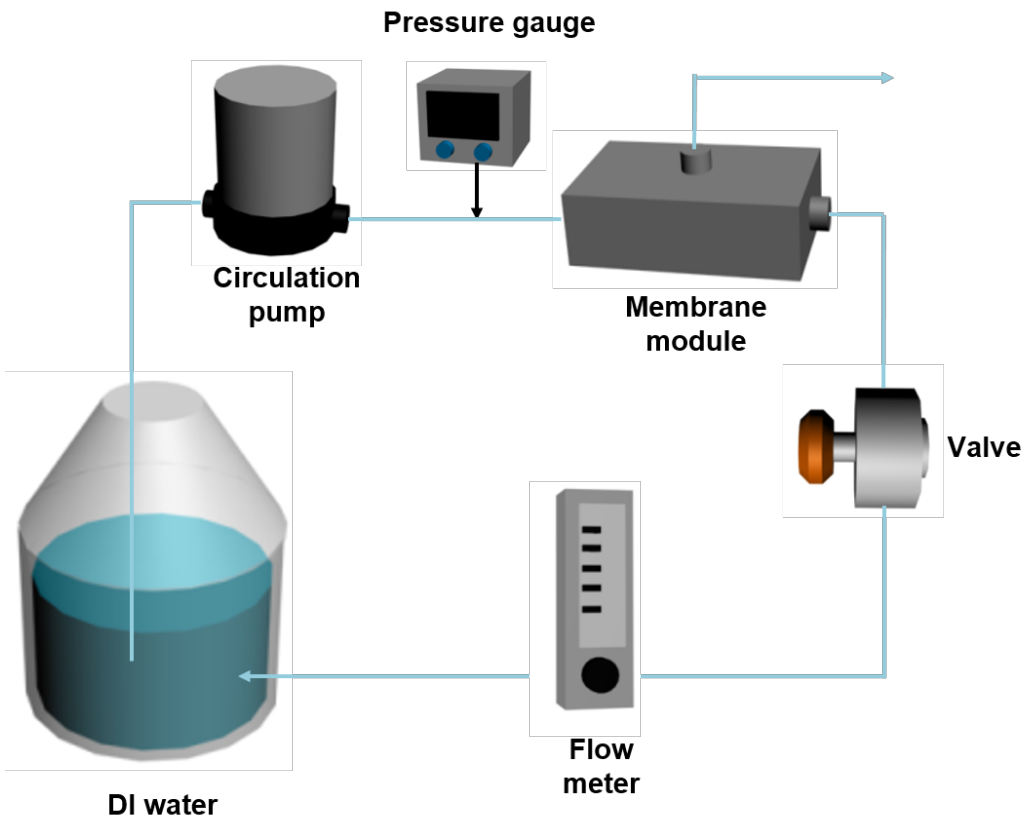

Figure V-2. Schematic diagram of crossflow microfiltration system

V.2.4. Particle deposition experiment

The effect of each patterned membrane on particle depositions were inspected by using cross filtration system as depicted in figure V-2. 1.1 μm polystyrene particles were suspended at deionized water to be 2.5 wt% and sonicated for 2 h before each particle deposition experiment. 600 μl of the 2.5 wt% polystyrene particle solution was diluted with 800 ml of deionized water at resovoir.

Operating conditions for microfiltration runs were as follows. Crossflow velocity and operating pressure were maintained as 0.21 m/s and 5 kPa during 20 min operation respectively. After each crossflow run, the membrane was cut and put into 15 ml conical tube with 1 ml deionized water to confirm the amount of deposited particle. The conical tube with membrane and deionized water was sonicated for 1 h to detach deposited polystyrene particles and turbidity of solution was measured by spectrophotometer (Mecasis, Republic of Korea) at 300 nm wavelength.

V.2.5. Numerical method

Three-dimensional hydraulic modeling was conducted to analyze fluid stream lines and wall shear stress at membrane surface. The Navier-Stokes and fluid continuity equations for the incompressible Newtonian fluid were discretized and solved by the finite element method. A rectangular parallelepiped channel was constructed as real membrane module and each pattern shape, pyramid, reverse-pyramid and 45° rotated pyramid, was created on the bottom side. Size of overall domain was 75 μm (width) × 150 μm (length) × 2000 μm (height), and the each pyramid or reverse pyramid size were 25 μm (width) × 25 μm (length) × 17 μm (height) that is identical with real pattern size on the membrane. The finer meshes near the membrane surface than bulk space were made to solve complicated flow behavior with accuracy.

Under a fully developed flow assumption, the velocity of the fluid was imposed at the inlet where U_{max} maximum crossflow velocity, h channel height, and z the coordinate. The maximum crossflow velocity was 0.21 m/s, and Reynolds number was 760 that is laminar flow region. The water permeation was assumed to be occurred at whole membrane surface and result of water flux test was employed to modeling. At the upper boundary, velocity was equal to that of the fully developed flow under the assumption of negligible effects of the surface patterns. The pressure boundary condition ($p = 0$) was assigned at the outlet, and no-slip boundary conditions were applied at the other boundaries. The calculation was performed by using a commercial software (COMSOL Multiphysics ver. 4.2, Comsol Inc., USA).

Calculation results were presented as colored stream lines showing the distribution of flow velocity and flow direction and as colored area presenting the distribution of wall shear stress of patterned membrane surface.

V.3. Results and discussion

V.3.1. Membrane characterization of flat and patterned membranes.

SEM images of each membrane surface are shown at figure V-3. Pyramid and reverse-pyramid patterns were formed with high fidelity while each membrane has sub-micro pores at surface and sponge like structure at cross section. The pure water fluxes of flat, pyramid, reverse-pyramid and 45° rotated pyramid patterned membrane were evaluated. The water fluxes of patterned membranes were around 1.4 times higher than flat membrane at each operating pressure as shown at figure V-4. The membrane surface area of patterned membrane was 1.36 times higher than that of flat membrane and the enhanced membrane surface area caused increase of water flux as Won et al. 2012.

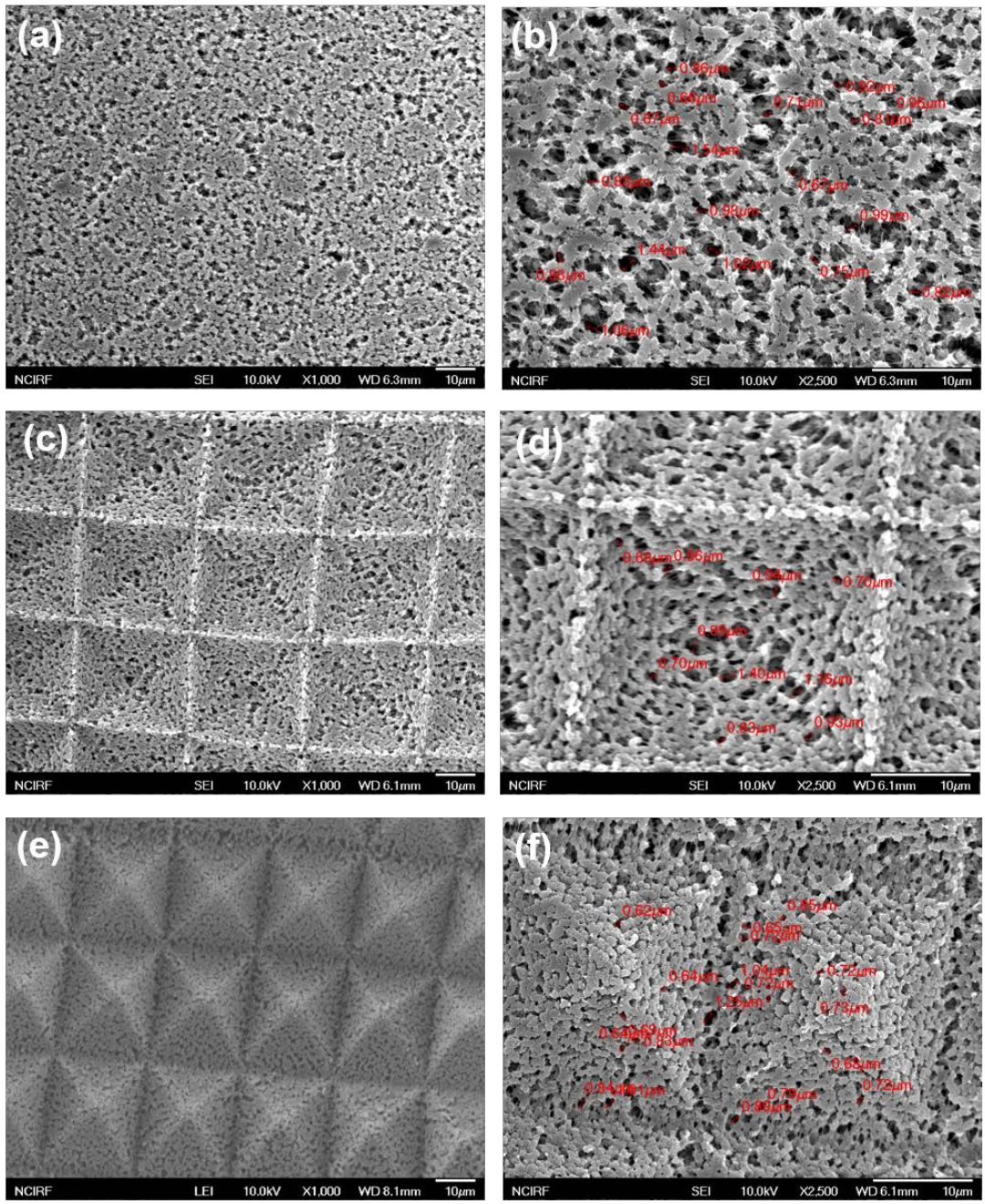

Figure V-3. SEM images of (a) flat membrane (X1000), (b) flat membrane (X2500), (c) reverse-pyramid membrane (X1000), (d) reverse-pyramid membrane (X2500), (e) pyramid membrane (X1000), and (f) pyramid membrane (X2500)

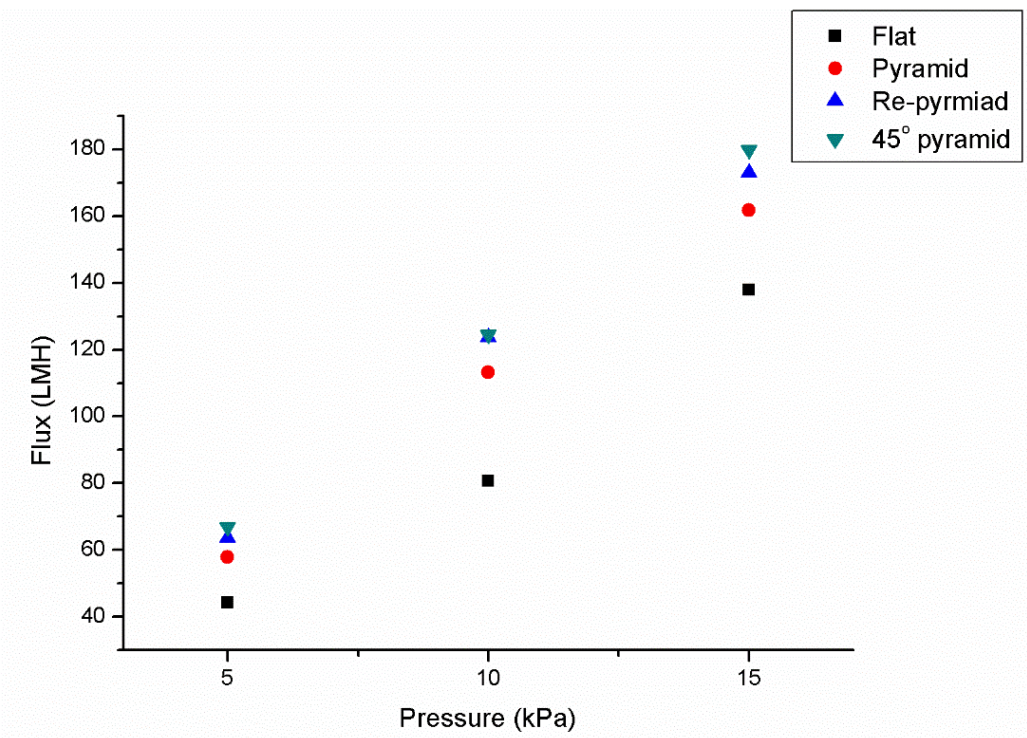

Figure V-4. Water fluxes of flat and patterned membranes

V.3.2. Particle deposition on flat and patterned membrane surface

The amounts of deposited particles are shown in figure V-5. According to the measured particle deposition amount, membrane fouling was decreased at all kinds of patterned membrane compared with flat membrane.

The amounts of deposited particles were varied with pattern shape and orientation. Reverse-pyramid membrane was fouled by polystyrene particles substantially while 45° rotated pyramid pattern showed the lowest fouling behavior among patterned membranes under experimental condition listed in section V.2.4. Correspondence of pattern shape and orientation with fouling behavior will be discussed by applying three dimensional modeling in sections V.3.5. and V.3.6.

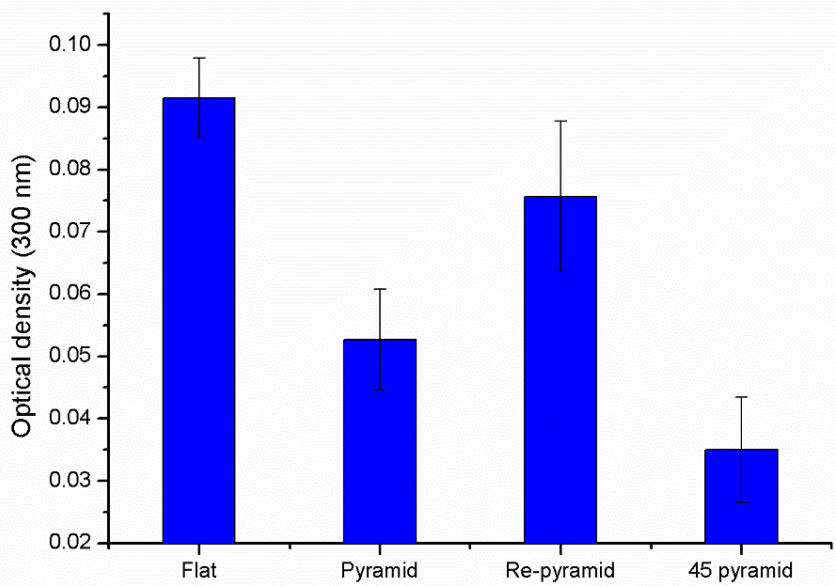

Figure V-5. Amounts of particle deposition at each membrane surface

V.3.3. Wall shear stress near the flat and patterned membrane surface

Wall shear stresses of flat and patterned membranes were visualized as variation of colors in figure V-6. The red and blue colors of the vertical bar indicate higher and lower wall shear stress, respectively. At the flat membrane surface, wall shear stress was identical on whole membrane surface with orange color. On the other hand, wall shear stress was decreased largely at reverse-pyramid pattern comparing with flat membrane owing to flow blockage which was induced by 'closed pattern shape'. As a result, only a small area of top edge at reverse-pyramid pattern shows higher wall shear stress than sunken pattern wall comparing with flat membrane. The results of three dimensional modeling of pyramid and 45° rotated pyramid pattern indicated similar wall shear stress at top and bottom surface and dissimilar wall shear stress distributions were shown in middle region of pyramid and 45° rotated pyramid. Any flow disturbance ('open space') and relatively high flow velocity effect on membrane surface. As a result, larger wall shear stresses were shown at top region at both patterns. However, because of slow flow velocity and semi-closed space, low wall shear stresses were indicated at bottom of in pyramid and 45° rotated pyramid pattern. In the middle region of pyramid pattern, wall shear stresses were different depending on surface orientation. The wall shear stress of vertically oriented surface from flow direction showed low wall shear stress because the flow toward vertical surface was disturbed by previous pattern. On the other hand, pyramid surface that was parallel to flow direction present higher wall shear stress

than vertical surface as the flow was not hindered by previous pyramid pattern. At 45° rotated pyramid pattern, all of pattern surfaces are positioned 45° with respect to flow direction and therefore previous pyramid pattern does not affect wall shear stress of following pattern. As a result, every patterned surfaces indicate similar wall shear stress due to regular angle with flow direction.

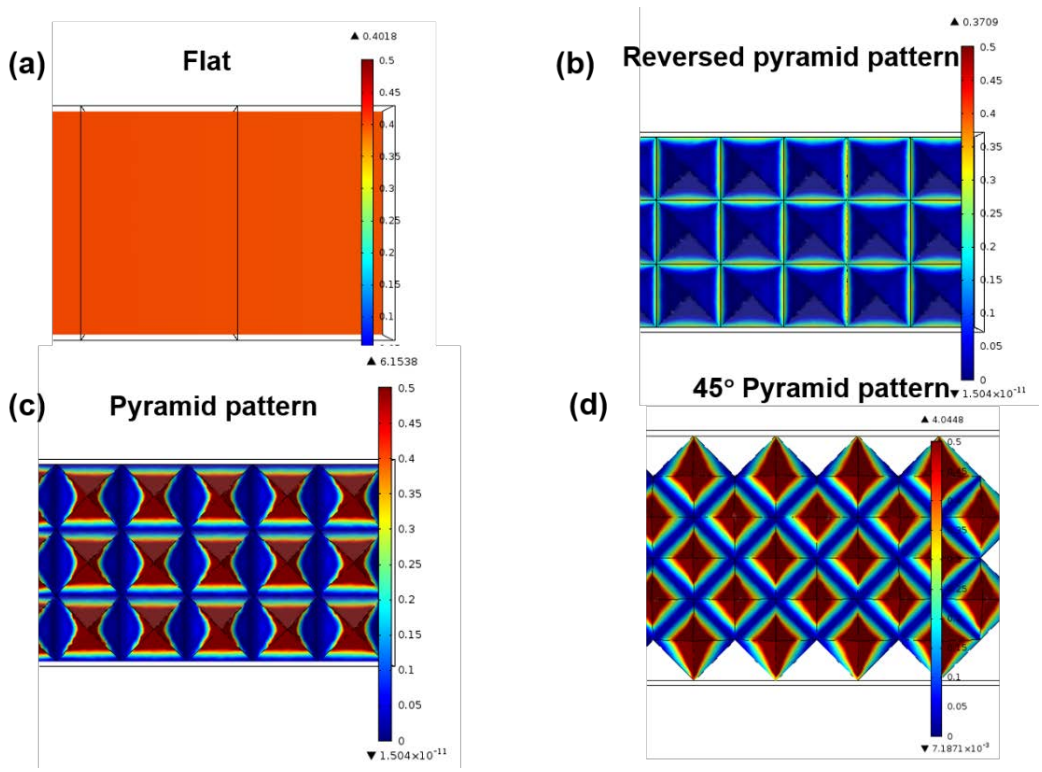

Figure V-6. Wall shear stresses at each membrane surface. The red and blue colors of the vertical bar indicate higher and lower wall shear stress, respectively.

V.3.4. Stream line near the flat and patterned membrane surface

Stream line at each membrane surface was analyzed by numerical method (figure V-7). While normal laminar flow was shown near the flat membrane, patterns shifted the laminar flow to complicated flow. Stream line near the reverse-pyramid pattern indicated slow flow velocity. Partial vortex was formed at the inner space of pattern and other flows faces toward membrane surface. On the other hand, fast stream line passed pattern through top region of pyramid and vortex like stream was formed between patterns that is semi-closed space. The end of the vortex like flows were directed toward membrane surface. Completely different stream was shown at 45° rotated pyramid pattern in spite of the same pattern shape. Streams take a detour near the pattern surface. Furthermore, faster stream velocity was presented at same height comparing with pyramid pattern and vortex was not formed owing to opened pattern space.

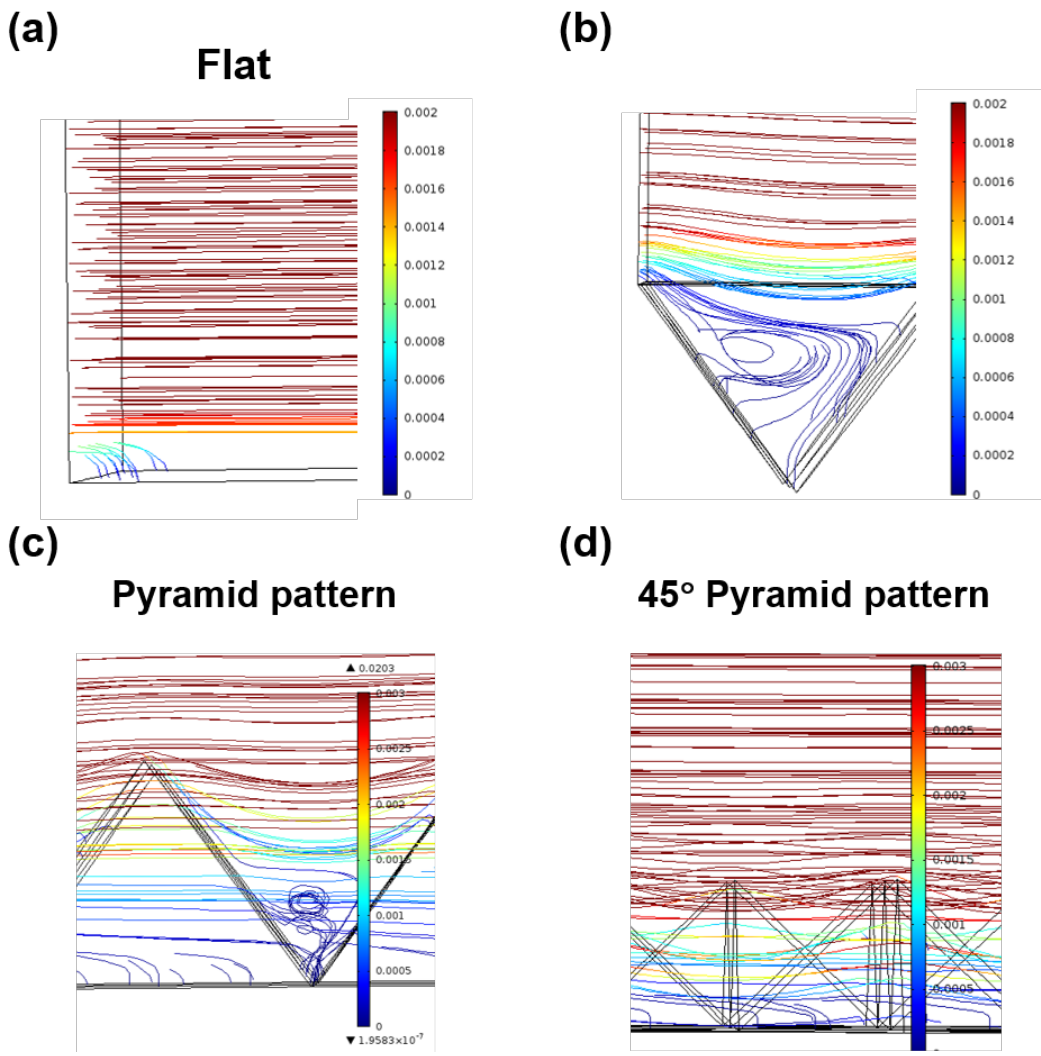

Figure V-7. Velocity profiles at each membrane surface

V.3.5. Relationship between particle deposition and wall shear stress

Figure V-8 indicates maximum wall shear stress of each membrane surface. The maximum wall shear stress of flat and reverse-pyramid pattern reveal similar value and the values were much lower than pyramid and 45° rotated pyramid pattern. The critical shear stress, which enables detachment of particles from membrane, would exist in flat or reverse pyramid and 45° rotated pyramid pattern. As a result, the amount of particle deposition was much larger on flat and reverse-pyramid than pyramid and 45° rotated pyramid pattern.

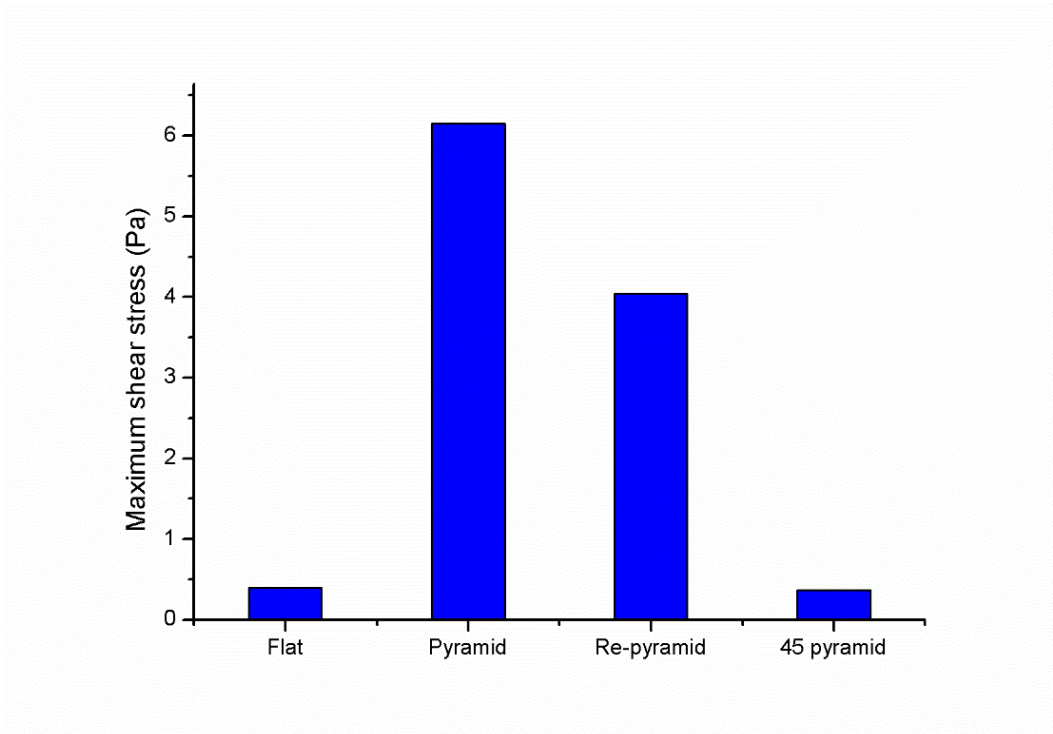

Figure V-8. Maximum wall shear stresses of each pattern shape.

V.3.6. Relationship between particle deposition and stream line

In spite of similar maximum wall shear stress on flat and reverse-pyramid pattern, the number of deposited particle was larger at flat membrane. As shown in figure V-6 (a), flow change was not occurred on flat membrane surface while, flow separation and incomplete vortex were appeared on reverse-pyramid pattern (figure V-6 (b)). The flow separation and vortex would prevent particle movement toward the bottom and deposit inside the reverse-pyramid pattern.

Comparing deposited amount of particle between pyramid and 45° rotated pyramid pattern, the deposited amount was much larger on pyramid pattern. Particle deposition at the bottom edge of pattern could occur on the both patterns. However, additional deposition area was only found at pyramid pattern. As shown in figure V-6 (c) incomplete vortex like stream was formed between each pyramid patterns and the vortex like stream faced toward bottom edge of the pattern. As a result, larger deposable area on pyramid pattern than 45° rotated pyramid pattern would induce more deposited amount of particle.

V.4. Conclusions

The effect of pattern shape and orientation on membrane fouling was identified by combining particle deposition experiment and three dimensional modeling. Micro patterns on the membrane surface alter wall shear stress distribution. Maximum wall shear stress was increased at pyramid and 45° rotated pattern while reverse-pyramid pattern showed similar value comparing with flat membrane. The increased maximum wall shear stress decreased particle deposition amount at pyramid and 45° rotated pattern. The micro patterned also altered flow behavior near membrane surface. Permeation drag force was larger at flat than reverse-patterned membrane and the difference affected more particle deposition at flat membrane. At pyramid pattern stream of larger region faced toward membrane surface and it induced more particle deposition than 45° rotated patterned membrane.

Chapter VI

Conclusions

VI. Conclusions

VI-1. Micro- and submicron isopore membranes were prepared using a soft lithography technique and a material with low surface energy. The following conclusions can be drawn:

- The membranes have uniformity of pore size. The size (and uniformity) of pores and their spatial distribution can be not only precisely controlled by the patterns on the mold or stamp used, but also easily varied by simply changing the process conditions.
- The soft-lithographically patterned membrane had non-tortuous pores running through the entire thickness of the membrane.
- Releasing agent in the UV-curable PUA oligomer solution induced lower surface energy than polycarbonate and it could lead to less biofouling.

VI-2. A patterned isopore membrane was prepared from UV-curable polymer by the soft lithographic method and factors affecting particle depositions were investigated with experiments as well as with 3D modeling. The following conclusions can be drawn:

- Uniform pore was formed in the center of each reverse-pyramid pattern and its size was dependent on the spinning rate of a PDMS replica mold.
- The number and position of particle depositions on the patterned surface

were largely dependent on the crossflow rate, pore water flux and size of particles in the feed suspension.

- Three-dimensional CFD modeling revealed that two stream lines (bulk and vortex) were generated on the surface of the reverse-pyramid patterned membrane and were in accordance with the trends of particle depositions during the microfiltration.

VI-3. The effect of pattern shape and orientation on membrane fouling was identified by particle deposition experiment and three dimensional modeling. The following conclusions can be drawn:

- Micro patterns on the membrane surface alter wall shear stress distribution and stream characteristics.
- Wall shear stress distribution was depend on pattern shape and orientation and maximum wall shear stress affect particle detachment.
- Flow separation and incomplete vortex formation on reverse-patterned membrane reduced the extent of particle deposition.
- At pyramid pattern stream of larger region faced toward membrane surface and it induced more particle deposition than 45° rotated patterned membrane.

국 문 초 록

분리막을 이용한 수처리 기술은 여러 장점으로 인해 널리 사용되고 있지만 분리막의 넓은 공극크기분포와 막오염은 여전히 해결해야 할 문제로 남아있다. 이 문제를 해결하기 위해 본 연구에서는 소프트 리소그래피공법과 광경화성 고분자를 이용하여 등방공경 분리막을 제작하였고 3 차원 모델링을 통해 패턴형 분리막에서의 유체의 유동과 그 유동이 입자의 부착에 미치는 영향을 평가하였다.

첫번째로, 소프트 리소그래피를 이용하여 등방공경 분리막을 제작하였다. 기존 분리막 대비 좁은 공극크기분포를 얻기 위하여 마이크로 크기의 패턴을 사용하여 공극의 크기를 조절하였다. 또한 표면에너지가 낮은 광 경화성 고분자를 사용하였고 그 결과 낮은 표면에너지로 인해 기존 분리막대비 소프트 리소그래피를 이용하여 제작된 등방공경 분리막의 내 오염성이 향상된 것 또한 확인하였다.

두 번째로는, 첫번째 연구를 통해 개발한 등방공경 분리막 제작기법을 응용하여 패턴형 등방공경 분리막을 제작하였고 입자부착실험을 통해 오염 메커니즘을 규명하였다. 입자부착실험은 십자형흐름 여과를 통해 수행되었으며 부착된 입자의 양은 입자의

크기뿐만 아니라 유체의 선속도와 공극을 통과하는 속도의 비의 영향을 받았다. 삼차원 모델링은 와류의 형성과 역피라미드 패턴형 분리막에서의 오염 메커니즘을 규명하기 위해 수행되었다. 특히 와류의 형성 유무가 입자부착의 경향에 큰 영향을 미치는 것을 확인하였다.

마지막으로, 각각 패턴의 모양과 방향이 다른 패턴형 분리막에서 삼차원모델링과 입자부착실험을 이용하여 패턴형상에 따른 내 오염성 효과를 규명하였다. 십자형 여과를 통해 부착된 입자의 양이 패턴의 모양 및 방향에 따라 변화하는 것을 확인하였다. 이러한 경향을 해석하기 위해 삼차원 모델링을 통해 분리막 표면의 응력 분포 및 패턴 근처에서의 흐름변화를 관찰하였다. 그 결과 패턴 근처에서의 수력학적 변화는 입자의 부착에 영향을 미친다는 것을 확인하였으며 특히 최대응력이 부착되는 입자의 양에 큰 영향을 미친 것을 확인할 수 있었다.

주요어 : 등방공경 분리막, 패턴형 분리막, 입자부착, 내 오염성, 삼차원 모델링,
소프트 리소그래피, 응력, 와류

Reference

Apel, P. (2001) Track etching technique in membrane technology. Radiation Measurements, 34, (1-6) 559-566.

Baker, J.S. and Dudley, L.Y. (1998) Biofouling in membrane systems - A review, Desalination, 118(1-3), 81-89.

Brittain, S., Paul, K., Zhao, X.M. and Whitesides, G. (1998a) Soft lithography and microfabrication. Physics World 11(5), 31-36.

Brittain, S., Kenis, P.J.A., Schueller, O.J.A., Jackman, R.J. and Whitesides, G.M. (1998b) The use of soft lithography for the fabrication of components for micro electromechanical systems (MEMS). Abstracts of Papers of the American Chemical Society 216, U312.

Calvo, J.I., Hernández, A., Prádanos, P., Martınez, L., and Bowen, W.R. (1995) Pore Size Distributions in Microporous Membranes II. Bulk Characterization of Track-Etched Filters by Air Porometry and Mercury Porosimetry. Journal of Colloid and Interface Science 176(2), 467-478.

Campbell, D.J., Beckman, K.J., Calderon, C.E., Doolan, P.W., Ottosen, R.M., Ellis, A.B., and Lisensky, G.C. (1999) Replication and compression of bulk and surface structures with polydimethylsiloxane elastomer, Journal of Chemical Education, 76, 537-541.

Chiang, Y. C., Chang, Y., Chuang, C. J. and Ruaan R. C. (2012) A facile zwitterionization in the interfacial modification of low bio-fouling nanofiltration membranes. Journal of Membrane Science 389, 76-82.

Choi, K.M. and Rogers, J.A. (2003) A photocurable poly(dimethylsiloxane) chemistry designed for soft lithographic molding and printing in the nanometer regime. Journal of American Chemical Society 125(14), 4060-4061.

Choi, S.J., Yoo, P.J., Baek, S.J., Kim, T.W. and Lee, H.H. (2004) An ultraviolet-curable mold for sub-100 nm lithography. Journal of the American Chemical Society 126(25), 7744-7745.

Chon, K., Cho, J. and Shon, H.K. (2013) Fouling characteristics of a membrane bioreactor and nanofiltration hybrid system for municipal wastewater reclamation. Biosource Technology 130, 239-247.

Culfaz, P.Z., Buetehorn, S., Utiu, L., Kueppers, M., Blue mich, B., Melin, T., Wessling, M. and Lammertink, R.G.H. (2011a) Fouing Behavior of Microstructured Hollow Fiber Membranes in Dead-End Filtrations: Critical Flux Determination and NMR Imaging of Particle Deposition. Langmuir 27(5), 1643-1652.

Culfaz, P.Z., Haddad, M., Wessling, M., and Lammertink, R.G.H. (2011b) Fouling behavior of microstuctured hollow fibers in cross-flow filtrations: Critical flux determination and direct visual observation of particle deposition. Journal of Membrane Science 372(1-2), 210-218.

Culfaz, P.Z., Rolevink, E., van Rijin, E. C., Lammertink, R.G.H. and Wessling, M.(2010) Microstructured hollow fibers for ultrafiltration. Journal of Membrane Science 347 (1-2), 32-41.

Culfaz, P.Z., Wessling, M. and Lammertink, R.G.H. (2011c) Hollow fiber ultrafiltration membranes with microstructured inner skin. Journal of Membrane Science 369 (1-2), 221-227.

Culfaz, P.Z., Wessling, M. and Lammertink, R.G.H. (2011d) Fouling behavior of microstructured hollow fiber membranes in submerged and aerated filtrations. Water Research 45(4), 1865-1871.

Drew, A. (2006) Membrane fouling in membrane bioreactors: Characterisation, contradictions, cause and cures. Journal of Membrane Science 363, 1–28.

Fowkes, F. M. (1962) DETERMINATION OF INTERFACIAL TENSIONS, CONTACT ANGLES, AND DISPERSION FORCES IN SURFACES BY

ASSUMING ADDITIVITY OF INTERMOLECULAR INTERACTIONS IN SURFACES. The Journal of Physical Chemistry 66(2), 382.

Gronda, A.M., Buechel, S., and Cussler, E.L. (2000) Mass transfer in corrugatedmembranes. Journal of Membrane Science 165, 177–187.

Tracey, E. M. and Davis, R. H. (1994) Protein Fouling of Track-Etched Polycarbonate Microfiltration Membranes Journal of Colloid and Interface Science 167(1), 104-116.

Ho, C. and Zydney, A. L. (1999) Effect of membrane morphology on the initial rate of protein fouling during microfiltration. Journal of Membrane Science 155(2), 261-275.

Ho, J.M., Beck, R.G., Westervelt, R.M. and Whitesides, G.M. (1998) The use of soft lithography to fabricate arrays of Schottky diodes. Advanced Materials 10(8), 574.

Hui, C.Y., Jagota, A., Lin, Y.Y. and Kramer, E.J. (2002) Constraints on microcontact printing imposed by stamp deformation. Langmuir 18(4), 1394-1407.

Hoek, E.M.V., Kim, A. S. and Elimelech, M. (2002) Influence of crossflow membrane filter geometry and shear rate on colloidal fouling in reverse osmosis and nanofiltration separations. Environmental Engineering Science 19(6) 357-372.

Hong, P.S. and Lee, H.H. (2003) Pattern uniformity control in room-temperature imprint lithography. Applied Physics Letters 83(12), 2441-2443.

Huang, Z., Geyer, N., Werner, P., de Boor, J. and Gosele, U. (2011) Metal-Assisted Chemical Etching of Silicon: A Review. Advanced Materials 2011, 23, 285-308.

Jeon, N.L., Hu, J.M., Whitesides, G.M., Erhardt, M.K. and Nuzzo, R.G. (1998) Fabrication of silicon MOSFETs using soft lithography. Advanced Materials 10(17), 1466-1469.

Judd, S. and Judd, C. (2006) The MBR book: Principles and Applications of Membrane Bioreactors in Water and Wastewater Treatment, Elsevier, Amsterdam, The Netherlands.

Karunakaran, M., Nunes, S. P., Qiu X., Yu, H., and Peinemann, K.-V. (2014) PS-b-PEO ultrafiltration membranes via self-assembly and water-induced phase separation. Journal of Membrane Science, 453, Pages 471–477

Kim, E., Xia, Y.N. and Whitesides, G.M. (1996) Micromolding in capillaries: Applications in materials science. Journal of the American Chemical Society 118(24), 5722-5731.

Kim, Y.S., Suh, K.Y. and Lee, H.H. (2001) Fabrication of three-dimensional microstructures by soft molding. Applied Physics Letters 79(14), 2285-2287.

Khang, D.Y. and Lee, H.H. (2000) Room-temperature imprint lithography by solvent vapor treatment. Applied Physics Letters 76(7), 870-872.

Khang, D.Y., Yoon, H. and Lee, H.H. (2001) Room-temperature imprint lithography. Advanced Materials 13(10), 749-752.

Khang, D.Y., Khang, H., Kim, T. and Lee, H.H. (2004) Low-pressure nanoimprint lithography. Nano Letters 4(4), 633-637.

Khang, D.Y. and Lee, H.H. (2004a) Sub-100 nm patterning with an amorphous fluoropolymer mold. Langmuir 20(6), 2445-2448.

Khang, D.Y. and Lee, H.H. (2004b) Pressure-assisted capillary force lithography. Advanced Materials 16(2), 176.

Kumar, A., Biebuyck, H.A. and Whitesides, G.M. (1994) Patterning Self-Assembled Monolayers – Applications in Materials Science. Langmuir 10(5), 1498-1511.

Lai, K.L., Leu, I.C. and Hon, M.H. (2009) Soft imprint lithography using swelling/deswelling characteristics of a polymer mold and a resist induced by a poor solvent. Journal of Micromechanics and Microengineering 19(3).

Le-Clech, P., Chen, V. and Fane, T. A.G. (2010) Fouling in membrane bioreactors used in wastewater treatment. Journal of Membrane Science 284 (1-2) 17-53.

Lee, J.N., Park, C. and Whitesides, G.M. (2003) Solvent compatibility of poly(dimethylsiloxane)-based microfluidic devices. Analytical Chemistry 75(23), 6544-6554.

Lee, W., Ji, R., Gosele, U. and Nielsch, K. (2006) Fast fabrication of long-range ordered porous alumina membranes by hard anodization. Nature Materials 5, 741-747.

Lee, Y.K., Won, Y.J. Won, Yoo, J.H., Ahn, K.H., and Lee, (2013) C.H. Flow analysis and fouling on the patterned membrane surface, Journal of Membrane Science, 427, 320-325.

Leoni, L., Attiah, D., and Desai, T. A. (2002) Nanoporous Platforms for Cellular Sensing and Delivery. Sensors 2, 111-120.

Li, F., Meindersma, W., de Haan, A.B. and Reith, T. (2002) Optimization of commercial net spacers in spiral wound membrane modules. Journal of Membrane Science 208, 289-302.

Liu Y. and Zhao Q. (2005) Influence of surface energy of modified surfaces on bacterial adhesion. Biophysical Chemistry 117(1), 39-45.

Martínez-Villa, F., Arribas, J.I. and Tejerina, F. (1988) Quantitative microscopic study of surface characteristics of track-etched membranes. Journal of Membrane Science 36, 19-30.

Maruf, S., Greenberg, A. R., Pellegrino, J., and Ding, Y. (2014) Critical flux of surface-patterned ultrafiltration membranes during cross-flow filtration of colloidal particles. Journal of Membrane Science 471, 65-71.

Masuda, H., Yasui, K., and Nishio, K. (2000) Fabrication of Ordered Arrays of Multiple Nanodots Using Anodic Porous Alumina as an Evaporation Mask. Advanced Materials 12(14), 1031-1033.

Mohanty, K., Purkait, M. K. (2011) Membrane Technologies and Applications, CRC Press, New York, USA.

Odom, T.W., Love, J.C., Wolfe, D.B., Paul, K.E. and Whitesides, G.M. (2002) Improved pattern transfer in soft lithography using composite stamps. Langmuir 18(13), 5314-5320.

Ou, Y., Lv, C.J., Yu, W., Mao, Z.W., Wan, L.S. and Xu, Z.K. (2014) Fabrication of Perforated Isoporous Membranes via a Transfer-Free Strategy: Enabling High-Resolution Separation of Cells. ACS Applied Materials & Interfaces 6, 22400-22407.

Ohya, H., Kim, J.J., Chinen, A., Aihara, M., Wemenova, S.I., Nehishi, Y., Mori, O. and Yasuda, M. (1998) Effect of pore size on separation mechanisms of microfiltration of oily water, using porous glass tubular membrane, Journal of Membrane Science, 145, 1-14.

Price, P.B., Walker, R.M., (1962) Electron Microscope Observation of Etched Tracks from Spallation Recoils in Mica Physical Review Letters 8, 217-19.

Radu, A.I., van Steen, M.S., Vrouwenvelder, J.S., van Loosdrech, M.C. and Picioreanu, C. (2014) Spacer geometry and particle deposition in spiral wound membrane feed channels. Water Research, 64 160-176.

Rahimi, M., Madaeni, S.S. and Abbsi, K. (2005) CFD modeling of permeate flux in cross-flow

microfiltration membrane. Journal of Membrane Science 255, 23-31.

Rogers, J.A. and Lee, H.H. (2009) Unconventional nanopatterning techniques and applications, Wiley, Hoboken, N.J.

Ruchhoeft, P., Colburn, M., Choi, B., Nounu, H., Johnson, S., Bailey, T., Damle, S., Stewart, M., Ekerdt, J., Sreenivasan, S.V., Wolfe, J.C. and Willson, C.G. (1999) Patterning curved surfaces: Template generation by ion beam proximity lithography and relief transfer by step and flash imprint lithography. Journal of Vacuum Science & Technology B 17(6), 2965-2969.

Schwinge, J., Wiley, D.E. and Fletcherb, D.F. (2002) A CFD study of unsteady flow in narrow spacer-filled channels for spiral-wound membrane modules. Desalination 146 195-201.

Sharp, K.G., Blackman, G.S., Glassmaker, N.J., Jagota, A. and Hui, C.Y. (2004) Effect of stamp deformation on the quality of microcontact printing: Theory and experiment. Langmuir 20(15), 6430-6438.

Strathmann, H. (2011) Introduction to Membrane Science and Technology, Wiley-VCH, Weinheim, Germany.

Suh, K.Y., Kim, Y.S. and Lee, H.H. (2001) Capillary force lithography. Advanced Materials 13(18), 1386-1389.

Tong, H. D., Jansen, H. V., Gadgil, V. J., Bostan, C. G., Berenschot, E., van Rijn, C. J. M. and Elwenspoek, M. (2004) Silicon Nitride Nanosieve Membrane. Nano Letters 4, 283-287.

Urase, T., Yamamoto, K. and Ohgaki, S. (1996) Effect of pore structure of membranes and module configuration on virus retention, Journal of Membrane Science, 115, 21-29.

Vakuliuk, P., Burban, A., Konovalova, V., Bryk, M., Vortman, M., Klymenko, N. and Shevchenko V. (2009) Modified track membranes with antibacterial properties. Desalination 235, 160-169.

Vrouwenvelder, J.S., Piciorenu, C., Kruithof, J.C. and van Loosdrecht, M.C.M. (2010) Biofouling in spiral wound membrane systems: Three-dimensional CFD model based evaluation of experimental data. Journal of Membrane Science 346, 71-85.

Vogelaar, L., Barsema, J. N., van Rijn, C. J. M., Nijdam, W. and Wessling, M. (2003) Phase Separation Micromolding—PSμM. Advanced Materials 15, 1385-1389.

Wang, Y., Brannock, M., Cox, S. and Leslie, G. (2010) CFD simulations of membrane filtration zone in a submerged hollow fibre membrane bioreactor using a porous media approach. Journal of Membrane Science, 363, 57-66.

Wachner, D., Marczewski, D. and Goedel, W.A. (2013) Utilising spontaneous self-organization of particles to prepare asymmetric, hierarchical membranes comprising microsieve-like parts. Advanced Materials, 25(2), 278-283.

Wan, L.S., Li, J.W., Ke, B.B. and Xu, Z.K. (2012) Ordered microporous membranes templated by breath figures for size-selective separation, Journal of the American Chemical Society, 134, 95-98.

Warkiani, M.E., Chen, L., Lou, C.P., Liu, H.B., Zhang, R. and Gong, H.Q. (2011) Capturing and recovering of Cryptosporidium parvum oocysts with polymeric micro-fabricated filter, Journal of Membrane Science, 369, 560-568.

Warkiani, M.E., Bhagat A.A.S., Khoo, B.L., Han, J., Lim, C.T., Gong, H.Q. and Fane, A.G. (2013) Isoporous micro/nanoengineered membranes. ACS Nano, 7(3), 1882-1904.

Wei, P., Zhang, K., Gao, W., Kong, L. and Field, R. (2013) CFD modeling of hydrodynamic characteristics of slug bubble flow in a flat sheet membrane bioreactor. Journal of Membrane Science, 445, 15-24.

Won, Y.J., Lee, J., Choi, D.C., Chae, H.R., Kim, I., Lee, C.H., and Kim, I.C. (2012) Preparation and application of patterned membranes for wastewater treatment. Environmental Science & Technology 46(20), 11021-11027.

Won, Y.J., Choi, D.C., Jang, J.H. Jang, Lee, J.W. Lee, Chae, H.R., Kim, I., Ahn, K.H., Lee, C.H. and Kim, I.C. (2014) Factors affecting pattern fidelity and performance of a patterned membrane. Journal of Membrane Science, 462,1-8.

Worrel, L. S., Morehouse, J. A., Shimko, L. A., Lloyd, D. R., Lawler, D. F. and Freeman, B. D. (2007) Enhancement of track-etched membrane performance via stretching, Separation and Purification Technology 53, 71-80.

Xia, Y.N. and Whitesides, G.M. (1998) Soft lithography. Angewandte Chemie-International Edition 37(5), 551-575.

Yan, F. and Goedel, W. A. (2004) A Simple and Effective Method for the Preparation of Porous Membranes with Three-Dimensionally Arranged Pores. Advanced Materials 2004, 16(11), 911-915.

Yan, F., Ding, A. M., Girones, Lammertink, R. G. H., Wessling, M., Borger, L., Vilsmeier, K., and Goedel, W. (2012) Hierarchically Structured Assembly of Polymer Microsieves, made by a Combination of Phase Separation Micromolding and Float-Casting Advanced Materials 24(12), 1551-1557.

Ye, X.D., Ding, Y.C., Duan, Y.G., Liu, H.Z. and Lu, B.H. (2010) Room-temperature capillary-imprint lithography for making micro-/nanostructures in large areas. Journal of Vacuum Science & Technology B 28(1), 138-142.

Yoo, P.J., Choi, S.J., Kim, J.H., Suh, D., Baek, S.J., Kim, T.W. and Lee, H.H. (2004) Unconventional patterning with a modulus-tunable mold: From imprinting to microcontact printing. Chemistry of Materials 16(24), 5000-5005.

Yuanfa, L., Gaohong, H. Luhui, D., Hong, D., Jia, J. and Baojun, L. (2012) Experimental and CFD studies on the performance of microfiltration enhanced by a turbulence promoter. Separation Science and Engineering 20(4), 617-624.